POLITECNICO DI MILANO
School of Industrial and Information Engineering
Master of Science in Aeronautical Engineering
Dipartimento di Scienze e Tecnologie Aerospaziali

A Comprehensive Aeroservoelastic Approach to Detect and Prevent Pilot Assisted Oscillations in Tiltrotors

Supervisor:
Prof. Pierangelo Masarati

Co-supervisors:
Prof. Giuseppe Quaranta
Ing. Vincenzo Muscarello

Master Thesis by:
Francesca Colombo, ID 852417

Academic Year 2016-2017

Abstract

In tiltrotors, as well as in helicopters and airplane, the structural vibrations of the aircraft can interact with the involuntary pilot's biodynamics causing inadvertent man-machine coupling phenomena. These events are known in literature as PAOs, acronym of *Pilot Assisted Oscillations* and can cause oscillatory or divergent motions, difficulty in performing the desired tasks, and, ultimately, loss of control.
PAOs occur in a frequency range between 2 and 8 Hz and they require an accurate aeroservoelastic modelling of the vehicle. This work presents an effective approach to develop multidisciplinary aeroservoelastic models that can tackle this peculiar type of problems. A detailed tiltrotor model, representative of the Bell XV-15, has been built using the simulation tool MASST, developed at Politecnico di Milano for the aeroservoelastic and aeromechanical analysis of aircraft and rotorcraft. This model includes a finite element airframe structural model, airframe unsteady aerodynamics, aeroelastic rotors, drive-train, servo-actuators and controllers.
Biomechanical models of the pilot are included in feedback loop to define the Pilot-Vehicle System (PVS). The pilot, acting on the power lever and on the control stick, is described using a transfer function that characterises the biodynamic feedthrough (BDFT), i.e. involuntary control inceptor motion caused by external accelerations transmitted to the pilot's body.
With the introduction of the pilot, the system is studied using robust stability analysis techniques. In particular, the stability margins of the system are quantified using Nyquist's criterion.
PAO analyses are conducted separately along the longitudinal, lateral and vertical axes. Once a PAO mechanism is identified, a model reduction is performed to detect the main dynamics and the most influential parameters that trigger the instability. Finally, possible means of prevention are investigated and their pros and cons are discussed.

Sommario

Nei convertiplani, così come negli elicotteri e negli aeroplani, le vibrazioni strutturali del velivolo possono attivare la riposta biomeccanica involontaria del pilota, generando percorsi di carico potenzialmente critici in grado di deteriorare le prestazioni della macchina. Interazioni avverse tra pilota e velivolo possono provocare oscillazioni, determinare difficoltà nel completare una missione o, in ultima istanza, causare la perdita di controllo del sistema. Questi fenomeni di accoppiamento uomo-macchina sono noti in letteratura con la sigla PAO, acronimo di *Pilot Assisted Oscillation*.
I PAO si verificano in una banda passante compresa tra 2 e 8 Hz, e richiedono accurate modellazioni aeroelastiche di un velivolo. Al fine di cogliere questo tipo di fenomeni, è stato sviluppato un dettagliato modello del convertiplano Bell XV-15, comprensivo di una struttura elastica modellata a elementi finiti accoppiata ad una pannellatura aerodinamica in grado di rappresentare i carichi instazionari, rotori aeroelastici, drive-train, servo-attuatori e controllori. Il modello è elaborato in MASST, un software sviluppato in MATLAB® dal Politecnico di Milano per analisi aeroservoelastiche e aeromeccaniche di aeroplani ed elicotteri ed attualmente utilizzato da industrie leader nella produzione di elicotteri.
Le analisi di PAO sono effettuate introducendo dei modelli biomeccanici del pilota in retroazione al modello aeroservoelastico del velivolo. I modelli di pilota sono rappresentati da funzioni di trasferimento, disponibili in letteratura, che traducono l'azione del pilota sui comandi di stick longitudinale/laterale e sulla leva del collettivo/potenza.
La stabilità del sistema comprensivo di velivolo e pilota è analizzata mediante tecniche di stabilità robusta. In particolare, i margini di stabilità del sistema a ciclo chiuso sono quantificati utilizzando il criterio di Nyquist.
Le analisi di PAO sono realizzate separatamente lungo gli assi longitudinale, laterale e verticale; in ciascuno dei tre casi si analizzano i meccanismi responsabili dell'innesco di potenziali instabilità, individuando le dinamiche critiche. Infine, a seguito dell'identificazione di eventuali PAO, sono discussi possibili metodi di prevenzione del fenomeno.

Ringraziamenti

Ringrazio Pierangelo Masarati, Giuseppe Quaranta e Vincenzo Muscarello per avermi seguito e stimolato allo studio e alla ricerca quanto più approfondita della materia in analisi. Durante questo anno di lavoro con voi ho potuto mettere alla prova ed ampliare le conoscenze maturate in questi anni di studio. Vi ringrazio inoltre per avermi dato fiducia, offrendomi la possibilità di pubblicare il mio primo articolo scientifico per una rinomata società tecnica internazionale.

Vorrei dedicare questo lavoro di tesi alla mia famiglia. I miei genitori, Cristina e Lorenzo, sono un esempio di unione e forza e mi sostengono da sempre in modo incondizionato. Mia sorella Federica è una delle persone più in gamba che conosca e mi spinge costantemente a dare il meglio in tutto.

Se sono arrivata a questo punto è certamente merito anche di Alberto, che con immensa dolcezza e comprensione mi ha accompagnato in questo lungo ed impegnativo percorso.

Infine vorrei ringraziare la mia storica amica Camilla, per tutta la carica positiva che da sempre riesce a trasmettermi.

Contents

List of Figures

List of Tables

Chapter 1

Introduction

1.1 Tiltrotor History

The first realisation of a tiltrotor dates back to the early 1920s with a flying machine attributed to Henry Berliner. This vehicle, depicted in Figure 1.1(a), was similar to a fixed-wing biplane, except it had a tilting propeller mounted near the tip of each wing (Ref.[1]). The later British Baynes Heliplane, of Figure 1.1(b), proposed a configuration that resembles the design of modern tiltrotor aircraft (Ref.[2]). In 1942 the German Focke-Achgelis FA-269 convertiplane used pusher propellers that tilted below the wing for take-off (Ref.[3]). This project was destroyed during a bombing in WWII. A few years later, in 1947, Transcendental Aircraft Corporation of New Castle, Delaware, started working on the 1-G tiltrotor aircraft of Figure 1.2(a). The founding's principals were Mario A. Guerrieri and Robert L. Lichten.

During the late 1940s and early 1950s many researches were dedicated to the design of a vertical take-off and landing (VTOL) vehicle that, combining the

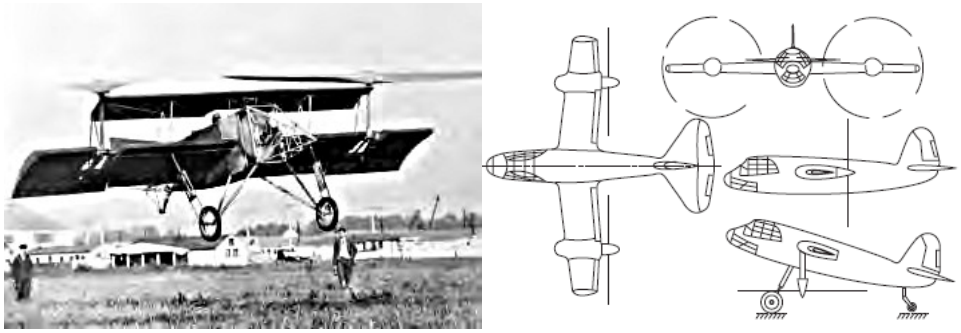

(a) Berliner Heliplane, 1920s Ref.[1] (b) Baynes Heliplane, 1930s Ref.[1]

Figure 1.1: Tiltrotor Concept

performances of an helicopter and of an airplane, could sustain significant hover duration, be manoeuvrable at low speeds and possess large efficiency in range.
During the August of 1950, U.S. Army and U.S. Air Force jointly initiated a *Convertiplane Program*. Different kinds of vehicles were suitable to satisfy the performances required by the *Program*, among which the Sikorsky XV-2 stoppable rotor aircraft, the McDonnel XV-1 compound helicopter and the Bell XV-3 tiltrotor aircraft. The tiltrotor and the compound helicopter represented the most promising options, although, in the second case, many severe aspects strongly limited the potential performances. The compound helicopter was provided with a fixed-wing that produced lift during forward flight and it allowed to unload the rotor that, however, encountered the variations in rotor blade drag due to the advancing and retreating airloads during each rotation. It became apparent that the compound helicopter suffered from the same speed limitations typical of a helicopters (Ref.[1]). These aspects made the Bell XV-3 tiltrotor to be engaged in the U.S. Army and U.S. Air Force *Convertiplane Program*.

The Bell XV-3 (Figure 1.2(b)) provided an opportunity to demonstrate the effectiveness of the tiltrotor concept. Its first flight occurred in 1955 but, during subsequent flights between 1955 and 1956, a rotor dynamic instability appeared, causing airframe damages. The rotor design was subsequently strongly modified and the tiltrotor completed 110 transitions from helicopter to airplane mode between December 1958 and July 1962 (Ref.[1]). In 1959 the XV-3 was subjected to a Government flight evaluation, whose report concluded that "the fixed-wing prop-rotor (i.e. the tiltrotor) principle is feasible and should be given serious consideration in future Vertical or Short Takeoff and Landing aircraft design competition. [...] The XV-3 demonstrates that the fixed-wing prop-rotor concept is operationally practical with safety and complexity comparable to helicopters " Ref.[4].

(a) Transcendental 1-G, 1947 Ref.[1] (b) Bell XV-3, 1950 Ref.[2]

Figure 1.2: First Tiltrotors' Realisations

Figure 1.3: Bell XV-15, 1972

The data and experience derived from the XV-3 program were key elements used to successfully develop the Bell XV-15, Figure 1.3. What was to become the XV-15 program was launched in 1971 at NASA Ames Research Center. Contracts were issued to Bell Helicopter and Boeing-Vertol on October 1972. After a review of the proposals of both companies, NASA selected the Bell 301, later renamed XV-15.

The first XV-15 flight traces back to May 3, 1977 and it consisted in accelerating the vehicle in helicopter mode by the application of power and the forward movement of the center control stick. The pilot was Ron Erhart and copilot Dorman Cannon. This first flight demonstrated satisfactory handling qualities and safe structural loads. After twenty years of research the XV-15 proved the tiltrotor aircraft's versatility and potential in many VTOL aircraft applications and inspired later researches both in civil and military applications (Refs.[1, 5]).

The V-22 tiltrotor aircraft, of Figure 1.4, was developed for the U.S. Navy by the team of Bell Helicopter Textron, Inc. and Boeing Helicopter Company

Figure 1.4: Bell-Boeing V-22 Osprey, 1989

and it was ideally suited for a wide range of military operations, documented in Ref.[6]. The first flight of the V-22 was March 19, 1989. This tiltrotor incorporated a digital fly-by-wire control system, separated into primary flight control system (PFCS) and automatic flight control system (AFCS). The cockpit controls included conventional cyclic stick and pedals; differently from previous XV-15, the power lever (PL) was replaced by a thrust command lever (TCL), which resembled an airplane throttle lever.

In November 1996, Bell and Boeing announced their collaboration for the design of the Bell Boeing 609 (BB609). The BB609 was the first tiltrotor designed for the civil market and its architecture was strongly inspired by the features that were applied to the V-22, such as fly-by-wire flight controls and avionics, advanced composites in the rotors and structure and Health and Usage Monitoring (HUM) systems.

In March 1998 Boeing abandoned the BB609 project to focus on military helicopters only and in September 1998 Bell announced a collaboration with the Agusta Helicopter Company (now Leonardo Helicopters). The BB609 was subsequently renamed BA609 (Bell-Agusta609, Fig.1.5). In 2011 AgustaWestland assumed full control of the program, renaming the aircraft AW609.

In 2013 Bell Helicopter Textron and Lockheed Martin presented the Bell V-280 Valor (Fig.1.6) for the *Future Vertical Lift (FVL) Program*. Its first flight was performed on December 18, 2017 in Amarillo, Texas.

Figure 1.5: Bell Agusta BA609, 1998

Figure 1.6: Bell V-280 Valor, 2013

1.2 Rotorcraft-Pilot Coupling Phenomena

This thesis focuses on the study of airplane/rotorcraft-pilot coupling (A/RPC) phenomena. Usually known under the name of Pilot Induced/ Assisted Oscillations, A/RPCs generally are oscillations or divergent responses of the vehicle originating from adverse pilot-vehicle couplings (PVCs)*. These undesirable couplings may result in potential instabilities that can degrade the handling qualities and lead to the exceedence of the structural strength envelope. Since early days of manned flight, A/RPCs have represented a critical issue for flight safety and the architecture of nowadays aircrafts/rotorcrafts, including flight control systems, increases the sensitivity to these kind of phenomena (Ref.[7]).

RPCs can be separated into Pilot Induced Oscillations (PIOs) and Pilot Assisted/Augmented Oscillations (PAOs). PIOs generally occur when the pilot excites divergent vehicle oscillations by applying control inputs that are in the wrong direction or have phase lag with aircraft motion (Refs.[7, 14]). PIO events involve the voluntary response of the pilot and verify in a frequency range below 1 Hz. In this bandwidth the aircraft's dynamics can be analysed by means of rigid body vehicle models.
On the other hand PAOs correspond to a different kind of interaction, since they involve the pilot's involuntary biodynamics. The pilot can respond at the structural frequencies creating an unstable feedback path caused by inadvertent or unintentional control inputs, resulting from inertial reaction of the pilot/control device to the accelerations of the cockpit. A PAO can be defined as the result of involuntary control input by the pilot that destabilise the aircraft due to inadvertent man-machine coupling (Ref.[7]). These phenomena occur at frequencies ranging from 2 to 8 Hz (Ref.[8]); for higher frequencies the pilot is not expected to react, and the human body is assumed to filter the vibrations of the cockpit. PAO studies require detailed aeroelastic vehicle modelling.

PIO and PAO phenomena have been extensively analysed in fixed wing aircraft and similar phenomena have been encountered in rotorcraft, although, in this case, the number of reported events and studies is rather more limited (Ref.[9]). Many reasons, shortly recalled below, can explain why RPCs are more likely to verify in rotary wing rather than fixed wing aircraft (Ref.[7]).

- rotorcraft are often required to execute demanding manoeuvres such as precision landings and hovering. The combination of extreme task

*http://aristotel-project.eu/

demands, which require very high pilot-gain, is one major reasons for RPC problems.

- the high level of vibrations, produced by the rotating-blade or by the aerodynamic interferences between the rotor and the fuselage, excites the pilot, interfering with command inputs or producing involuntary inputs, i.e. biodynamic coupling.
- in rotorcraft there exists a high inherent phase lag between inceptor input and vehicle body response due to the time required for actuator and rotor responses.

This thesis focuses on the study of PAO phenomena in tiltrotors. In the following it is shortly resumed a list of PAO events that has verified in rotary wing aircraft.

The *vertical bounce* is a PAO instability typical of helicopters and it involves vertical accelerations caused by a pulsating thrust due to the pilot acting on the collective control lever. Reference [7] lists many RPC studies about aeromechanical instabilities and some of the reported accidents are classified as vertical bounce occurrences. In recent years several events of this nature have occurred. In July 6, 2016 a vertical bounce phenomenon caused in-flight breakup of the Bell 525 during a one-engine inoperative (OEI) test. The two Test Pilots received fatal injuries, and the helicopter was destroyed (Ref.[10]). In October 2014, the same phenomenon was experienced by a Danish AW101 helicopter during landing in degraded visual environment[†]. Although the crew was not seriously injured the helicopter was destroyed. The accident report confirms a vertical bounce occurrence at 3.65 Hz. As a matter of fact, this topic represents a severe issue that is strongly involved in the design of modern helicopters.

A PAO occurrence caused by lateral accelerations is reported in Ref.[7] for the Boeing Vertol CH-46D/E Sea Knight. It is documented a 3.2 Hz oscillation due to the interaction between the rotor lead lag mode and the pilot, acting on the cyclic stick. A similar phenomenon has been also encountered on the SH-60 due to a flexible mode ground resonance (1981). Roll/lateral adverse aeroservoelastic rotorcraft-pilot couplings in helicopters were also investigated in Reference [34], by means of linear vehicle aeroservoelastic models and experimentally identified involuntary lateral pilot dynamics.

PAO events have been documented in tiltrotor aircraft as well. The Bell-Boeing V-22 Osprey is known to have suffered from three different kind of PAOs involving a 1.4 Hz lateral oscillation on the ground, a 3.4 Hz lateral

[†]https://aviation-safety.net/wikibase/wiki.php?id=201671

oscillation in airplane mode (APMODE) and a 4.2 Hz longitudinal oscillation in APMODE (Ref.[11]).
Even though this thesis focuses on PAO events only, it is recalled, for completeness, a recent PIO phenomenon occurred for the AW609 tiltrotor aircraft (Ref.[40]). In this case the coupling between the tiltrotor's lateral dynamics and the pilot flying control inputs through the control laws resulted in a very low frequency (0.1Hz) lateral-directional diverging oscillation. According to Ref.[40], the possible causes of the fatal accident correspond to three main factors: the development of latero-directional oscillations, the inability of the fly-by-wire flight control system (FCS) control laws to maintain controlled flight and the failure of the engineering flight simulator (SIMRX) to foresee the event. The actual reasons for the accident are still under investigation, however this occurrence has been proved to involve a RPC lateral dynamics.

In this thesis Pilot-in-the-loop stability analysis is performed by introducing pilot/control device elements in feedback loop with the tiltrotor aeromechanics. A general pilot-vehicle-system (PVS) scheme is represented in the block diagram of Figure 1.7. Pilot biomechanics is described using a transfer function that characterises the biodynamic feedthrough (BDFT), i.e. involuntary control inceptor motion caused by external accelerations transmitted to the pilot's body (Ref.[12]). The feedback, provided by the pilot's BDFT, may affect the stability margins of the system and may lead to the occurrence of unstable mechanisms. The closed loop system is also characterised by a Primary Flight Control System (PFCS), including the gear ratios between the control inceptor deflections and the corresponding control surfaces rotation, and a RPM governor. The XV-15 PFCS architecture is schematised in **Appendix A**. The possibility to introduce into the model an Automatic Flight Control System (AFCS), used to improve the tiltrotor's stability and handling qualities, will be investigated in a future work. Currently, its presence is accounted for by considering a gain

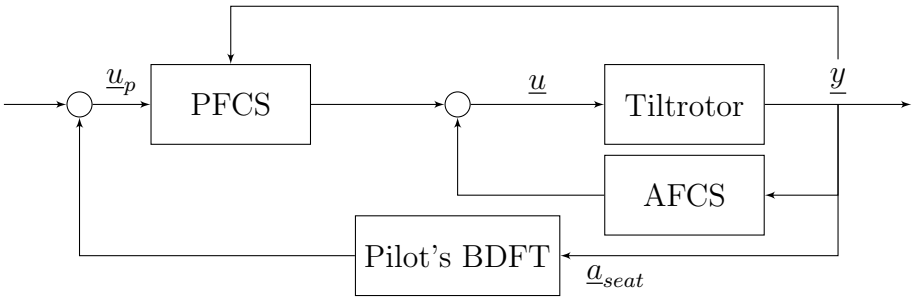

Figure 1.7: General PVS Scheme

and a time delay between the control inceptor motion produced by the pilot biomechanical model and the signals that are input to the actuators.

In conclusion, the interaction between the pilot and the vehicle is critical because it can potentially impact over the characteristics of performance, stability and safety of the PVS. Modern tiltrotors' design is aware of the possibility of this phenomenon to occur and pilot-in-the-loop stability analysis are considered since early design stages.

1.3 Outline

1.3.1 Thesis Objective

In tiltrotors, as well as in helicopters, the unintentional pilot's body response can be triggered by the structural vibrations of the vehicle, possibly creating an unstable feedback path. These phenomena go under the name of Pilot-Assisted-Oscillations (PAOs). This work presents an effective approach to develop multidisciplinary aeroservoelastic models that can tackle this peculiar type of problems.

A detailed tiltrotor model, representative of the Bell XV-15, is built using the simulation tool MASST, developed at Politecnico di Milano for the aeroservoelastic and aeromechanical analysis of aircraft and rotorcraft (Refs.[13, 17]). The realisation of a XV-15 aeroelastic model is enabled by a large database of the tiltrotor's general data available in open literature. Moreover, the choice of the XV-15 can be further justified by the fact that its layout resembles, in geometry and weight, the modern AW609 tiltrotor, whose specifics are not accessible. As a consequence, the study of the XV-15 dynamics can potentially emphasise issues associated with the design of modern tiltrotors.

The aim of this work is to perform Pilot-in-the-loop aeroservoelastic analyses and investigate possible PAO instability mechanisms along the longitudinal, lateral and vertical axes. Along each axis the pilot is modelled by means of a BDFT transfer function.
In this thesis, only category I Rotocraft Pilot Couplings are analysed (Ref.[8]), i.e. phenomena that do not imply a significant effect of nonlinearities (e.g. actuator saturations, freeplays, etc...). As a result, both the XV-15 and the pilot's models are linear. The tiltrotor's linear model is obtained from MASST while the pilot's linear transfer functions are derived from available open literature (Refs.[11], [12], etc.). It can not be excluded that for large amplitude oscillations the nonlinearities may have an impact, although this is outside the scope of the research presented here.
PAO phenomena are examined on the overall conversion corridor using Nyquist's criterion to analyse the stability and the robustness of the Pilot-vehicle-system (PVS). Once a PAO mechanism is identified, a model reduction is performed to detect the main dynamics and the most influential parameters that trigger the instability. Possible means of prevention are finally discussed.

1.3.2 Thesis Innovative Contribution

A broad literature exists about PAO events, mainly focused on fixed-wing aircraft. This thesis addresses these kind of RPCs in rotary wing aircraft and focuses on a deep understanding of PAOs in tiltrotors.

The lateral airplane mode instability mechanism described for the V-22 tiltrotor aircraft in Ref.[11] is studied in detail. The proverse yaw phenomenon, that triggers the lateral oscillations, is estimated by the unsteady aerodynamics implemented in NASTRAN, using the Doublet Lattice Method, which is a standard for aeroelastic analyses in aerospace industry. The adopted numerical approach innovatively substitutes the experimental methodology used in Ref.[11] to determine the magnitude of the aileron/fin interactional aerodynamic effects.
A critical parameter for the development of latero-directional oscillations is detected in the geometry of the vertical fins. This aspect is extensively investigated in order to identify new means of preventions associated with the preliminary design of the tail.

In helicopters a pulsating thrust, induced by an oscillation of the collective control lever, triggers the *vertical bounce* phenomenon (Refs.[12, 14, 9]). The analyses conducted in this thesis examine for the first time the vertical bounce in tiltrotors. Possible vertical instability mechanisms are explored on the overall conversion corridor. It is demonstrated that, in HEMODE configuration, the vertical unstable oscillations can result from a resonance between the airframe first symmetric wing bending (SWB) and the pilot's unintentional control input on the power lever (PL), due to a pulsating thrust generated by the rotors. It is also discovered that the SWB can be destabilised in APMODE, due to a pulsating torque produced by the rotors after an involuntary oscillation of the PL as a consequence of vertical accelerations. Finally it is stated that, for intermediate nacelle conversion angles, the destabilising phenomena encountered in HEMODE and APMODE are mixed.

1.3.3 Thesis Structure

In the following it is exposed the structure of the present work.

Chapter 2 This Chapter describes the dynamic set-up of a bioaeroservoelastic model representative of the Bell XV-15 Tiltrotor Research Aircraft. The many substructures that are part of the model (structural airframe, substructured nacelles, unsteady aerodynamics, aeroelastic rotors, servo-actuators ...) are outlined and the basics of their mathematical models are recalled.

Chapter 3 This Chapter reports a detailed description of the structural elastic airframe, which is described by means of a finite element (FE) stick model consisting of a ten-elements elastic wing with rigid fuselage and wing tip mounted nacelles. Furthermore, in order to represent the local compliance between the wing and the nacelle, it is introduced a nacelle-actuator scheme. The results obtained in this section are validated with general data available in open literature.

Chapter 4 A PVS analysis examines the relationship between the involuntary pilot's lateral cyclic stick motion and the subsequent vehicle motion in the lateral direction. The analyses are performed considering high speed airplane mode flight. A critical parameter for the occurrence of a lateral PAO is detected in the geometry of the vertical fins. Pilot-in-the-Loop analyses are subsequently performed considering two off-design tail configurations and the results are critically evaluated.

Chapter 5 The longitudinal PAO analysis investigates the trigger of possible instability mechanisms due to longitudinal oscillations of the cyclic stick induced by the involuntary pilot. Pilot-in-the-loop analyses are performed considering two configurations, corresponding to the airplane mode (APMODE) and helicopter mode (HEMODE). In both cases a set of representative airspeeds is considered. The results are discussed.

Chapter 6 The trigger of possible instability mechanisms on the vertical axis is investigated and a detailed Pilot-in-the-loop analysis is conducted over the entire conversion corridor. Possible means of prevention are represented by the design of notch filters at the flight control system level.

Chapter 7 This section presents the conclusions of this work, together with hints on possible future developments.

Chapter 2

XV-15 Dynamic Set-up

A detailed tiltrotor model, representative of the Bell XV-15, has been built using the simulation tool MASST (Modern Aeroservoelastic State Space Tools), a software developed by the Department of Aerospace Science and Technology of Politecnico di Milano and implemented in the general-purpose mathematical software MATLAB. MASST is a collection of procedures that can be used to produce multidisciplinary analyses of fixed and rotary wing aircraft (Refs.[13, 17]). The graphic user interface is reported in **Appendix B.1**.

The following Sections describe the many components that are part of the tiltrotor's model. The XV-15 dynamic model set-up includes structural airframe, nacelles, unsteady aerodynamics, rotors, drive-trains, servo-actuation systems, controllers and pilot models.
The modelling of the elastic airframe and of the unsteady aerodynamics represents the most consistent part of the work. Its presentation is split in two phases: Section 2.1 reports the details of the airframe's implementation in MASST, while a more extensive characterisation of the XV-15 finite element (FE) model, developed in NASTRAN, is advanced in Chapter 3.
Other components, including the rotors, the drive train and the RPM governor, are available from previous work; these elements are exported to MASST and are incorporated into the model. The basics of their mathematical models are recalled.
The complete XV-15 MASST model can be visualised in **Appendix B.2** in airplane and helicopter mode configurations.

2.1 Airframe

2.1.1 Elastic Structural Model

The layout of the Bell XV-15, shown in Figure 2.1(a), is similar to a turboprop aircraft but instead of classical airplane props it mounts large helicopter like rotors coupled with turboshafts engines on the wing tips. The rotor axes rotate from the vertical normal position for hover and helicopter flight, to the horizontal for airplane mode flight. The structure of the fuselage and empennage is of conventional semimonocoque design.
According to available open literature (Ref.[15]), the airframe structural model can be outlined as a finite element (FE) stick model consisting of an elastic wing, discretised using ten beam elements, with a rigid fuselage and rigid wing-mounted nacelles. Two concentrated masses model the left and right rotors. The resulting schematisation is depicted in Figure 2.1(b). An extensive description of the tiltrotor's airframe model is proposed in Chapter 3.
This initial model is found not to be fully representative of the real mass distribution of the tiltrotor in airplane configuration (APMODE). Consequently, in Section 3.3, it is performed an updating procedure in order to improve the mass properties' matching.
One of the main issues related to the Bell XV-15 model is due to the rigid connection between the wing tip and the nacelle. To represent the local compliance between the two substructures, it is decided to replace the clamped constraint with lumped angular springs about the nacelle's pitch and yaw axes. In Section 3.5.1 the values assigned to the elastic elements are set to match the APMODE downstop-off frequencies, reported in Ref.[5].

The airframe model of Figure 2.1(b) is modelled in NASTRAN and it is later exported to MASST.

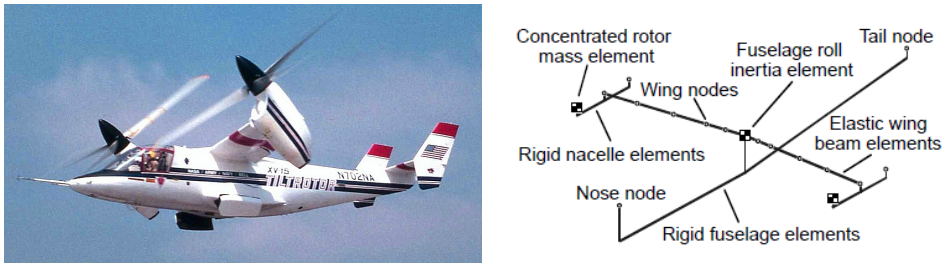

(a) XV-15 Physical Model

(b) XV-15 FE stick model Ref.[15]

Figure 2.1: XV-15 Tiltrotor Aircraft

2.1.2 Nacelle Substructuring

Boundary Mass Substructuring Method

The XV-15 airframe model, obtained in NASTRAN, is exported to MASST considering three separated substructures: one component includes the wing, the fuselage and the tail, whereas the other two describe the rigid nacelles. The nacelle component in MASST has the specific property of being able to rotate about a fixed spindle axis. This allows to handle a single airframe model, which is connected to the substructured nacelles that are parameterised with respect to the pylon conversion angle.

The substructuring approach is based on the Boundary Mass Method proposed by M. Karpel in Ref.[18], which requires the user to add large lumped masses and inertias at the assembly points, that in this case correspond to the wing-tip connections (Fig.2.2). The single boundary mass, described in NASTRAN by a CONM2 element, is characterised by the quantities listed in Table 2.1. The mass value is equal to the whole aircraft weight and the magnitude of the inertias is comparable with the principal moments of the entire tiltrotor.

The dynamic system, composed by the structural airframe and the wing tip boundary masses, is later described by a reduced order model (ROM), necessary for MASST substructuring routine (Ref.[16]). The adopted formal procedure is exposed below.

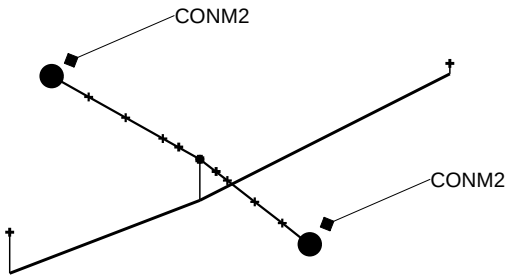

Figure 2.2: Boundary Wing-Tip Masses

	m	$\mathbf{I}_{xx}$	$\mathbf{I}_{yy}$	$\mathbf{I}_{zz}$
CONM2	33.67	1.E+06	1.E+06	1.E+06
units	blob	blob·in^2	blob·in^2	blob·in^2

Table 2.1: Concentrated Mass Element

A physical representation of the tiltrotor's dynamics can be obtained through its equivalent mass and stiffness matrices $\mathbf{M}$ and $\mathbf{K}$, as reported in Equation 2.1. Vector $\underline{u}$ contains the nodes' displacements of the FE model of Figure 2.2.

$$\mathbf{M}\ddot{\underline{u}} + \mathbf{K}\underline{u} = \underline{0} \tag{2.1}$$

The displacement vector $\underline{u}$ can be written as a linear combination of the generalised modal coordinates $\underline{q}$ through the modal matrix $\mathbf{U}$, as shown in Equation 2.2.

$$\underline{u} = \mathbf{U}\underline{q} \quad , \quad \mathbf{U}^{n\times m} = \left[\mathbf{U}_c^{n\times m_c} \mid \mathbf{U}_R^{n\times 6} \mid \mathbf{U}_E^{n\times m_E}\right] \tag{2.2}$$

The modal matrix $\mathbf{U}^{n\times m}$ contains :

- m_c control surfaces modes $\mathbf{U}_c^{n\times m_c}$, output of a SOL101 NASTRAN analysis. These mode shapes, characterised by a rigid rotation of a control surface about the hinges that connect it to the airframe, are required to model the aircraft's manoeuvres. The XV-15 is is provided with seven aerodynamic control surfaces (flaps, flaperons, elevator and rudders), hence seven control surfaces modes are considered;
- six airframe rigid modes $\mathbf{U}_R^{n\times 6}$ related to the global rigid motion of the free-flying aircraft, output of a SOL103 NASTRAN analysis;
- m_E elastic normal modes $\mathbf{U}_E^{n\times m_E}$, output of a SOL103 NASTRAN analysis. The number of included elastic modes is specified in Eq.2.6;

A ROM can be obtained by substituting Equation 2.2 into 2.1 and pre-multiplying by $\mathbf{U}^T$, as shown in Equations 2.3, 2.4 and 2.5.

$$\mathbf{M}_{hh}\ddot{\underline{q}} + \mathbf{K}_{hh}\underline{q} = \underline{0} \tag{2.3}$$

Where

$$\mathbf{M}_{hh} = \mathbf{U}^T\mathbf{M}\mathbf{U} \tag{2.4}$$

$$\mathbf{K}_{hh} = \mathbf{U}^T\mathbf{K}\mathbf{U} \tag{2.5}$$

The mass and stiffness matrices $\mathbf{M}_{hh}$ and $\mathbf{K}_{hh}$ can be obtained as outputs of a SOL103 NASTRAN analysis and they are generally not diagonal.
The result of the condensation procedure is a reduced model defined by matrices $\mathbf{M}_{hh}$, $\mathbf{K}_{hh}$ and $\mathbf{U}$. These quantities are exported to MASST and are used for the substructuring routine. After that, the added boundary wing-tip masses can be removed from the airframe and the substructured nacelles can be integrated as two separated components. According to Ref.[18], this approach allows the reconstruction of the modal content of the original non-substructured model of Figure 2.1(b). Further details about MASST substructuring routine are available in Ref.[16].

Substructured Nacelles

As already mentioned, the nacelles are removed from the original NASTRAN assembly of Figure 2.1(b) and they are re-modelled in MATLAB as substructured components. Here a set of ASCII files, listed below, is compiled and later exported to MASST.

- **.grid** : this file contains the coordinates of the nacelle's structural nodes P_1, P_2 and P_3, represented in Figure 2.3 and listed in Table 2.2.
- **.mass** : this file contains the mass matrix **M** of the substructured component, written with respect to the pivot point P_1 of Figure 2.3. The properties listed in Table 2.3 describe the mass distribution resulting from the nacelle and rotor's assembly. Coherently with Ref.[15], the nacelle is modelled as a bar while the rotor is approximated by a concentrated mass placed at the nacelle's end.
- **.stf** : this file contains the stiffness matrix **K** associated with the substructured component. Since the nacelles are modelled as rigid bodies this matrix is populated by zeroes.
- **.dmp** : this file contains the damping matrix **C** associated with the substructured component. No structural damping is introduced.
- **.mod2** : this matrix contains the modal shapes associated with the substructured component.

Three linear actuators are also modelled to enable the rotor controls, including :

- collective pitch control
- longitudinal cyclic control
- lateral cyclic control

It is specified that the lateral cyclic control is modelled for the sake of completeness since the XV-15 is not provided with this kind of control.
Figure 2.3 shows that each linear actuator is described by means of two points: one, called "fixed" (F), is joint to the nacelle while the other, called "movable" (M), can move along the nacelle axis. The M ends are attached to the rotors, that will be introduced in MASST as further substructures (Section 2.2). The specifics of the hydromechanical servomechanisms associated with the actuators will be described in Section 2.4.
Due to the introduction of the actuators, the **.mod2** file contains the six rigid modes associated with the rigid nacelle and three modes associated with the motion of each linear actuator along the nacelle axis.

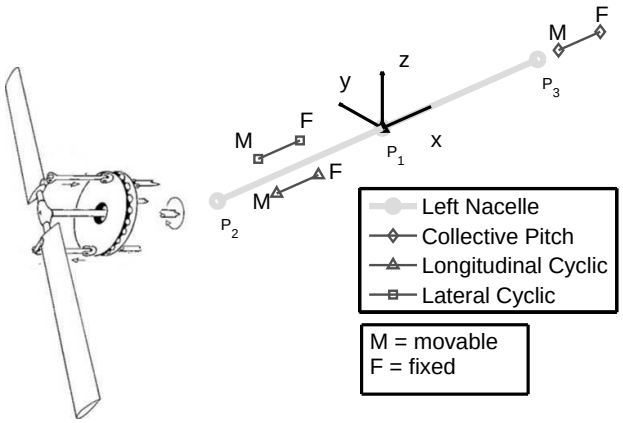

Figure 2.3: Nacelle and linear actuators for rotor controls

Point	x [in]	y [in]	z [in]
P_1	0	0	0
P_2	-47.3	0	0
P_3	44.61	0	0

Table 2.2: Nacelle Grids Ref.[15]

	Value	Units
m	5.545	blob
S_{xy}	36.89	blob·in
S_{yz}	73.90	blob·in
I_{xx}	332.03	blob·in^2
I_{yy}	7906.714	blob·in^2
I_{zz}	7574.680	blob·in^2
I_{xz}	-49.62	blob·in^2

Table 2.3: Nacelle Mass Matrix

Substructuring Validation

The substructuring procedure of the airframe and the nacelles is validated as follows. The aircraft natural frequencies are computed in NASTRAN by means of a SOL103 eigenanalysis. The same analysis is performed in MASST, considering the assembly composed by the airframe and the substructured nacelles. The results are subsequently compared. Tables of **Appendix C** show the eight lowest natural frequencies of the airframe obtained in the two cases, considering a subset of representative nacelle conversion angles and locked aerodynamic control surfaces. It can be observed that the results overlap with very low frequency error.

With reference to Equation 2.2, it is also estimated that the obtained results can be achieved using a minimum modal base $\mathbf{U}^{n\times m}$ of the airframe composed by six rigid modes $\mathbf{U}_R^{n\times 6}$ and twenty elastic modes $\mathbf{U}_E^{n\times 20}$:

$$\underline{u} = \mathbf{U}\underline{q} \quad , \quad \mathbf{U}^{n\times m} = \left[\mathbf{U}_R^{n\times 6} \mid \mathbf{U}_E^{n\times 20}\right] \tag{2.6}$$

2.1.3 Aerodynamic Control Surfaces

In order to develop an aeroelastic model the XV-15, the aerodynamic control surfaces are introduced. This tiltrotor is supplied with two flaperons, an elevator and two rudders. The initial NASTRAN model, developed according to Ref.[15], is modified following the steps listed below.

- as highlighted in Figure 2.4, each structural node of the wing is assigned a rigid and massless BAR2 element to represent the Leading Edge (LE) and Trailing Edge (TE) of the wing. The TE points allow the connection of flaps and flaperons.
- it is modelled a rigid and massless tail to allow the connection of the elevator and the rudders.

The movable surfaces are structurally represented by 2D rigid plates of rectangular shape which are connected to the structure by means of a single point constraint, representing an hinge. Note that, commonly, the movable surfaces are physically connected to the structure through two hinges; reducing the nexus to a single point is an essential approximation not to further constrain the flexible element to which the surfaces are attached and consequently alter its modal behaviour.
No mass is associated with the aerodynamic surfaces as their weight is already included in the total mass of the wing. However, a concentrated inertia (NASTRAN element type CONM2) is applied to the point representing the hinge. The introduction of the surfaces' hinge-referred inertias is quite negligible with respect to the total mass distribution of the tiltrotor, therefore

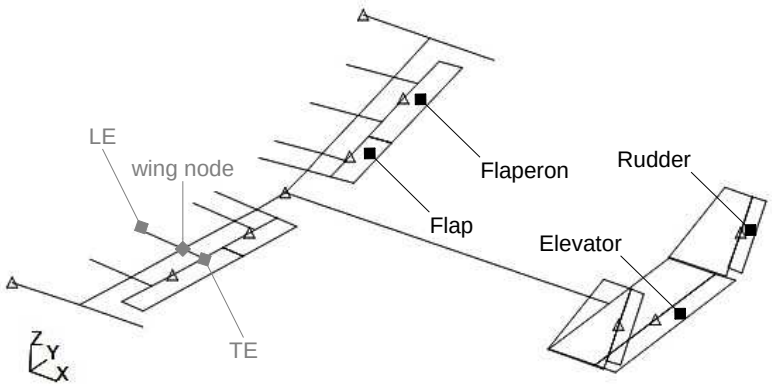

Figure 2.4: FE stick model with movable surfaces

the mass properties and modal characteristics are not altered.
The geometrical data used for surfaces' modelling are derived from Ref.[5] and are reported in Table 2.4, together with the hinge-referred inertias.

	Flap	**Flaperon**	**Elevator**	**Rudder**	**units**
Span	50.98	94.3307	144	55.91	in
Chord	15.50	15.44	14.11	9.70	in
Hinge Inertia*	3	4	3.5	1.5	blob·in^2

Table 2.4: Control Surfaces Data Ref.[5]

*The values are given for the single flap, flaperon and rudder

2.1.4 Unsteady Aerodynamics

The unsteady aerodynamics contribution is evaluated in the frequency domain using the Doublet Lattice Method (DLM), implemented in NASTRAN. The DLM is in use worldwide for flutter and dynamic analysis of aircraft at subsonic speeds. It is a classic tool for aeroelastic calculation, which makes it "the de facto" standard method for aeroelasticity in aerospace industry. The theoretical basis of the DLM is the potential flow based panel method (Refs.[20, 21, 22]). Each aerodynamic surface is discretized into trapezoidal boxes whose edges are aligned with the free stream, as represented in Figure 2.5. On each discrete lifting element it is imposed a steady horseshoed vortex, that represents the steady-flow effect, and an oscillatory doublet, that describes the periodical contribution. The lifting vortex ring is placed at quarter box chord while the normalwash boundary condition is applied at the control point, centred spanwise on the three-quarter line of the box.

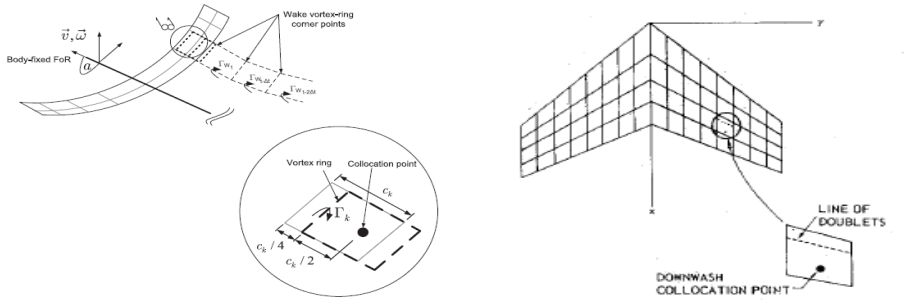

Figure 2.5: DLM, Doublet Lattice Method

In the frequency domain, the relationship between the modal aerodynamic forces $\underline{F}_a(j\omega)$ and the generalised coordinates $\underline{q}(j\omega)$ can be expressed as in Equation 2.7.

$$\underline{F}_a(j\omega) = q_\infty \cdot \mathbf{H}_{am}\Big(k, M\Big)\underline{q}(j\omega) \tag{2.7}$$

The matrix $\mathbf{H}_{am}\Big(k, M_\infty\Big)$ contains the generalised aerodynamic forces due to the modal displacements as functions of the reduced frequency k and the Mach number M. The dynamic pressure is indicated by q_∞.

$$k = \frac{\omega \cdot l}{V_\infty} \qquad M_\infty = \frac{V_\infty}{c_\infty} \qquad q_\infty = \frac{1}{2} \cdot \rho_\infty \cdot V_\infty^2 \tag{2.8}$$

ω indicates the natural frequency, l is the reference length equal to the half mean aerodynamic wing chord, V_∞ is the unperturbed free stream velocity, c_∞ is the speed of sound and ρ is the air density.

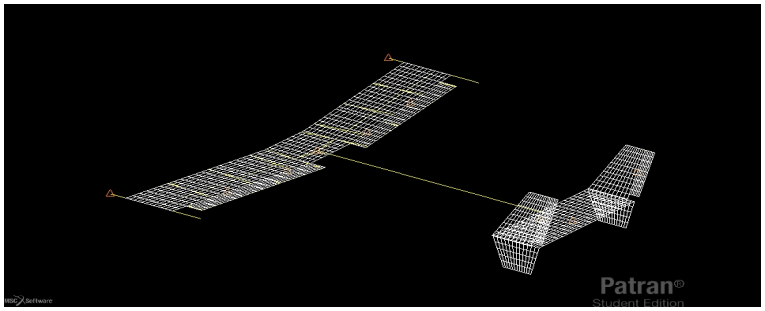

Figure 2.6: DLM - aerodynamic boxes

The unsteady aerodynamic properties are obtained running a SOL146 NASTRAN analysis (Ref.[23]). This NASTRAN procedure provides a list of aerodynamic matrices $\mathbf{H}_{am}$ scheduled with respect to the reduced frequencies and to the Mach numbers specified in the input file. The card that is compiled for a SOL146 also requires the indication of the wing chord length and the air density, reported in Table 2.5.

The XV-15 adopted aerodynamic mesh is represented in Figure 2.6. A total number of twelve panels has been modelled; in particular the wing is separated into right semi-wing, left semi-wing, and a center section representing the fuselage. Four panels are modelled to capture the rigid movements of the flaps and flaperons. The tail is modelled by means of six panels to recover the displacements of the horizontal tail, the elevator, the vertical fins and the rudders. The DLM is applied only on the airframe base structure, neglecting any aerodynamic interference of the nacelles.

The panels, whose discretisation is reported in Table 2.6, are meant to deform like the elastic structure. It is recalled that the only elastic element of the structure is the wing, and the other structural elements are supposed to be rigid. The aerodynamic discretisation is not coincident with the structural mesh and, to verify the goodness of the aero-structural interpolation, it is possible to graphically visualise the panels' deflection, to ensure that they deform coherently. In Figure 2.7 it is reported, by way of example, the

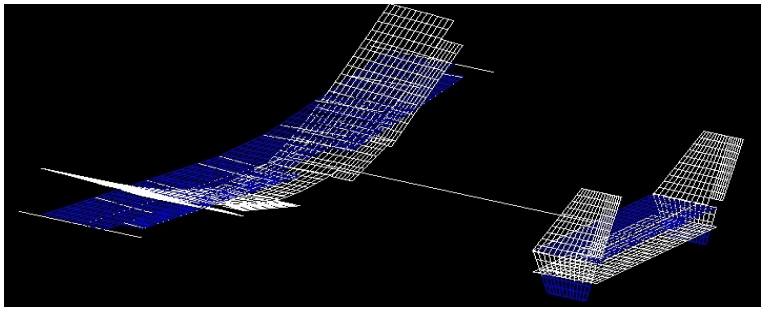
Figure 2.7: DLM - aerodynamic boxes' deformation

aerodynamic mesh deflection after an out-of-plane bending deformation. According to NASTRAN's manual (Ref.[23]), the minimum chordwise discretisation needed to capture a phenomenon at speed v and frequency f should respect the constraints reported in Equation 2.9.

$$\Delta x \leq 0.02 \cdot \frac{v}{f} \qquad\qquad \frac{\Delta y}{\Delta x} \leq 3 \tag{2.9}$$

The aerodynamic discretisation has been designed to capture the oscillating phenomena up to 10 Hz and the airspeeds covered by the tiltrotor's conversion corridor.

The unsteady aerodynamics' data obtained in NASTRAN are exported to MASST. In MASST the aerodynamic forces are approximated using Roger's formulation (Ref.[24]). Despite its easy implementation, a large number of states is required by Roger's technique to obtain an acceptable level of accuracy. A model condensation can be performed in MASST using a balance truncation procedure whose details are available in Ref.[25].
At the end of the whole procedure, the unsteady aerodynamic data can be visualised in MASST in a plot that reports the real and imaginary parts of each aerodynamic influence coefficient, scheduled with respect to the reduced frequency and the Mach number. By way of example, Figure 2.8 depicts the trend of the generalised aerodynamic coefficient $\mathbf{H}_{am}(3,5)$, which represents the generalised aerodynamic force on mode 3 due to mode 5, at Mach 0.2 and reduced frequencies spacing from 0 to 2. A sixth order Roger's approximation is applied to interpolate the available data.

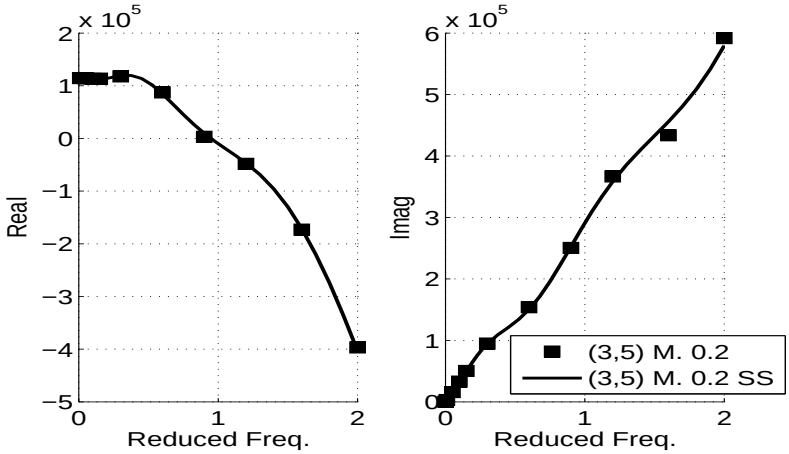

Figure 2.8: Frequency domain aerodynamic transfer function

density	1.146E−07	lbf·s^2/in
wing chord	63.00	in

Table 2.5: NASTRAN SOL146

Panel	N chordwise	N spanwise
Semiwing	12	20
Flap	6	6
Flaperon	6	12
Fuselage	12	7
Horizontal Tail	7	20
Elevator	5	20
Vertical Tail	12	15
Rudders	6	9

Table 2.6: Panels Discretization

2.2 Aeroelastic Rotors

The rotors' models, available from previous work, are connected to the tiltrotor's airframe. They are developed in CAMRAD/JA, a software dedicated to aerodynamic and dynamic study of rotorcrafts, following the guidelines of Ref.[26], by C.W. Acree. The XV-15 mounts a 25-ft-diameter gimbal-mounted, stiff-in-plane, three-bladed rotors (Ref.[5]).

The rotor's dynamics is described by non linear ordinary differential equations (ODE) which are linearised for a representative subset of trim configurations, highlighted in Figure 2.9(a). The rotors' representation for other intermediate configurations can be obtained in MASST using the interpolation procedure (Ref.[16]). As a result, a single non linear rotor model is replaced by a chosen number of linear time invariant (LTI) rotor models.
The aeroelastic models are based on the beam theory for rotating wings with large pitch and twist. The aerodynamics is based on Drzwiecki Blade Element Theory (BET), assuming that each blade section acts as a two dimensional airfoil to produce aerodynamic forces (Ref.[29]).

The models obtained in CAMRAD/JA are later exported to MASST, where the rotor dynamics is described by second-order quasi-steady approximation:

$$\mathbf{M}\ddot{q} + \mathbf{C}\dot{q} + \mathbf{K}q = \mathbf{B}_\theta\theta + \mathbf{G}_g v_g \tag{2.10}$$

Vector q represents the degrees of freedom of the rotor in the non-rotating reference frame using multi-blade coordinates (MBC), θ corresponds to the collective and cyclic pitch inputs, and v_g is the gust velocity. The matrices $\mathbf{M}$, $\mathbf{C}$, $\mathbf{K}$, $\mathbf{B}$ and $\mathbf{G}$ are characterised by constant coefficients and the periodic quantities are averaged over a revolution (Ref.[16]).

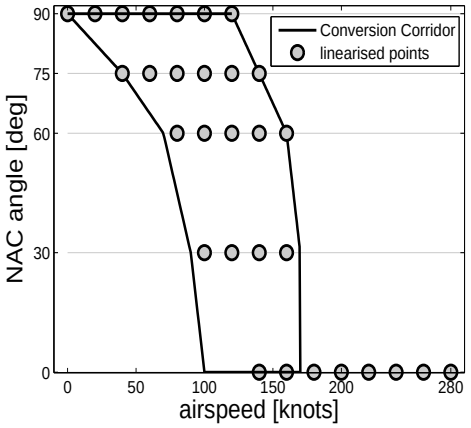

(a) XV-15 Conversion Corridor

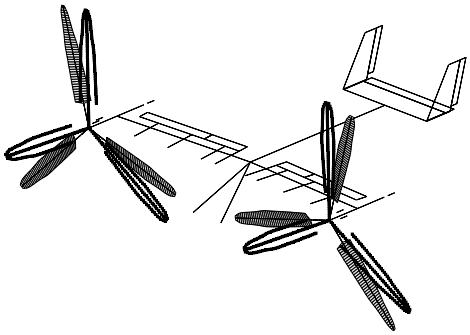

(b) MASST XV-15 Model with Rotors

Figure 2.9: Aeroelastic Rotors

CAMRAD J/A is used to generate the rotor dynamic equations and the blade normal modes of the right rotor. Exploiting the symmetry, the left rotor can be obtained in MASST using a *mirror* function (Ref.[16]).
In MASST the XV-15 rotor's dynamics is described including the following degrees of freedom (DoF) :

- three bending modes, in particular two flapping modes and a lead/lag mode. Each mode is described by a collective mode and two cyclic modes (MBC, 9 DoFs).
- the pitch mode and one torsion mode, each described by a collective mode and two cyclic modes (MBC, 6 DoFs).
- the gimbal modes, each described by two cyclic modes (MBC, 2 DoFs).
- the axial inflow, Ref. [30] (1 DoF)
- the rotor speed (1 DoF)

The single rotor is connected to the nacelle according to Craig-Bampton's substructuring technique (Ref.[13]) and six rigid modes are introduced to describe the rigid hub motion. As a result, a total number of 25 DoFs is involved in the description of the rotor's dynamics.
The rotors are subsequently connected to the drive train, described in Section 2.3, and to the nacelle's collective and cyclic servo-actuators, already presented in Section 2.1.2. Figure 2.9(b) shows a MASST visualisation of the XV-15 model provided with rotors. The blades with black solid lines indicates the rotor's initial position at zero azimuth, while the painted ones are rotated by 15 degrees.

2.3 Drive Train and RPM "Beta" Governor

The drive train model is derived from previous work and it is exported to MASST. Currently the drive train dynamics can be modelled in MASST using simplified one-dimensional models consisting in a set of torsional springs and equivalent lumped inertias (Ref.[16]).

The Lycoming LTClK-4K engines (a modification of the T53-L-13B) and main transmissions are located in wing-tip nacelles. The drive train model is based on the symmetric architecture proposed in Ref.[28] and depicted in Figure 2.10. The engines are characterised by means of a rotational inertia I_E and they are connected to the rotors by left and right transmissions. The connections between the engine, the transmissions and the rotors are supported by shafts of torsional stiffnesses K_E and K_M. The reduced parameters I_E, K_E and K_M are derived from Ref.[26]. The two rotors are joined by an interconnecting shaft, which precludes the complete loss of power to either rotor due to a single engine failure, permits power transfer for transient conditions and provides rotational speed synchronisation (Ref.[5]). The drive train MASST model is depicted in Figure 2.11 and further details about its implementation are available in Ref.[16].

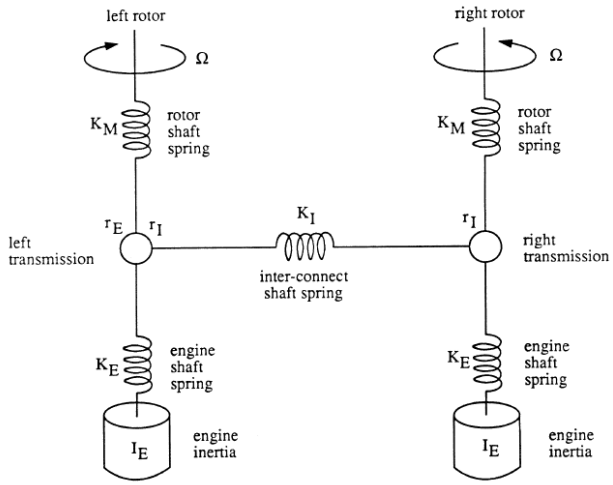

Figure 2.10: Schematic of Rotorcraft Transmission and Engine Dynamics model Ref.[28]

The XV-15 aeroelastic model is also integrated with a RPM "Beta" Governor, developed in previous work. It is a closed loop system that maintains a pilot-selected RPM by controlling collective blade pitch. The pilot sets engine power and the governor adjusts the propeller angle of attack to maintain the RPM (Ref.[31]).

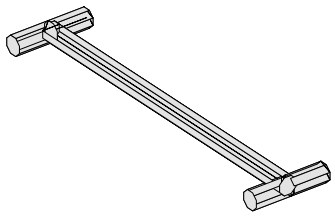

Figure 2.11: MASST drive train model

The governor control law, reported in Refs.[31] and [32], is a PI controller that considers as input the error between the requested RPM and the measured rotor speed. The controller's gains are scheduled with respect to the nacelle conversion (NAC) angle (Ref.[32]). Further details are specified in Section 6.1.

2.4 Servo-Actuators

In MASST the aerodynamic surfaces' deflection (flaps, flaperons, elevator, rudders) and the rotors' inputs (collective, longitudinal and cyclic pitch) are actuated by hydromechanical servomechanisms, used for position control. A short mathematical model description of the servo-valves is presented in the following and more details are available in Ref.[33], Chapter 9.
With reference to Figure 2.12, the servo-actuator linear dynamics can be represented, in the frequency domain, by the expression reported in Equation 2.11, where x and x_c correspond, respectively, to the displacement of the linear actuator and to the requested input displacement. F_c is the reaction force necessary to obtain the control surface deflection. Equation 2.11 can be written with respect to angular motion β as a function of the appropriate gear ratio b (Eq. 2.13).

$$x = H_c(s) \cdot x_c + H_m(s) \cdot F_c \tag{2.11}$$

$$x = \beta \cdot b \qquad\qquad M_c = F_c \cdot b \tag{2.12}$$

$$\beta = H_c(s) \cdot \beta_c + \frac{H_m(s)}{b^2} \cdot M_c \tag{2.13}$$

In MASST each servo actuator is characterised by the transfer functions $H_c(s)$ and $H_m(s)$. $H_c(s)$ represents the closed loop response to reference inputs and it is described by a second order low pass Butterworth filter with a cut off frequency of 15 Hz. The dynamic compliance $H_m(s)$ is instead approximated by a constant. Further details about the servo actuators' implementation in MASST are available in Ref.[16].

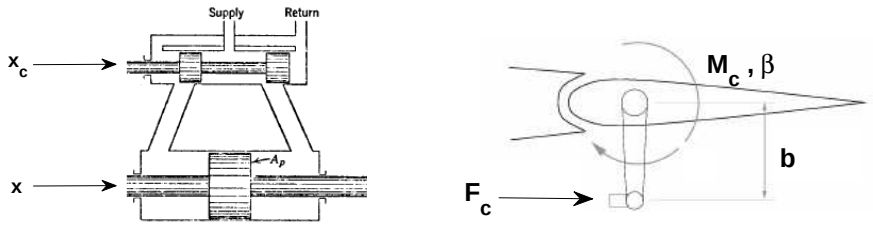

(a) Hydromechanical Servo (b) Actuator Load

Figure 2.12: Linear Actuator Scheme

2.5 Pilot/Control Device BDFT

2.5.1 Pilot-in-the-Loop Scheme and Cockpit Layout

Pilot-in-the-loop stability analysis is performed by introducing pilot/control device elements in feedback loop with the tiltrotor aeromechanics (Figure 2.13). As mentioned in Section 1, the investigation of PAO phenomena requires the introduction of involuntary pilot's models. The pilot's passive biomechanics can be described using a transfer function that characterises the biodynamic feedthrough (BDFT), i.e. involuntary control inceptor motion caused by cockpit accelerations transmitted to the pilot's body. BDFTs are usually obtained from experimental shake tests, during which sinusoidal commands are applied to the simulator platform, with the pilot sitting in the seat and hands on the controls. As a result, the measured bio-response includes both the pilot's biodynamics and the control inceptor dynamics (pilot/control device dynamics).
In MASST the pilot's BDFT is introduced as a controller, since it is actually a control system that takes as input the acceleration a_{seat}, measured at the pilot's seat, and acts on appropriate actuators.

Due to structural vibrations, the pilot can inadvertently act over the control commands. It is consequently necessary to present the XV-15 cockpit layout, shown in Figure 2.14. The cockpit controls consist of a longitudinal/lateral stick, a collective-type power lever (PL) and pedals for the pilot and copilot. A three-position switch on each power lever controls the nacelle conversion angle. Pilot controls in the HEMODE are similar to that of a conventional helicopter. The PL provides power and collective pitch for height control and a control stick provides longitudinal and lateral control. In the APMODE, conventional airplane stick and rudder pedals are employed, while the collective stick/power lever continues to be used for power management

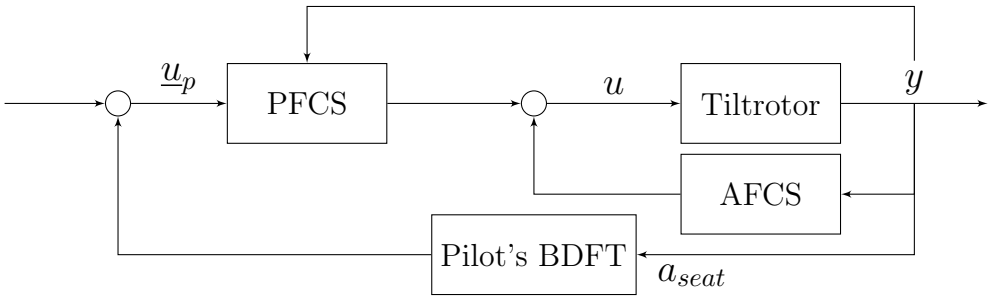

Figure 2.13: General PVS scheme

(Ref.[5]). The XV-15 control paths are further clarified in **Appendix A**, that presents a general schematics of the PFCS control mixing.

Figure 2.14: XV-15 Cockpit Layout

In Chapters 4, 5 and 6 Pilot-in-the-Loop stability analyses are performed separately along the longitudinal, lateral and vertical axes. On each axis, the pilot model is defined by a transfer function.

1. A pilot longitudinal axis transfer function is derived from Ref.[11]. This work presents the results of Pilot-in-the-Loop aeroelastic analyses conducted for the V-22. The pilot's BDFT is identified measuring the longitudinal displacements of the stick in response of longitudinal cockpit accelerations.
2. A pilot lateral axis transfer function is described in Ref.[34], where three trained test pilots are considered in a biodynamic feedthrough characterisation. In this work it is examined the relationship between the pilot's lateral cyclic stick control input and the subsequent vehicle motion in the lateral direction.
3. Finally the pilot vertical axis transfer function is derived from Ref.[12]. In this case pilot's collective stick motion is recorded, while vertical sinusoidal commands are applied to the simulator platform at discrete frequencies ranging from 1 to 5 Hz. In this case the results are experimentally obtained from two sets of pilots, distinguished into ectomorphic (small and lean build) and mesomorphic (large bone structure and muscle build).

As a result, pilot biomechanical models are available about the vertical, lateral and longitudinal axes and cross-coupled effects are assumed negligible. The details about the pilot's BDFTs are reported in Sections 4.1.1, 5.1.1 and 6.1.1.

2.5.2 Robust Stability Analysis of SISO systems

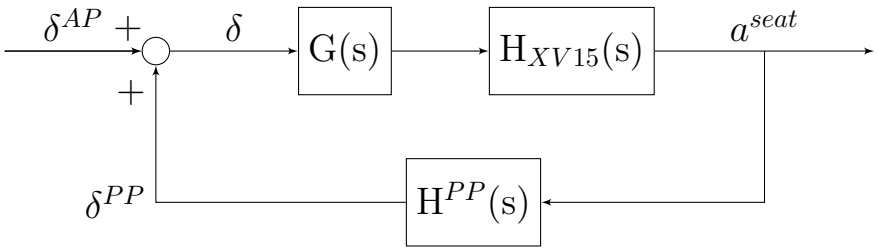

Figure 2.15: Closed Loop System SISO Dynamics

In the following it is described the generalised approach through which PAOs are investigated. The same method is also employed in other References (e.g. [9, 14, 34]), and represents a standard for this kind of analysis.

As already mentioned, PAO analyses are performed separately along the longitudinal, lateral and vertical axes, due to the impossibility to handle a single pilot-model representative of the complete biodynamics over the three axes. Along each axis the pilot is described by a single-input single-output (SISO) transfer function that takes as input a longitudinal/lateral/vertical acceleration and generates as output a longitudinal/lateral motion of the stick or a vertical displacement of the power lever. In other words, the pilot is modelled as a passive element that senses a linear acceleration along a single axis and acts over a single control command, neglecting possible cross-coupled effects. After a longitudinal/lateral acceleration the pilot transmits the vibrations to the only longitudinal/lateral stick and after a vertical acceleration the oscillations are conveyed to the power lever.
Therefore the dynamics of the closed loop PVS, along a single axis, can be described as a SISO system, whose general scheme is reported in Figure 2.15. The deflection δ of a control input (this could be a longitudinal/lateral movement of the stick or a vertical displacement of the power lever), amplified by G(s), generates, through the tiltrotor's dynamics $H_{XV15}(s)$, an acceleration a^{seat} along the longitudinal/lateral/vertical axis. This acceleration, measured at the pilot's seat, is supposed to excite the biodynamic involuntary response of the pilot, described by the transfer function $H^{PP}(s)$. The involuntary response generates a control device motion δ^{PP} providing a feedback to the open loop tiltrotor's dynamics.
The subscripts AP and PP of Figure 2.15 stand for *active pilot* and *passive pilot*. The active pilot is not modelled and the influence of a voluntary pilot's input δ^{AP} is not contemplated.

The loop transfer function (LTF) of the closed loop SISO system of Figure 2.15 can be expressed as :

$$\text{LTF(s)} = -\, G(s) \cdot H_{XV15}(s) \cdot H^{PP}(s) \tag{2.14}$$

The tiltrotor transfer function H_{XV15} is generated from the state space model created in MASST using the *Simulink Time Response & Nonlinear* routine (Ref.[16]). The pilot's BDFT $H^{PP}(s)$ is instead derived, for each of the three axes, from known open literature, as mentioned in Section 2.5.1. $G(s)$ is defined in Equation 2.15 by the product of a gear ratio G_0 and an exponential function, that introduces possible control device time delays τ. G_0 relates the control inceptor deflection and the corresponding control surface rotation, while time delays can be justified by digital acquisition, filtering of control device motion or by signal processing before feeding inputs to the actuators (Ref.[14]).

$$G(s) = G_0 \cdot e^{-\tau \cdot s} \tag{2.15}$$

With the introduction of the pilot, the system is studied using robust stability analysis techniques, specifically Nyquist criterion (Refs.[35, 36]). According to this criterion, the stability of a system can be evaluated by means of two indexes : the gain and phase margins of the LTF. In order for a system to be stable, both margins have to be positive. Once that this constraint is satisfied, the degree of robustness can be quantified by looking at the magnitude of the stability margins. To obtain robust systems it is necessary to reach a gain margin above 6 decibel and a minimum phase margin of 60 degrees.

Chapter 3

Airframe Elastic Model

3.1 XV-15 Finite Element Model

This Chapter is dedicated to the development of an airframe model representative of the Bell XV-15. The layout of this tiltrotor is similar to a turboprop aircraft but instead of classical airplane props it mounts large helicopter like rotors coupled with turboshafts engines on the wing tips. The rotor axes rotate from the vertical normal position for hover and helicopter flight, to the horizontal for airplane mode flight. The structure of the fuselage and empennage is of conventional semimonocoque design.
Figure 3.1 compares the physical XV-15 model with the simplified finite element (FE) scheme proposed by C.W. Acree in Ref.[15]. The airframe structural model can be outlined as a stick model, consisting of an elastic wing, discretised using ten beam elements, with a rigid fuselage and rigid wing-mounted nacelles (Fig. 3.1(b)). The left and right rotors are represented by two lumped masses.
As already mentioned in the Introduction Section, PAOs typically occur in a frequency range between 2 and 8 Hz. The XV-15 schematisation advanced by Acree captures the first six normal modes of the wing, whose

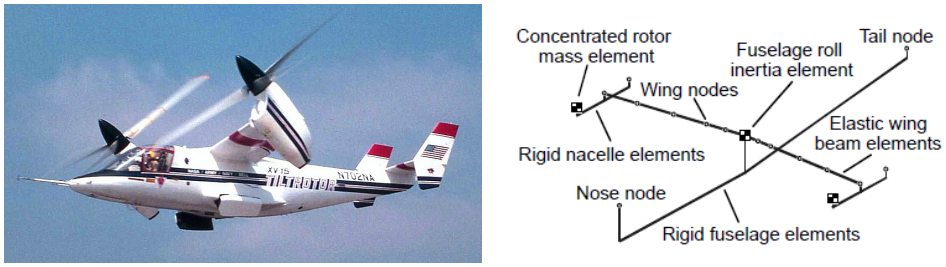

(a) XV-15 Physical Model

(b) XV-15 FE model Ref.[15]

Figure 3.1: XV-15 Tiltrotor Aircraft

natural frequencies are comprised between 3.3 and 8.7 Hz. As a result, the FE stick model of Fig.3.1(b) describes the tiltrotor's dynamics in the typical frequency range of PAO phenomena and it is consequently adopted to represent the tiltrotor's structural airframe. NASTRAN is chosen as mathematical work environment.

The XV-15 stick model, depicted in detail in Figure 3.2, is based on the XV-15 geometry, weights and wing's structural characteristics. The number and type of NASTRAN elements, associated with each structural component, is reported in Table 3.1.

Component	**Element Type**	**NASTRAN**	**N° Elements**
Wing	Elastic Beam	BAR	10
Left and Right Nacelles	Rigid Beam	RBE2	4
Left and Right Rotor	Lumped Mass	CONM2	2
Fuselage	Rigid Beam	RBE2	2
	Roll Inertia	CONM2	1

Table 3.1: XV-15 FE characteritics Ref.[15]

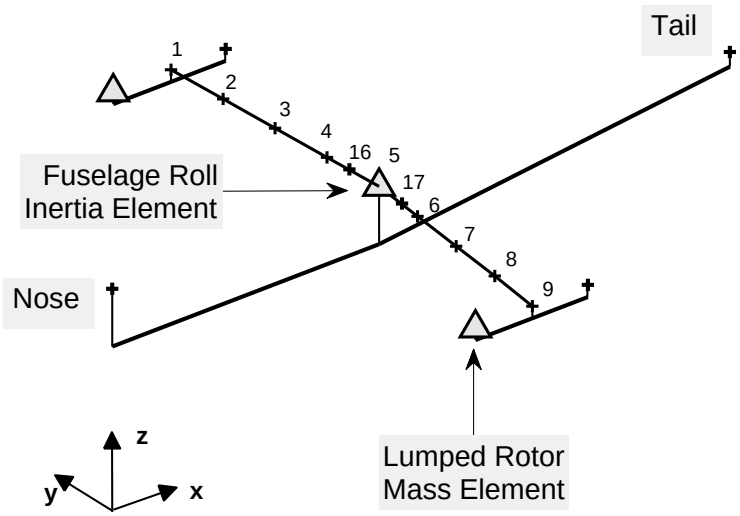

Figure 3.2: NASTRAN XV-15 FE stick model

The wing's geometry is described by the properties listed in Table 3.2. The elastic wing, depicted in Figure 3.2, is discretised using ten beam elements, whose lengths are specified in Figure 3.3. Each element is characterised by bending and torsional stiffnesses, also reported in Table 3.2. The wing is assumed rigid in torsion and chord bending between the wing-to-fuselage mounting points, numbered 16 and 17 in Figure 3.2. This is done to account for the high stiffness created by the fuselage structure (Ref.[15]). Since no information about the wing's mass distribution is available, the weight is uniformly distributed along the span. It is specified that fuel, cross shafting, etc. are included into the total mass of the wing.

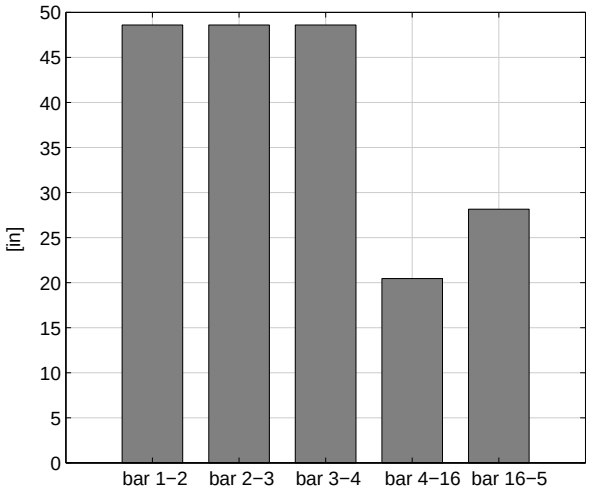

Figure 3.3: Lengths of the wing's FEs, Ref.[15]

Wing Characteristics	**Value**	**units**
Mass	2534	lb
Span	386	in
Dihedral	2	deg
Sweep	-6.5	deg
Out-of-plane Bending Stiffness	3.70E+09	$\text{lb}\cdot\text{in}^2$
In-plane Chord Stiffness	1.12E+10	$\text{lb}\cdot\text{in}^2$
Torsion Stiffness	2.80E+09	$\text{lb}\cdot\text{in}^2$

Table 3.2: Wing Characteristics, Ref.[15]

The nacelles are modelled as rigid bars and, according to Ref.[15], they are located below the plane of the wing by a distance of 9 inches (Figure 3.2). The nacelles characteristics are resumed in Table 3.3. It should be noted that the nacelles' weight equals about a third of the entire mass of the aircraft and, as a consequence, the tiltrotor conversion manoeuvre causes the center of mass to move quite significantly.

Nacelle Characteristics	**Value**	**units**
Weight_{RX+SX}	3166	lb
Length	91.91	in
Offset Δ_z	-9.00	in

Table 3.3: Nacelle Characteristics Ref.[15]

The rotors are approximated by two lumped mass elements located at the nacelles' tips. Unlike the nacelles, the rotors are retained in the plane of the wing and no vertical offset is applied. The rotors' characteristics are listed in Table 3.4.

Rotor Characteristics	**Value**	**units**
Weight_{RX+SX}	1118	lb
Length	0	in
Offset Δ_z	0	in

Table 3.4: Rotor Characteristics Ref.[15]

The fuselage is considered rigid and, as for the nacelles, it is located below the plane of the wing by an offset of 43.2 inches; according to Ref.[15], a lumped roll inertia element I_{xx} is added to the fuselage to lower the asymmetric wing bending (AWB) frequency. This is done to match the AWB of a more detailed NASTRAN model, whose natural frequencies are available in the same reference. The fuselage weight includes equipment, crew and payload.

Fuselage Characteristics	**Value**	**units**
Weight_{RX+SX}	6182	lb
Length	505.20	in
Offset Δ_z	-43.2	in
I_{xx}	5.80E+04	blob·in^2 *

Table 3.5: Fuselage Characteristics Ref.[15]

*blob = lb·sec^2/in

The weights of the wing's components are resumed in Table 3.6. It should be noted that some geometrical data are not specified in Ref.[15]. All the missing quantities are estimated from Figure 3.4 of Ref.[5].

The complete bulk file, implemented for NASTRAN analysis, is listed in **Appendix D.1**. Such file provides a description of the aircraft's geometry and it contains the structural nodes (GRIDS), their connection (CBAR) and the associated elastic properties (PBAR).

Component	**Weight [lb]**
Wing	2534
Left and Right Nacelle	3166
Left and Right Rotor	1118
Fuselage	6182
Design Gross Weight	**13.000**

Table 3.6: XV-15 weights Refs.[15], [5]

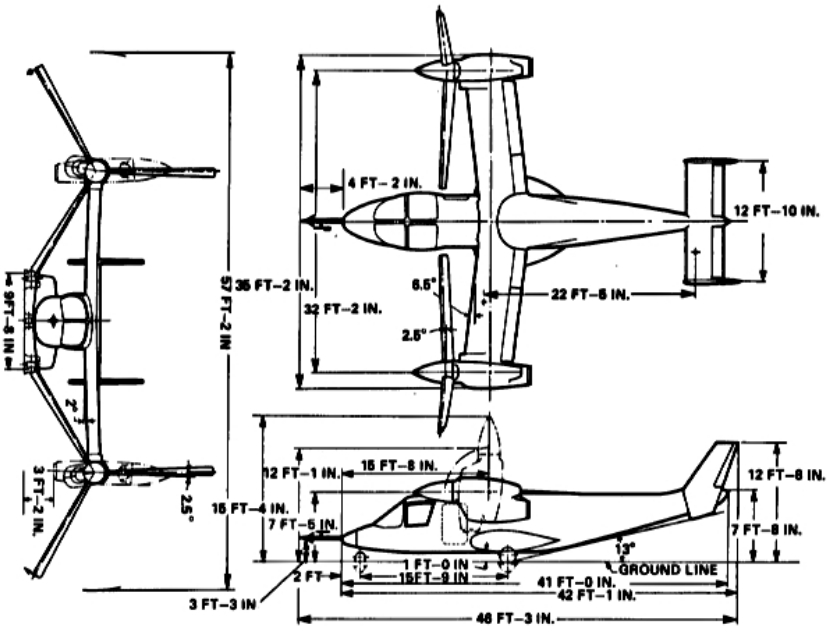

Figure 3.4: XV-15 Geometry Ref.[5]

3.2 Modal Validation

The XV-15 FE stick model presented by C.W. Acree in Ref.[15] is aimed to capture the six lowest natural frequency modes of the wing. These modes correspond to symmetric/asymmetric wing bending (SWB/AWB), symmetric/asymmetric wing chord (SWC/AWC) and symmetric/asymmetric wing torsion (SWT/AWT), represented in Figure 3.5.

The NASTRAN card used to perform the eigenvalue analysis corresponds to a SOL103 (Ref.[23]). The output text file (.f06) lists the airframe natural frequencies and the modal shapes associated with each structural node specified the input file (**Appendix D.1**).
The natural frequencies, the modal masses and the right-hub modal shapes, obtained using NASTRAN, are compared with the corresponding results presented by Acree in Ref.[15]. Figures 3.6 and 3.7 demonstrate that the natural frequencies and the modal masses overlap with very good approximation. The relative errors, listed in Tables 3.7 and 3.8, confirm an excellent match. Also the right hub modal shapes of Fig.3.8 show a good agreement with predicted results. **Appendix D.3** reports the visualisations of the six lowest airframe modal shapes (S/AWB, S/AWC, S/AWT).

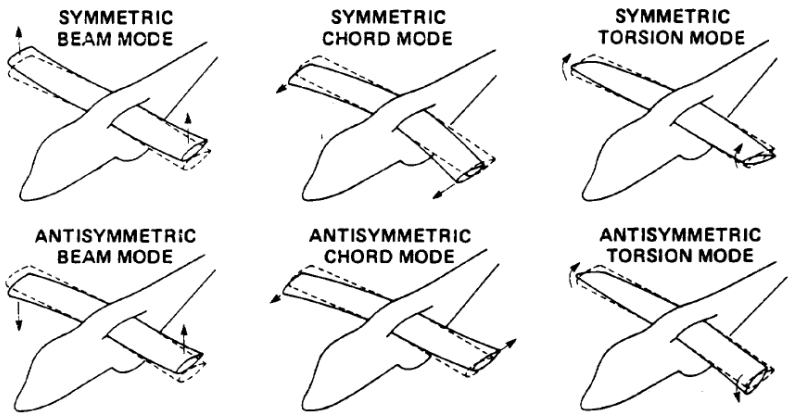

Figure 3.5: XV-15 six lowest elastic wing modes Ref.[1]

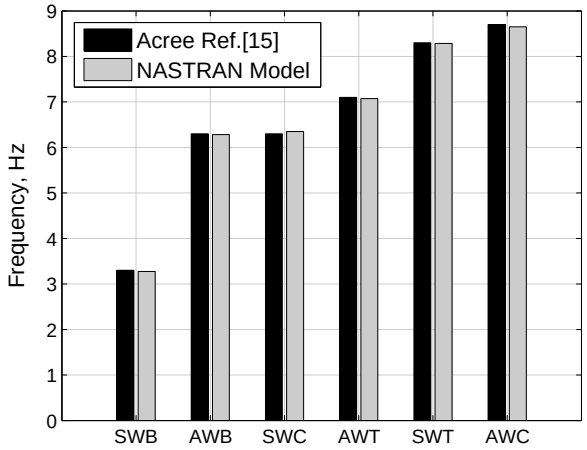

Figure 3.6: Airframe Natural Frequencies

Mode Name	**SWB**	**AWB**	**SWC**
err %	0.7848	0.2567	0.7914
Mode Name	**AWT**	**SWT**	**AWC**
err %	0.3443	0.1798	0.5770

Table 3.7: Airframe Natural Frequencies Error

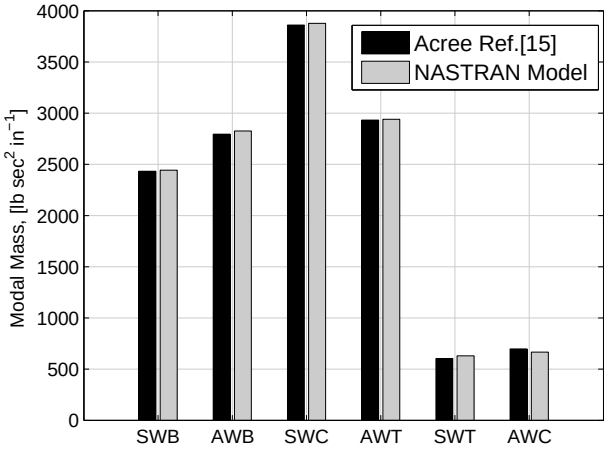

Figure 3.7: Airframe Modal Masses

Mode Name	**SWB**	**AWB**	**SWC**
err %	0.4272	1.1215	0.4389
Mode Name	**AWT**	**SWT**	**AWC**
err %	0.2832	-4.2222	4.3512

Table 3.8: Airframe Modal Masses Error

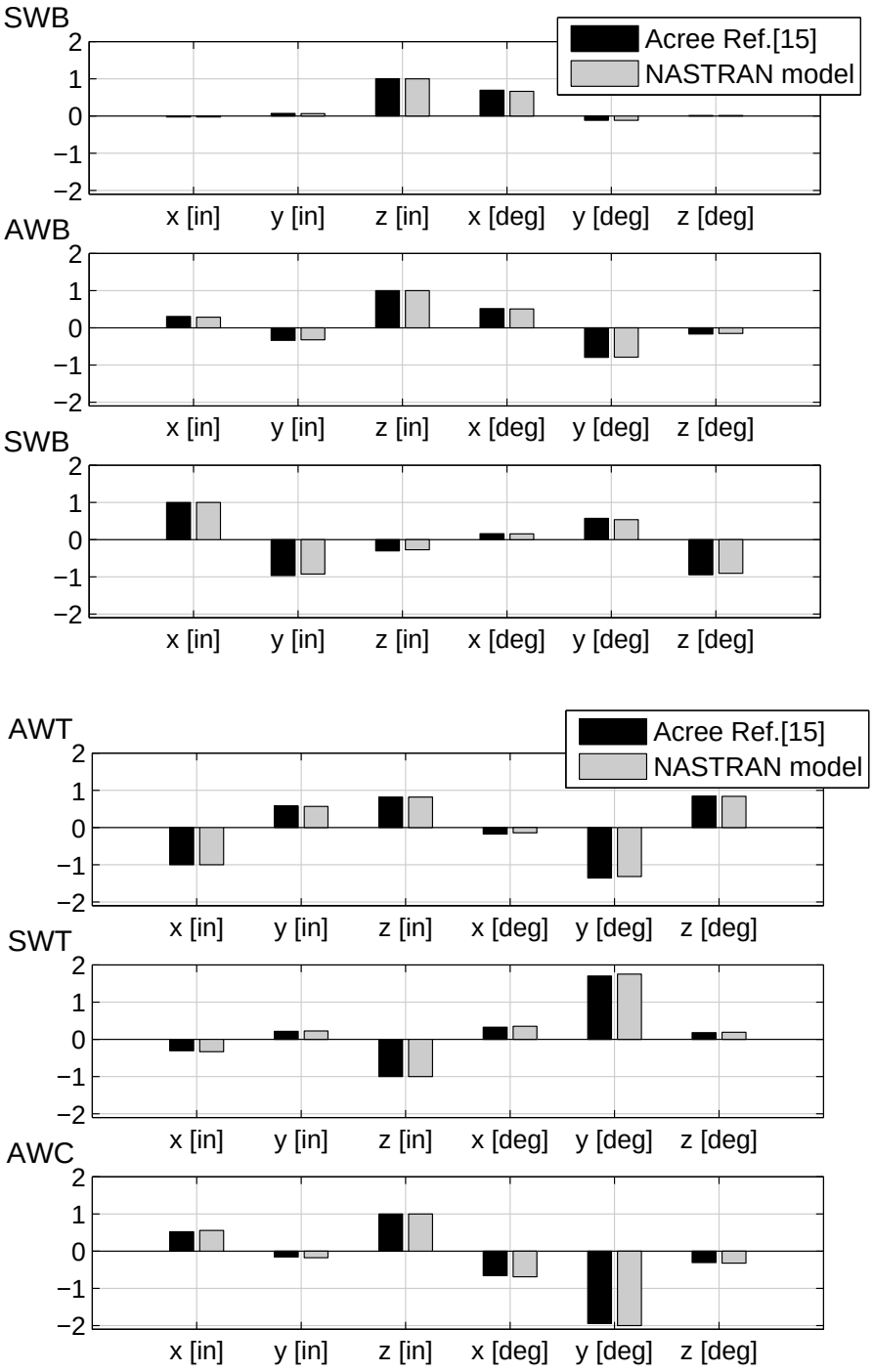

Figure 3.8: Right Hub Mode Shapes

3.3 Mass Properties Validation

The nominal XV-15 mass properties are derived from Ref.[28], where the tiltrotor is analysed in CAMRAD/JA considering the design gross weight (13.000 lb) configuration and airplane mode flight. The reference system adopted in CAMRAD/JA differs from NASTRAN's. Figure 3.9 clarifies the location of the two references' origins and Table 3.9 reports the station and water lines offsets that must be applied to translate NASTRAN into CAMRAD reference system.

NASTRAN and CAMRAD mass properties are compared in Tables 3.10 and 3.11. It can be observed that NASTRAN inertias do not match CAMRAD's and the computed error is large. Also the center of mass location is widely incorrect. This mismatch may not be surprising; in Ref.[15] it is proposed a simplified XV-15 model that represents the six lowest modal shapes of the airframe by means of a very reduced set of parameters. These parameters have been tuned by Acree to match the XV-15 natural frequency modes predicted by a more detailed XV-15 FE model. As a matter of fact, this process only ensures to correctly represent the modal behaviour of the tiltrotor, but it does not guarantee a realistic characterisation of the aircraft's mass properties. Considering it essential to have a XV-15 model with a more reliable mass distribution, it is performed an updating procedure in order to match the tiltrotor's actual specifics.

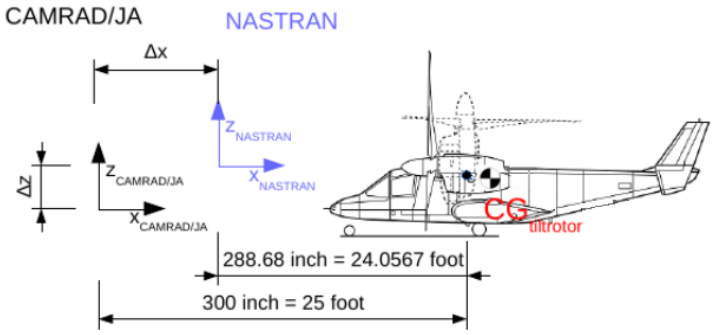

Figure 3.9: NASTRAN and CAMRAD/JA reference systems

Offsets	Δx	Δy	Δz	units
	11.32	0	93.256	in

Table 3.9: NASTRAN to CAMRAD offsets

	$\mathbf{I}_{xx}[\text{blob} \cdot \text{in}^2]$	$\mathbf{I}_{yy}[\text{blob} \cdot \text{in}^2]$
CAMRAD	6.1138E+05	2.4417E+05
NASTRAN	5.6883E+05	5.8469E+05
err %	6.9598	139.4625
	$\mathbf{I}_{zz}[\text{blob} \cdot \text{in}^2]$	$\mathbf{I}_{xz}[\text{blob} \cdot \text{in}^2]$
CAMRAD	8.0599E+05	1.2910E+04
NASTRAN	1.0672E+06	1.8452E+04
err %	32.4184	42.9132

Table 3.10: XV-15 APMODE mass properties

	x_G	z_G	units
CAMRAD	296.880	72.828	in
NASTRAN	324.836	77.656	in

Table 3.11: XV-15 APMODE Center of Mass location

The tiltrotor's stick model is structurally modified; the rigid beam that represents the fuselage (Fig.3.2) is replaced by a lumped mass (NASTRAN element type CONM2). The spatial location and the mass properties assigned to this lumped parameter are tuned to match the nominal APMODE mass distribution. The original fuselage vertical offset, reported in Table 3.5, is preserved. Along the longitudinal axis the lumped element is located at a distance of 22.40 inches from the center of the wing towards the nose (Figure 3.10). The inertias associated with the fuselage are reported in Table 3.12. The original weight is not altered by the updating procedure and the magnitude reported in Table 3.6 is maintained.

The final XV-15 APMODE mass properties, evaluated after the updating procedure, are listed in Tables 3.13 and 3.14. The computed percent errors are lower with respect to previous results (Tables 3.10, 3.11) and are considered tolerable. The center of mass location becomes acceptable and remains within the tiltrotor's center of gravity limitations, as highlighted in Figure 3.11. These results are considered satisfactory.

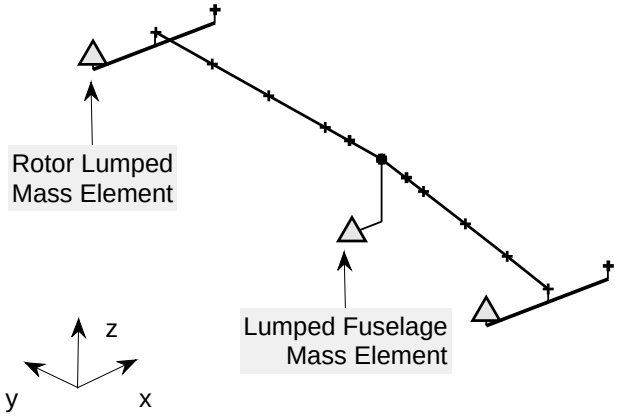

Figure 3.10: Updated FE Stick Model

	I_{xx}[blob · in^2]	I_{yy}[blob · in^2]	I_{zz}[blob · in^2]	I_{xz}[blob · in^2]
CONM2	5.930E+04	2.100E+05	3.041E+05	0.147E+05

Table 3.12: Lumped Fuselage Mass Inertias

	I_{xx} [blob · in^2]	I_{yy} [blob · in^2]
CAMRAD J/A	6.1138E+05	2.4417E+05
NASTRAN	5.729410E+05	2.429293E+05
err %	6.2877	0.5060
	I_{zz} [blob · in^2]	I_{xz} [blob · in^2]
CAMRAD J/A	8.0599E+05	1.2910E+04
NASTRAN	8.169145E+05	1.260217E+04
err %	1.3550	2.2827

Table 3.13: XV-15 APMODE mass properties

	x_G	z_G	units
CAMRAD J/A	296.880	72.828	in
NASTRAN	297.5611	73.3996	in

Table 3.14: XV-15 APMODE Center of Mass location

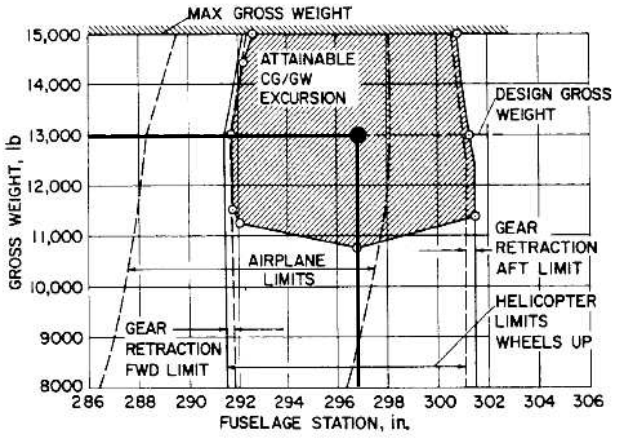

Figure 3.11: Center of Gravity Limitations Ref.[5]

Ref.[28] also provides the center of mass location in HEMODE. Figure 3.12 compares the station and water line coordinates of the tiltrotor's center of mass obtained in NASTRAN and CAMRAD for HEMODE and APMODE. Results overlap with good approximation.
The same figure also shows the coordinates of the center of mass with respect to the nacelle conversion angle (NAC), obtained in NASTRAN. Since the nacelles' weight equals about a third of the entire mass of the aircraft, the tiltrotor conversion manoeuvre causes the center of mass to move quite significantly along the water line.

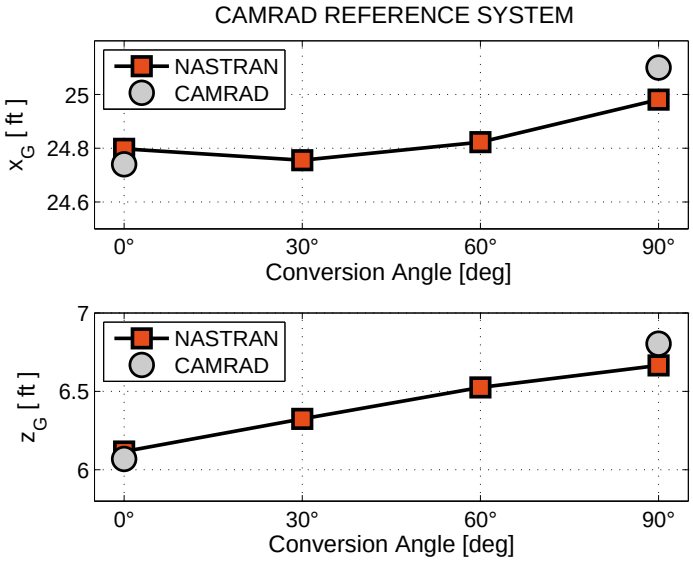

Figure 3.12: Center of Gravity coordinates with respect to nacelle conversion angle

3.4 XV-15 Model Update and Validation

In Section 3.3 the original FE stick model of Ref.[15] is structurally modified in order to match the XV-15 APMODE mass properties. In particular the fuselage rigid beam is replaced by a lumped parameter of assigned mass and inertia. Thanks to this procedure the error over the mass distribution of the aircraft is demonstrated to significantly decrease. However, it is necessary to re-evaluate the modal properties of the altered model to verify possible variations due to the applied modification.

Table 3.15 lists the natural frequencies associated with the structurally modified NASTRAN model of Figure 3.10. These are compared with the natural frequencies reported in Ref.[15]. It can be observed that the application of the necessary structural modifications mostly affect the AWT frequency, whose percent error reaches a value of 8.60%.

Mode Name	**SWB**	**AWB**	**SWC**	**AWT**	**SWT**	**AWC**
Acree [Hz] Ref.[15]	3.30	6.30	6.30	7.10	8.30	8.70
NASTRAN [Hz]	3.19	6.19	6.39	7.71	8.52	8.97
err $\%_{Hz}$	3.33	1.75	1.43	**8.60**	2.65	3.10

Table 3.15: Airframe Natural Frequencies

To reduce the AWT frequency error a further modification is applied to the model; the fourth mode is a coupled mode between torsion and chord and the AWC frequency lightly exceeds the predicted one, by a 3.10 %. It is subsequently decided to lower the magnitude of the wing chord bending stiffness EJ_z indicated in Table 3.2. Such reduction is considered tolerable since the in-plane bending stiffness does not correspond to a physically measured value. It is an equivalent structural property that allows the representation of the six lowest normal modes of the wing by means of a restricted set of parameters. As a result of a tuning process, a 10% lowering of the in-plane bending stiffness is considered sufficient to ensure a satisfactory reduction of the AWT frequency error.
The natural frequencies and the modal shapes associated with the updated model, characterised by a reliable mass distribution and by a reduced in-plane bending stiffness, are compared with the corresponding results of Ref.[15]. Table 3.16 shows that, through the lowering of EJ_z, the frequency error becomes more uniformly distributed among all the frequencies, maintaining acceptable low values. Also the modal shape correlation of Figure 3.14 is considered widely satisfactory.

In summary, the final updated model is characterised by a reliable mass distribution, as demonstrated by the results reported in Table 3.16 and Figure 3.14. These results are achieved replacing the rigid-fuselage-beam with a lumped fuselage mass element, whose characteristics are listed in Table 3.12. Finally, the lowering of the chord bending stiffness ensures a good correlation with the mode frequencies and modal shapes reported by Acree in Ref.[15]. The structural properties of the final updated model are resumed in **Appendix D.2**.

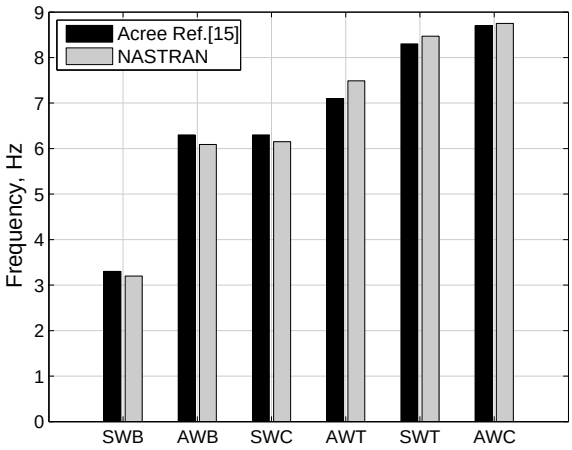

Figure 3.13: Airframe APMODE Natural frequencies after updating procedure

Mode Name	**SWB**	**AWB**	**SWC**
err $\%_{Hz}$	3.1303	3.2683	2.3175
Mode Name	**AWT**	**SWT**	**AWC**
err $\%_{Hz}$	5.6113	2.0157	0.5782

Table 3.16: APMODE frequency error after updating procedure

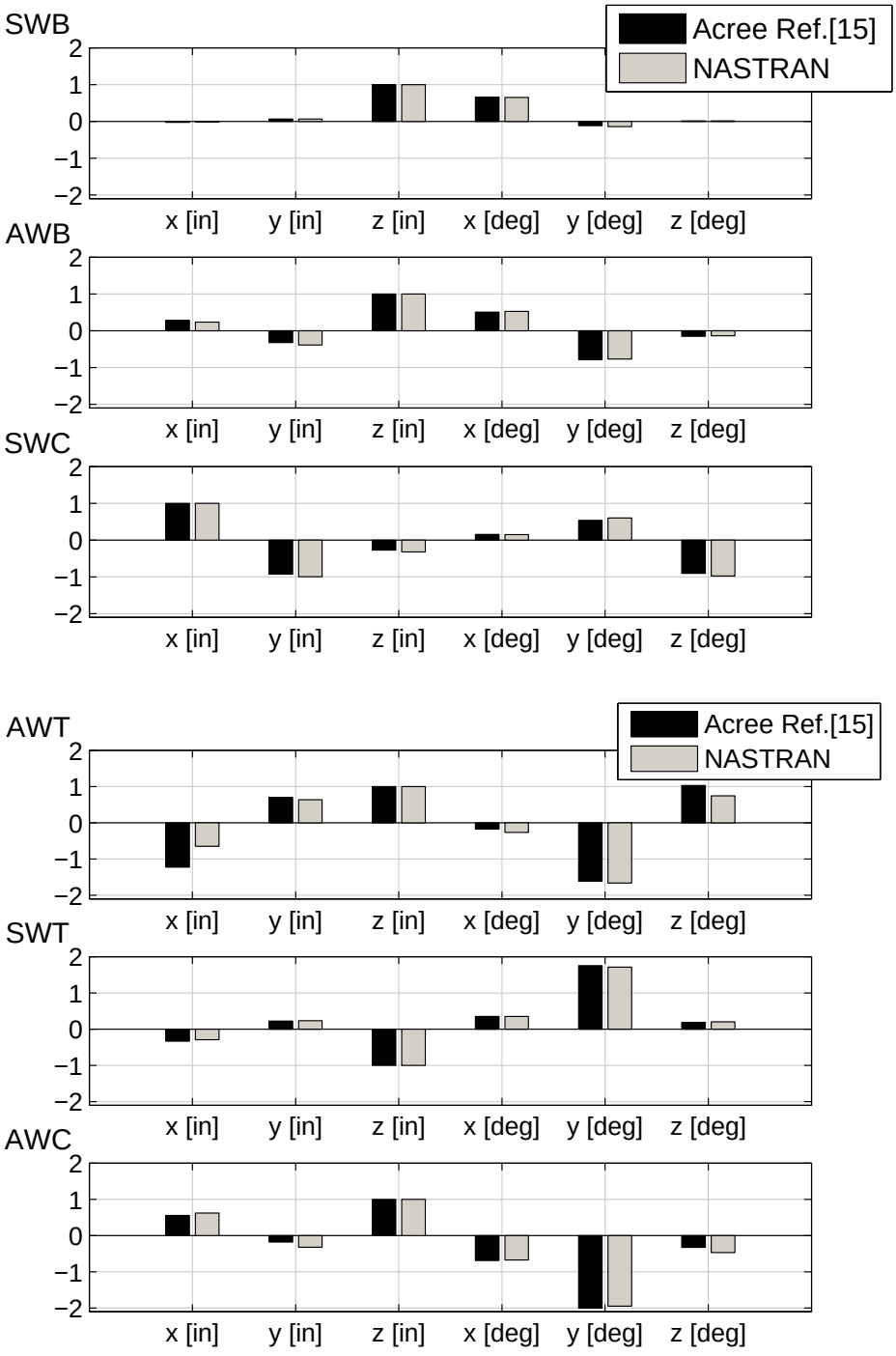

Figure 3.14: Right Hub Mode Shapes after updating procedure

3.5 Wing-Nacelle Compliance

3.5.1 Downstop Off

The natural frequencies of the structural airframe as a function of the pylon conversion angle are shown in Figure 3.15 of Ref.[5] (both for symmetric and asymmetric modes). The sudden frequency change at zero degrees is justified by the engagement of the pylon downstops. A downstop-on configuration, with respect to a downstop-off, is characterised by a more rigid wing-nacelle connection and it is adopted in APMODE forward flight, due to the high aerodynamic loads on the rotors.
In the XV-15 NASTRAN model of Figure 3.2 the wing tip and the nacelle are clamped. To represent the downstop-off local compliance between the two substructures it is decided to replace the rigid constraint with lumped angular springs about the nacelle's pitch and yaw axes.

With reference to Figure 3.15, it can be observed that, among the six lowest normal modes of the airframe, the wing torsion is the most affected by the engagement of pylon downstops. Hence, to represent the downstop-off configuration, it is introduced a lumped angular spring about the nacelle's pitch axis. The magnitude of the pitch spring stiffness K_{pitch} is tuned to match the downstop-off symmetric and asymmetric wing torsion mode frequencies.

In Figure 3.15, it is also shown that, near 10 Hz, the modal behaviour is mainly influenced by the symmetric and asymmetric pylon yaw modes (SPY, APY), that involve a yaw movement of the nacelles. The downstop-off SPY and APY mode frequencies are obtained introducing an angular spring of stiffness K_{yaw} about the nacelles' yaw axis.

In summary, the downstop-off configuration is modelled adjusting the magnitude of the nacelle's pitch and the yaw springs. The first is tuned to match the downstop-off torsional frequencies, while the second is tuned to match the downstop-off pylon yaw frequencies. The adopted procedure is exposed through the passages reported below.

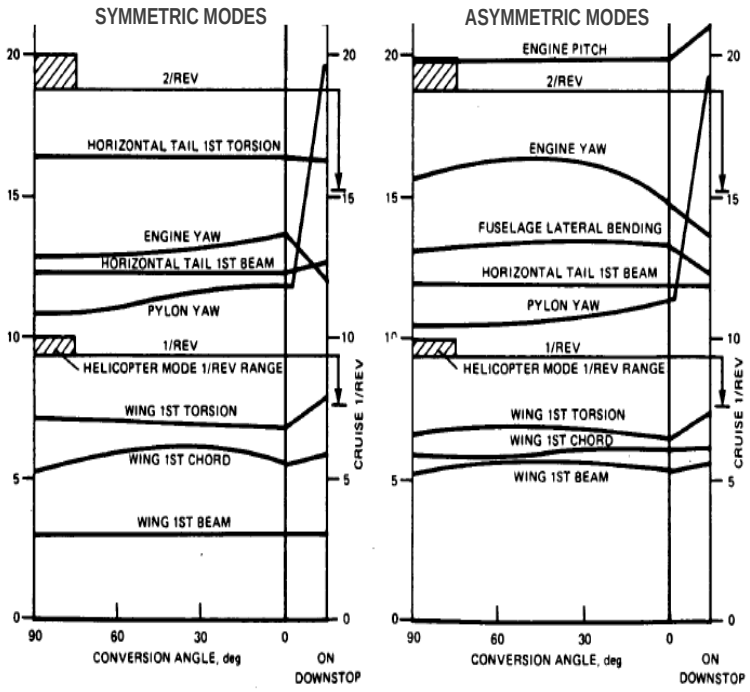

Figure 3.15: Airframe Natural Frequencies with respect to the NAC angle Ref.[5]

As already mentioned, the airframe natural frequencies validated in Section 3.4 (Figure 3.13) , are obtained assuming a clamped constraint between the nacelle and the wing tip. These results are considered representative of a downstop-on configuration. NASTRAN downstop-on torsional frequencies (listed in **Appendix C**) are reported below.

$$\mathrm{f}^{ON}_{sym\,tors.} = 8.46\,\mathrm{Hz} \tag{3.1}$$

$$\mathrm{f}^{ON}_{asym\,tors.} = 7.49\,\mathrm{Hz} \tag{3.2}$$

The percent reductions of the symmetric and asymmetric torsional frequencies after a shift from downstop-on to downstop-off are estimated from data of Ref.[5]. Such reductions, reported in Eqs.3.3 and 3.4, are applied to the corresponding NASTRAN downstop-on torsional frequencies (Eqs.3.1, 3.2) to estimate the downstop-off values.

$$\Delta_{sym\,tors.} = 12.62\% \tag{3.3}$$

$$\Delta_{asym\,tors.} = 10.56\% \tag{3.4}$$

The estimated torsional downstop-off frequencies are reported in Eqs. 3.5 and 3.6. They represent the target values to be obtained in NASTRAN through a tuning of the stiffness K_{pitch}, that is associated with a pitch spring located at the wing's tip.

$$\mathrm{f}^{OFF}_{sym\,tors.} = \mathrm{f}^{ON}_{sym\,tors.}(1 - \Delta_{sym\,tors.}) = 7.39\,\mathrm{Hz} \tag{3.5}$$

$$\mathrm{f}^{OFF}_{asym\,tors.} = \mathrm{f}^{ON}_{asym\,tors.}(1 - \Delta_{asym\,tors.}) = 6.70\,\mathrm{Hz} \tag{3.6}$$

The value assigned to K_{pitch} and the associated NASTRAN torsional frequencies are listed in Table 3.17. The frequency error, evaluated with respect to the predicted values of Eqs. 3.5 and 3.6, is lower than 5% and it is considered satisfactory.

Mode Name	K_{pitch} lbf· in/rad	$f_{estimated}$ Hz	NASTRAN Hz	err% -
SWT	6.00E+07	7.39	7.51	1.62
AWT	6.00E+07	6.70	6.99	4.33

Table 3.17: Torsional Frequencies Downstop-off

Similarly, the angular spring K_{yaw}, associated with the nacelles' yaw, is tuned to match the pylon yaw frequencies reported in Figure 3.15. The final value assigned to K_{yaw} and the associated NASTRAN frequencies are listed in Table 3.18. Again, the low percent errors are considered satisfactory. **Appendix D.3** reports NASTRAN visualisations of the SPY and APY.
It should be specified that the pylon yaw modes, located above 11 Hz, have a negligible impact over the PAOs study, whose characteristic bandwidth is between 2-8 Hz (Ref.[7]). However, for completeness, they are incorporated into the model. The pylon yaw modes may be relevant for other studies characterised by a higher frequency range, e.g. a whirl flutter analysis.

Mode Name	K_{yaw} lbf· in/rad	$f_{estimated}$ Hz	NASTRAN Hz	err% -
SPY	4.00E+07	11.70	12.23	4.53
APY	4.00E+07	11.92	12.36	3.69

Table 3.18: Pylon Yaw Frequencies Downstop-off

3.5.2 Airframe Natural Frequencies's Validation

In Ref.[5] (Figure 3.15) the airframe natural frequencies of a detailed XV-15 FE model are calculated as a function of the NAC angle. The trends, associated with the six lowest modes, are graphically acquired and reported in Figure 3.16. The gradual natural frequency variation with the nacelle angle is due to the shift in location of the pylon mass as the nacelles are converted. Since the nacelles comprises approximately 30% of the tiltrotor empty weight, the conversion manoeuvre has a significant impact over the tiltrotor's mass distribution, and, as a consequence, over the airframe natural frequencies.

Figure 3.16 compares the predicted trends of Ref.[5] with the corresponding NASTRAN results. The adopted stiffnesses of the angular pitch and yaw springs are reported in Table 3.19. The NAC angles between 90 and 0 dowstop-off degrees are assigned the values of K_{pitch} and K_{yaw} estimated in Section 3.5.1 to model the downstop-off. The downstop-on is instead approximated by a clamped constraint between the wing and the nacelle, and for this reason the springs' stiffnesses assume infinite values. This hypothesis will be removed in Section 3.5.4.
A good correlation between the symmetric trends can be appreciated. Also the AWB and AWT frequencies match the predicted values with good approximation. A critical behaviour is instead exhibited by the AWC. The downstop-on AWC frequency of NASTRAN, validated by Ref.[15], is located at a higher value with respect to the one proposed in Ref.[5]. As a matter of fact References [15] and [5] report two non-consistent downstop-on AWC frequencies. As a consequence, a matching between the AWC trends derived from NASTRAN and from Ref.[5] is not ensured.

In conclusion, the exposed results demonstrate that, through the introduction of properly tuned pitch and yaw angular stiffnesses, the simple FE stick model of Figure 3.2 can still be representative of many XV-15 configurations, corresponding to different pylon conversion angles. In fact, despite the AWC incongruence, the trends of the airframe natural frequencies, calculated with respect to the NAC angle, are in good agreement with reference data of [5].

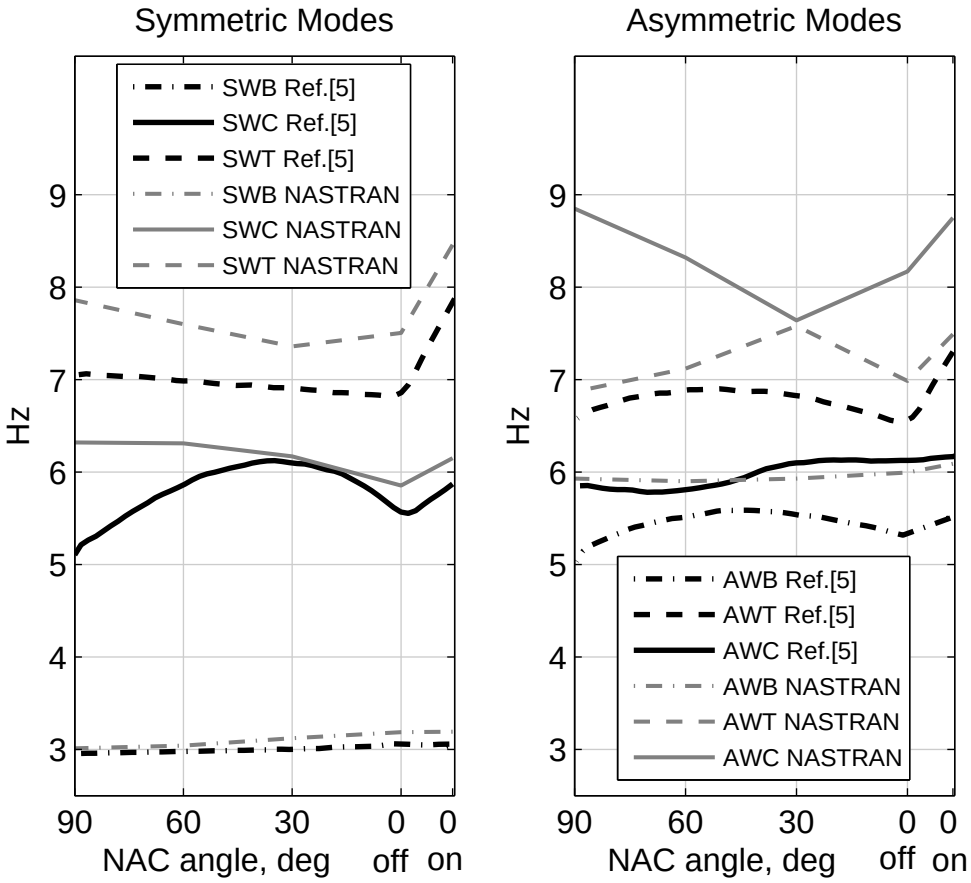

Figure 3.16: Airframe Natural Frequencies with respect to the NAC angle for NASTRAN validation

NAC deg	downstop	$\mathbf{K}_{pitch}$ lbf· in/rad	$\mathbf{K}_{yaw}$ lbf· in/rad
0	on	Inf.	Inf.
0	off	6.00E+07	4.00E+07
30	off	6.00E+07	4.00E+07
60	off	6.00E+07	4.00E+07
90	off	6.00E+07	4.00E+07

Table 3.19: Pitch and Yaw Springs Values

3.5.3 Nacelle-Actuator Kinematics

As discussed in Section 3.5.1, the compliance between the nacelle and the wing tip is modelled introducing two angular springs about the nacelle's yaw and pitch axes. Such springs are assumed to maintain a constant stiffness for all conversion angles, with the only exclusion of the downstop-on configuration (Table 3.19). In this Section it is intended to replace the constant downstop-off angular pitch spring with a nacelle-actuator scheme.

The physical nacelle actuator system, represented in Figure 3.17(a), is described by means of a simplified model, depicted in Figure 3.17(b), whose kinematics is defined by the angles α and β. The β angle represents a measure of the inclination of the nacelle. According to Figure 3.17, point C is the spindle point and it belongs to the airframe wing tip; points A and B'' represent, respectively, the airframe and nacelle actuator points and they are assumed to be connected by an elastic bar whose stiffness K_{AB} is characterised by the Young Modulus E, the section area A and the length

	x [in]	**y [in]**	**z [in]**
A	222.919	185.412	198.925
B''	231.576	185.922	204.006
C	251.469	189.026	198.900

Table 3.20: APMODE nacelle-actuator kinematics' coordinates

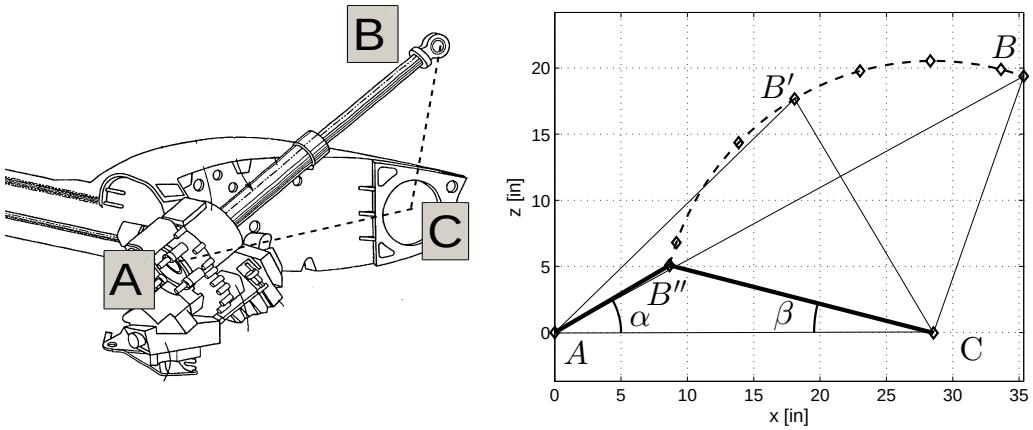

(a) Actuator Physical System Ref,[37] (b) Actuator Mathematical Kinetic Model

Figure 3.17: Nacelle Actuator

L_{AB}, as reported in Equation 3.7.

$$K_{AB} = \frac{EA}{L_{AB}} \quad \Big[Lbf/in\Big] \tag{3.7}$$

A, B'' and C APMODE coordinates, graphically estimated from nacelle-actuator sketches of Ref.[5], are reported in Table 3.20. The APMODE β_0, α_0 and ϕ_0 angles can be estimated using the following kinematic relations:

$$\begin{cases} \beta_0 = acos\Big(\frac{AC^2+BC^2-AB^2}{2\cdot AC\cdot BC}\Big)\Big|_{\text{APMODE}} \\ \alpha_0 = asin\Big(\frac{BC}{AB}\cdot sin\beta_0\Big)\Big|_{\text{APMODE}} \\ \phi_0 = \pi/2 - \alpha_0 + \beta_0 \end{cases} \tag{3.8}$$

For pylon-converted configurations the angles α and ϕ can be evaluated as a function of the conversion angle β :

$$\begin{cases} \beta = \beta_0 + \Delta\beta \\ \alpha = asin\Big(\frac{BC}{AB(\beta)}sin\beta\Big) \\ \phi = \pi/2 - \alpha + \beta \end{cases} \tag{3.9}$$

The actuator, modelled as a rod of axial stiffness EA, produces an elastic force F_{el}. Under the hypothesis of a plane kinematics, the moment M_C, generated by the actuator's elastic force with respect to the spindle point C, can be obtained through Eqs. 3.10 - 3.12.

$$L = L_{AB} + L_{BC}\cdot\Delta\beta cos\phi \quad \Big[in\Big] \tag{3.10}$$

$$F_{el} = K_{AB}\cdot(L - L_{AB}) \quad \Big[Lbf\Big] \tag{3.11}$$

$$M_C = F_{el}\cdot cos\phi\cdot L_{BC} \quad \Big[Lbf\cdot in\Big] \tag{3.12}$$

Substituting expressions 3.7 and 3.11 into Equation 3.12, the Moment M_C can be expressed as:

$$M_C = \frac{EA}{L_{AB}}\cdot(L_{BC}\cdot cos\phi)^2\Delta\beta \quad \Big[Lbf\cdot in\Big] \tag{3.13}$$

Consequently the equivalent actuator stiffness K_{act} can be estimated as:

$$K_{act} = \frac{M_c}{\Delta\beta} = \frac{EA}{L_{AB}}\cdot(L_{BC}\cdot cos\phi)^2 = K_{act}(\beta) \quad \Big[Lbf\cdot in/rad\Big] \tag{3.14}$$

Where EA represents the AB bar's stiffness, L_{AB} the length of the actuator and L_{BC} a constant distance. It can be noticed that this stiffness depends

on the actuator's length $L_{AB}(\beta)$ and on the angle $\phi(\beta)$, both functions of the nacelle conversion angle β. As a result, the downstop-off pitch spring can be replaced by an actuator, that is characterised by a variable stiffness K_{act} scheduled with respect to the NAC angle.
The axial stiffness EA, needed to schedule K_{act} as a function of conversion angle, can be estimated inverting Eq.3.14 and evaluating the right hand side in APMODE downstop-off, as shown in Eq.3.15.

$$EA = \left. \frac{L_{AB} \cdot K_{act}}{(L_{BC} \cdot cos\phi_0)^2} \right|_{\text{APMODE, downstop OFF}} \tag{3.15}$$

Figures 3.18 and 3.19 show the trend of L_{AB}, α and ϕ with respect to NAC angle β. Figure 3.18 confirms the legitimacy of the plane kinematics assumption.
The trend of the actuator's stiffness K_{act} as a function of β is represented in Figure 3.20. The corresponding numerical values are listed in Table 3.21. The stiffness magnitude rapidly decreases for NAC angles greater than 30 degrees, showing a quite large variation of K_{act}.
No experimental data is available to validate the obtained numerical results. It is however performed a comparison between the outcomes that can be obtained in NASTRAN with and without the introduction of the nacelle actuator. The found differences are critically evaluated in the following.

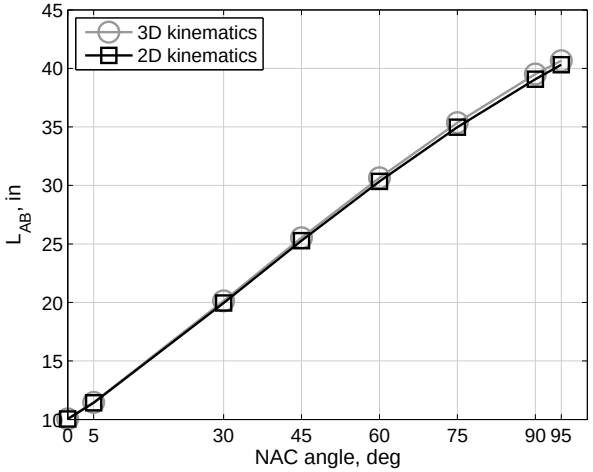

Figure 3.18: Actuator Kinematics - L_{AB} length

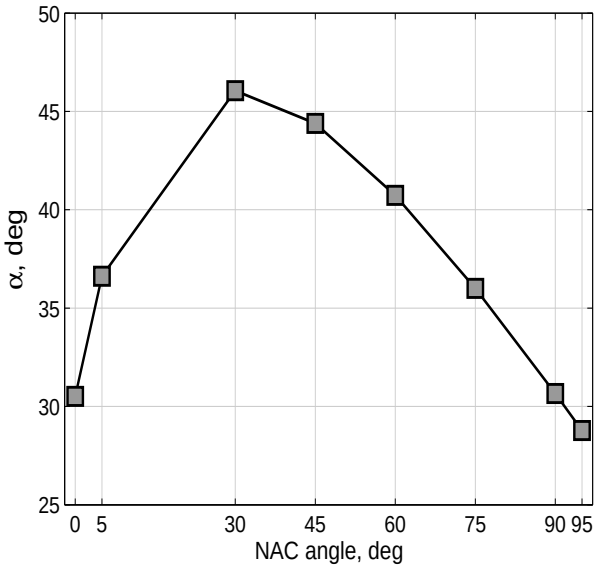

(a) α angle

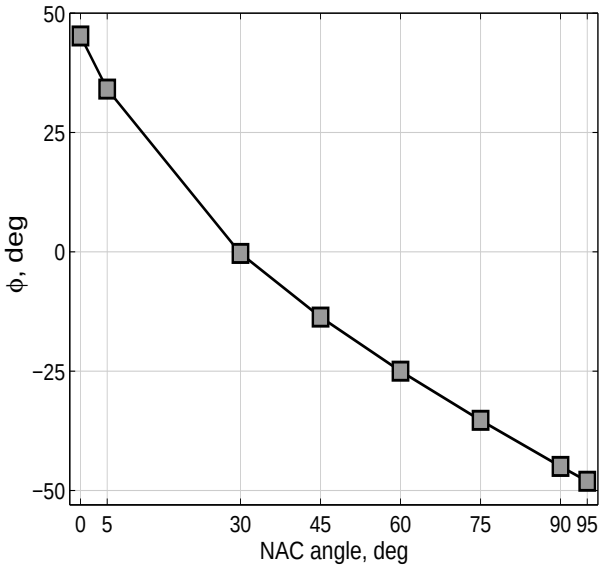

(b) ϕ angle

Figure 3.19: Actuator Kinematics - α and ϕ angles

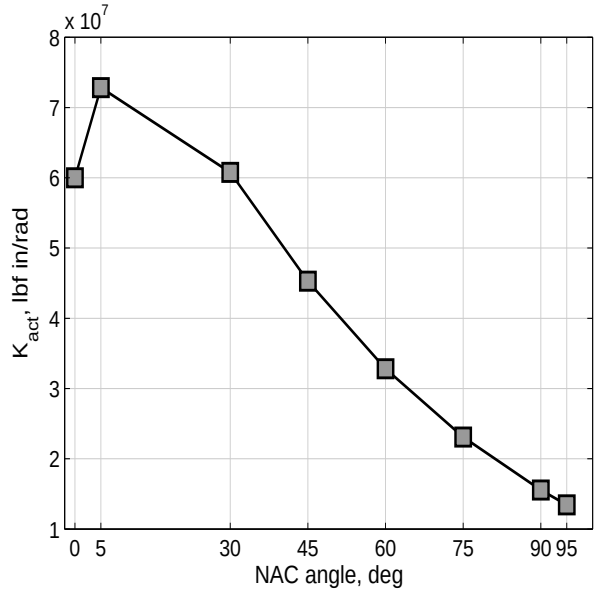

Figure 3.20: Actuator Kinematics - Stiffness K_{act}

NAC deg	$K_{actuator}\ \frac{lbf \cdot in}{rad}$
0	6.0000000e+07
5	7.2843325e+07
30	6.0770500e+07
45	4.5291923e+07
60	3.2821527e+07
75	2.3095893e+07
90	1.5542860e+07
95	1.3430391e+07

Table 3.21: Stiffness Scheduling

Figure 3.21 compares the airframe natural frequencies without and with the nacelle actuator. In the first case the gradual natural frequency variation with nacelle angle is due to the shift in location of the pylon mass. In the second case the frequency variation is also due to the application of a varying parameter represented by the actuator's equivalent stiffness (Table 3.21). The results overlap with good approximation from 0 to 60 degrees, both for symmetric and asymmetric frequencies. Beyond 60 degrees of NAC angle it can be appreciated a discrepancy between the two models. The application of the nacelle-actuator scheme mostly affects the torsional frequencies; this is due to the low value assumed by the equivalent actuator's stiffness in HEMODE (Table 3.21), that impacts reducing the torsional frequencies. The SWB and AWC are not influenced by the introduction of the actuator and result almost unaltered.

In summary, the nacelle-actuator kinematics is proposed to model a more physical wing-nacelle local compliance. The airframe natural frequencies, obtained after its introduction, are compared with the validated results of Section 3.5.2. The nacelle actuator kinematics influence the higher conversion angles and the largest impact is over the torsional frequencies.

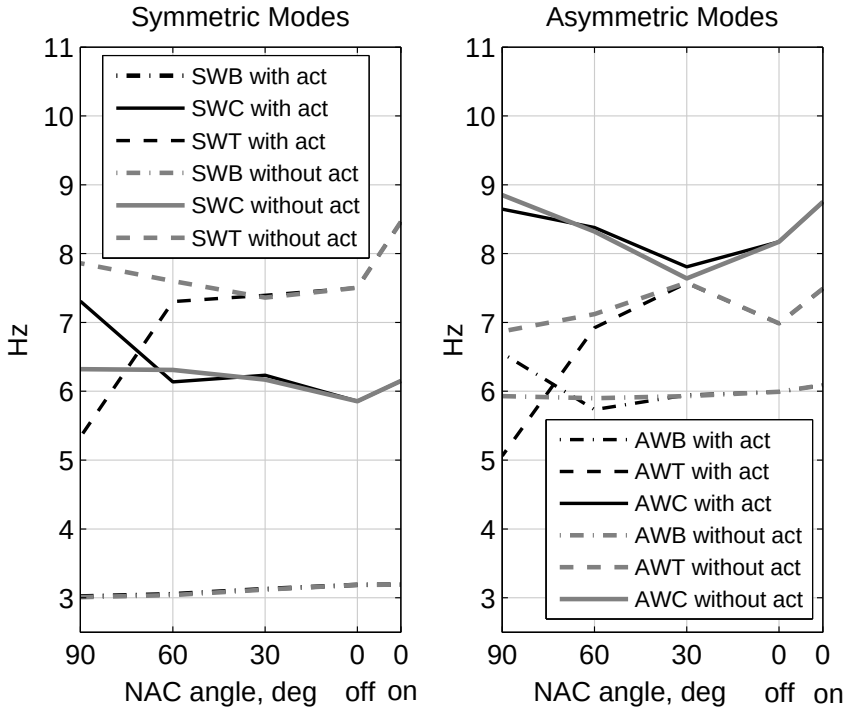

Figure 3.21: Airframe Natural Frequencies with respect to the NAC angle, with/out nacelle actuator

3.5.4 Downstop On

In Section 3.2 the downstop-on configuration is validated adopting a rigid constraint between the wing tip and the nacelle. It is now decided to replace the clamped connection with a more physical local compliance to represent the engagement of the pylon downstop.
As shown in Equation 3.17, the downstop-on pitch spring stiffness is estimated scaling the corresponding downstop-off value by a multiplicative factor N, which is tuned to match the APMODE downstop-on natural frequencies of Ref.[15]. A magnitude of N=2.5 is demonstrated to recover with good approximation the modal frequencies and shapes associated with the initial clamped constraint.

$$K_{pitch}^{OFF} = 6.00\text{E+}07 \ \left[Lbf \cdot in/rad\right] \tag{3.16}$$

$$K_{pitch}^{ON} = N \cdot K_{pitch}^{OFF} = 2.5 \cdot K_{pitch}^{OFF} = 1.5\text{E+}08 \ \left[Lbf \cdot in/rad\right] \tag{3.17}$$

In NASTRAN it is run an eigenvalue analysis to check the airframe natural frequencies and the normal modes obtained adopting the downstop-on pitch spring value of Equation 3.17. The goodness of the results is, once again, quantified estimating the error with respect to the airframe natural frequencies of Ref.[15]. Table 3.22 shows that the results overlap with good approximation and a satisfactory match is also highlighted by the mode shapes representation of Figure 3.22. As a result, the downstop-on configuration recovers the characteristics of the clamped constraint.

Mode Name	**SWB**	**AWB**	**SWC**	**AWT**	**SWT**	**AWC**
Acree - Ref.[15] [Hz]	3.3	6.3	6.3	7.1	8.3	8.7
downstop ON [Hz]	3.1930	6.0222	6.1019	7.3039	8.0501	8.5099
err $[\%]_{Hz}$	3.2435	4.4095	3.1447	2.8719	3.0114	2.1856

Table 3.22: Downstop-on Natural Frequencies

The downstop-on yaw spring value K_{yaw}^{ON} is tuned to obtain the downstop-on pylon yaw frequencies of Ref.[5]. The results are listed in Table 3.23 and are considered satisfactory .

	K_{yaw} lbf· in/rad	$f_{estimated}$ Hz	NASTRAN Hz	err % -
SPY	1.326E+08	19.07	18.53	2.83
APY	1.326E+08	19.51	18.87	3.28

Table 3.23: Yaw Spring, Downstop-on

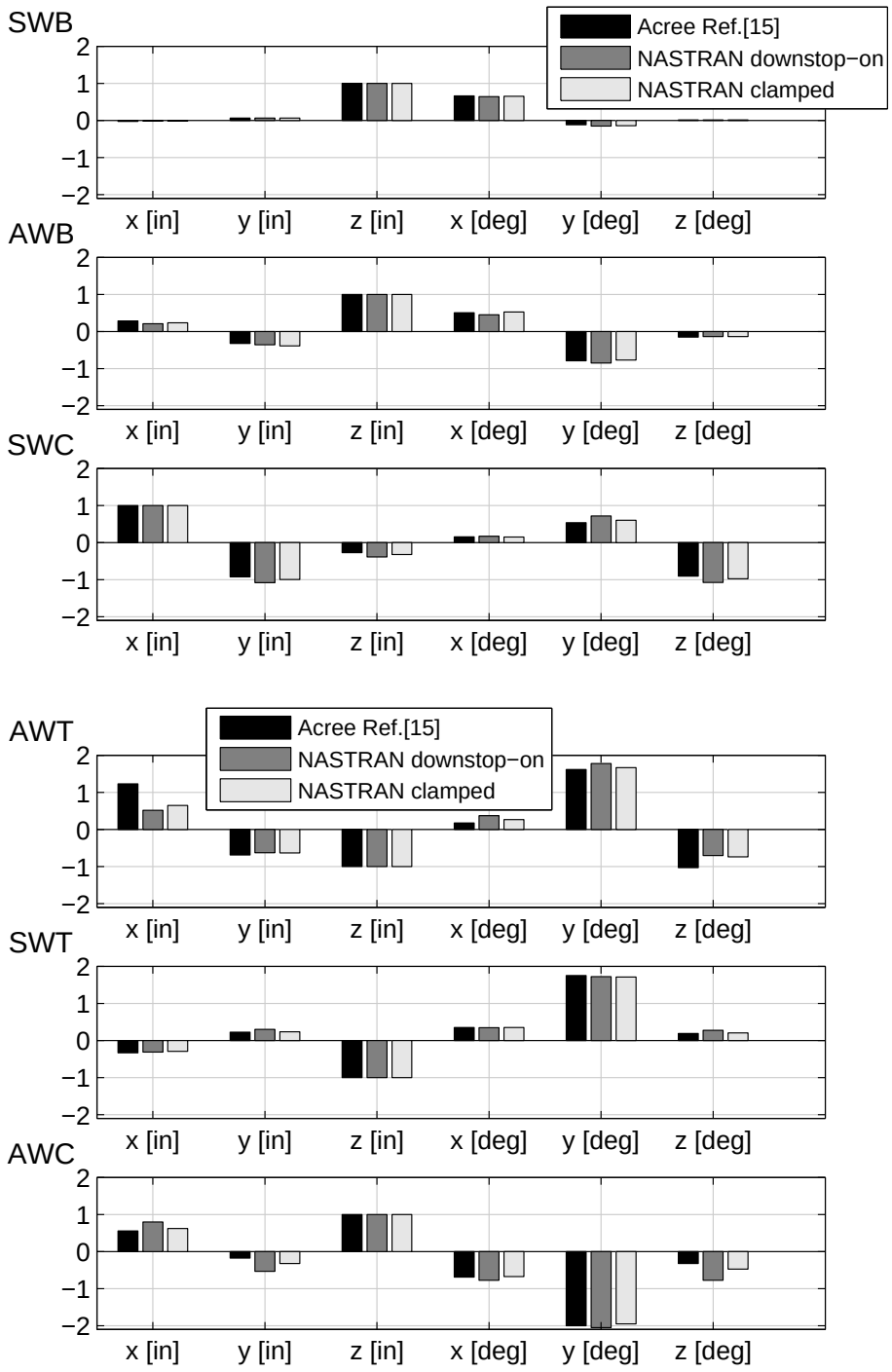

Figure 3.22: Right Hub Mode Shapes comparison

Chapter 4

Instability Mechanism on the Lateral Axis

4.1 Lateral PVS Dynamics

This chapter is dedicated to the aeroelastic RPC instabilities involving the tiltrotor's lateral dynamics. In particular it is intended to examine the relationship between the pilot's lateral cyclic stick control input and the subsequent vehicle motion in the lateral direction. The analyses are run considering high speed airplane mode (APMODE) flight.
In the XV-15, a lateral motion of the stick in APMODE generates an asymmetric deflection of the flaperons. For example, a movement of the stick to the right causes the right flaperon to move up and the left flaperon to move down, producing a roll motion to the right (Figure 4.1).
The vehicle lateral SISO dynamics is schematised in Figure 4.2. The invol-

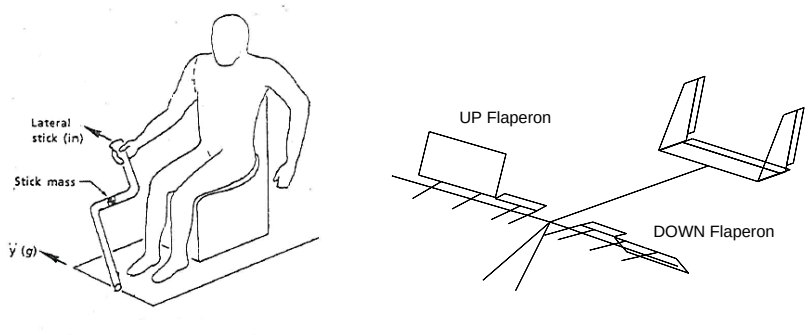

(a) Lateral Stick Motion (b) Flaperons Asym Deflection

Figure 4.1: Lateral Stick Motion

untary/passive pilot lateral-axis transfer function $H(s)^{PP}$ is put in feedback with the tiltrotor aeromechanics $H_{XV15}(s)$. Due to a lateral acceleration a_Y the pilot generates the output δ_Y^{PP}, which represents the involuntary lateral deflection of the stick. δ_Y^{PP} is later amplified by $G_f(s)$, which is defined in Equation 4.1. It is the product of a constant gear ratio G_{f0}, that converts the lateral displacement of the stick into degrees of flaperons' deflection θ_f, and an exponential function, which introduces a time delay τ over the stick control command.

$$G_f(s) = G_{f_0} \cdot e^{-\tau \cdot s} \tag{4.1}$$

The asymmetric deflection of the flaperons θ_f excites the tiltrotor's lateral dynamics, producing a lateral acceleration a_Y, that closes the loop. The influence of a voluntary/active pilot's input δ_Y^{AP} is not contemplated in the analyses.

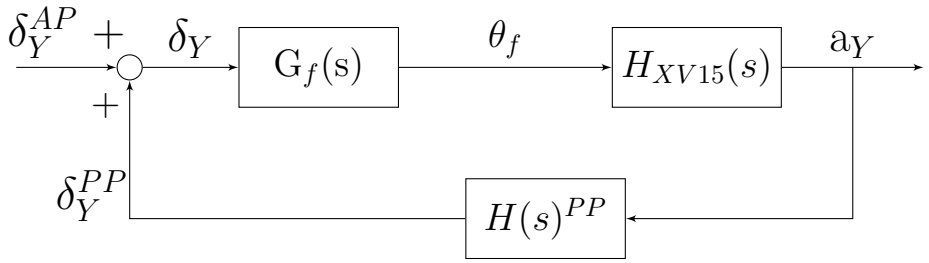

Figure 4.2: PVS Block Scheme - XV-15 Lateral Dynamics

4.1.1 Lateral Pilot/Control Device Dynamics

The pilot/control device lateral-axis transfer function is obtained from Reference [34]. This work illustrates the results of a test campaign focused on the study of lateral RPCs during which the BDFTs of three trained Test Pilots are identified.

The pilot's lateral dynamics is described by the transfer function reported in Equation 4.2. δ_Y^{PP} represents the involuntary pilot lateral stick displacement and a_Y represents the lateral acceleration measured at the pilot's seat. The structural properties identified for the three Test Pilots are reported in Table 4.1. The complex-conjugate biodynamic poles are well damped, with $\xi > 20\%$. Test Pilot 3 has the highest damping ratio: close to 40%. The natural frequencies ω_n range between 2 and 3 Hz and Pilot 2 shows the highest frequency of 2.95 Hz. The static gain μ_p of the transfer function of Pilot 1 is higher than that of the other pilots. Moreover, the low natural frequency of the biodynamic pole of this pilot causes a phase reduction at frequencies

lower than the other pilots' transfer functions. The different results obtained for Pilot 1, compared with the other pilots, are probably related to his anthropometric characteristics: Pilot 1 belongs to the 99th percentile in terms of height and weight, showing somewhat different biomechanical properties from those of an average individual.
The Bode plots of the individual pilot's transfer functions are shown in Figure 4.3.

$$\frac{\delta_Y^{PP}}{a_Y} = -\mu \frac{sT_z + 1}{sT_p + 1} \cdot \frac{1}{\left(\frac{s}{\omega_n}\right)^2 + 2\xi\left(\frac{s}{\omega_n}\right) + 1} \tag{4.2}$$

	units	Pilot 1	Pilot 2	Pilot 3
μ	%/g	216.26	88.67	83.88
T_z	sec	0.02	0.05	0.03
T_p	sec	0.51	0.49	0.26
ξ	%	26.87	23.11	39.66
ω_n	rad/s	13.59	18.53	14.81

Table 4.1: Pilot/Lateral stick dynamic properties

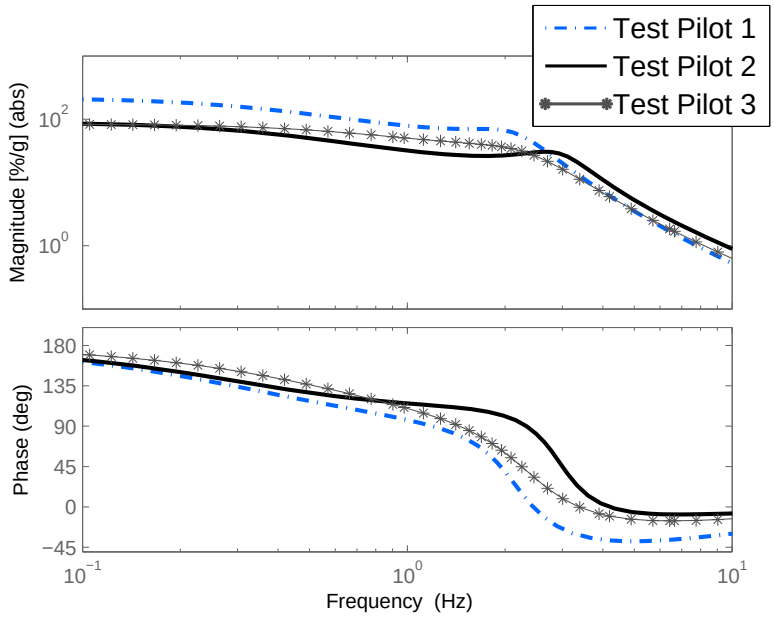

Figure 4.3: Test Pilots' BDFTs, from a_Y [g] to δ_Y^{PP} [%], Ref.[34]

As depicted in Figure 4.4, the lateral stick position δ_Y^{PP}, expressed as percentage of the maximum stick travel, can be converted into equivalent degrees of flaperon's deflection θ_f through the gear ratios G_1 and G_2. The numerical value of G_1, reported in Equation 4.3, is derived from Ref.[5] and G_2, reported in Equation 4.4, is obtained from Ref.[26]. The constant gear ratio G_{f_0}, reported in Equation 4.1, can be consequently expressed by the product of G_1 and G_2 (Eq. 4.5).

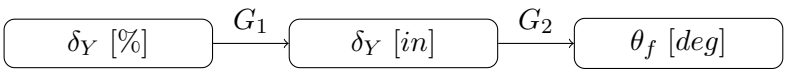

Figure 4.4: Lateral Gear Ratios from δ_y^{PP}[%] to θ_f[deg]

$$G_1 = 0.048 \quad [in/\%] \tag{4.3}$$

$$G_2 = 3.93 \quad [deg/in] \tag{4.4}$$

$$G_{f_0} = G_1 \cdot G_2 \quad [deg/\%] \tag{4.5}$$

Before proceeding, a further aspect should be specified; the shake tests performed during the experimental campaign of Ref.[34] required the pilot to keep the stick centred at null-command position. As a result, the pilots' transfer functions present an integral action in the low frequency range below 1 Hz, characterised by the low-frequency pole $-1/T_p$. This contribution can be attributed to the voluntary action the pilot exerts while trying to keep the control inceptor about the nominal position, thus acting as a regulator. A high pass filter is subsequently implemented to vanish the effect of the involuntary response in the bandwidth of the voluntary one. In agreement with Ref.[34], the cut off frequency is located at 3.10 rad/s, which is assumed to separate the active and passive pilots' responses. The adopted filter is a second order Butterworth filter, whose analytical expression is recalled below.

$$F_B = \frac{s^2}{s^2 + 2\xi\sqrt{2}/2 \cdot \omega_c \cdot s + \omega_c^2} \tag{4.6}$$

4.1.2 Tiltrotor Lateral Dynamics

In tiltrotors PAOs are commonly triggered by a resonance between the biodynamic pole of the pilot and an elastic mode of the airframe. As a matter of fact, in the lateral PAO reported for the V-22 (Ref.[11]), the pilot/control device, characterised by a biodynamic pole between 2-3 Hz (Figure 4.3), inadvertently destabilised the AWC mode, located at 3.25 Hz. In the XV-15 case, the AWC mode frequency is located near 8 Hz (Section 3.2). Due to the resulting frequency separation between the pilot's BDFT (2-3 Hz) and the tiltrotor's AWC (8 Hz), the possibility for a RPC to occur is unlikely. However, it is recalled that the XV-15 structural airframe, represented by the finite element stick model of Chapter 2.1, undergoes the strong hypothesis of a rigid fuselage. This aspect can potentially alter the frequency location of the AWC mode, that involves a consistent participation of the fuselage and tail's motion. With a flexible fuselage, the AWC frequency is expected to decrease. In support of this aspect, many literature sources demonstrate that the AWC mode frequency usually lays within a bandwidth between 3-4 Hz. As an instance, the V-22 AWC frequency is 3.25 Hz at 250 knots (Ref.[11]) and the AW609 AWC mode frequency is located at 3.76 Hz in vacuum (Ref.[38]). As a result it is decided to artificially modify the XV-15 AWC frequency location, moving it to a more realistic value. This operation is accomplished reducing the wing in plane bending stiffness, which is decreased by a 60%. The final AWC frequency equals a value of 3.28 Hz, close to the 3.25 Hz reported for the V-22. The tiltrotor's transfer function of the lateral acceleration response a_Y, measured at the pilot's seat, to the asymmetric flaperons' deflection θ_f is reported in Figure 4.5. The AWC mode frequency is highlighted near 3 Hz.

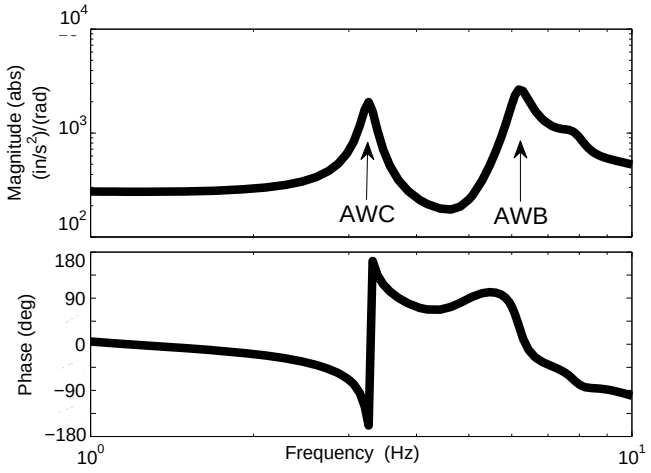

Figure 4.5: XV-15 transfer function from θ_f $[rad]$ to a_Y $[in/s^2]$

4.2 Pilot-in-the-Loop Results

4.2.1 PAO Analysis

Nyquist stability criterion is applied to the loop transfer function (LTF) of the lateral PVS of Figure 4.2, according to the procedure exposed in Section 2.5.2. The analyses are performed considering the most critical condition, represented by high speed APMODE flight. Specifically, the maximum APMODE airspeed (280 knots) is taken into account. The influence of possible time delays is initially neglected and flight height is maintained at Sea Level. Figure 4.6 compares the results obtained considering the feedback of the three Test Pilots of Section 4.1.1. High stability margins are highlighted for all the pilots. The numerical values of the gain margins and the associated frequencies are reported in Table 4.2. It can be observed that Test Pilot 2 exhibits a relatively larger response; this is due to the fact that the complex-conjugate biodynamic poles of this pilot are characterised by a natural frequency (2.95 Hz) that is closer, with respect to the other Test Pilots, to the AWC tiltrotor mode frequency (near 3 Hz). The coupling between the pilot's biomechanics and the in-plane bending mode of the wing is confirmed by the AWC mode shape visualisation reported in **Appendix E.1**. The lateral accelerations, induced by the AWC, excite the biodynamics of the lateral pilot, that acts on the lateral stick and induces an asymmetric deflection of the flaperons.

To further investigate the occurence of a lateral RPC, it is decided to evaluate the stability margins associated with a potential *High Gain Pilot*, which

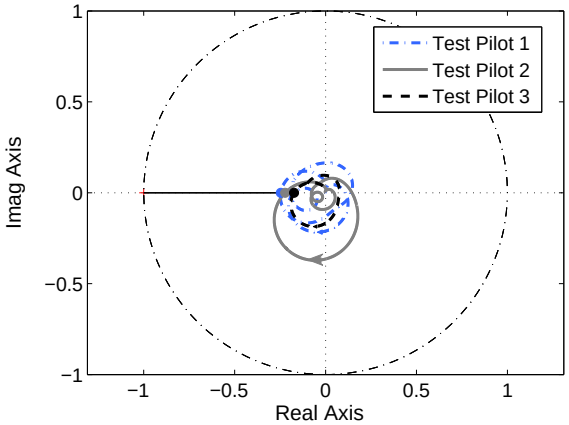

Figure 4.6: LTF Nyquist Diagram, nominal configuration (τ = 0 ms)

	$\mathbf{G_m}$ [dB]
Pilot 1	12.16
Pilot 2	13.07
Pilot 3	15.23
	$\mathbf{f(G_m)}$ [Hz]
Pilot 1	3.27
Pilot 2	3.36
Pilot 3	3.31

Table 4.2: Nominal Stability Margins

is artificially built through a combination of the structural characteristics of the three nominal Test Pilots. Specifically, this pilot retains all the characteristics of Pilot 2, out of the static gain, derived from Pilot 1. The Bode diagram of the *High Gain Pilot*'s BDFT is compared with the nominal ones in **Appendix E.2**. The LTF, obtained with *High Gain Pilot* feedback, is represented in Figure 4.7. It can be observed that, despite the relatively high gain margin, the lobe of the Nyquist diagram strongly enlarges with respect to the nominal cases of Figure 4.6.
The possibility of a PAO occurrence is further examined including a time delay on the lateral device control. Time delays, justified by the presence of fly-by-wire systems, digital acquisitions, filters and general signal processing (Ref.[34]), are introduced multiplying the constant gear ratio G_{f_0} by an exponential function (Eq.4.1). Figure 4.8 shows the effect of a delay over the PVS dynamics; the black solid line refers to the nominal LTF associated with the *High Gain Pilot*, while the grey lines represent the results obtained after the application of a time delay of increasing magnitude (10, 20, 50 ms). The nominal Nyquist diagram tends to rotate clockwise, reducing the gain margin. The lowest gain margin is obtained for a time delay of 50 ms.

The root locus of Figure 4.9 resumes the main results obtained in this Section. The squared markers represent the poles associated with the tiltrotor's open loop dynamics (i.e. without the pilot), whereas the circular markers are obtained after the Pilot-in-the-Loop stability analysis, performed considering the *High Gain Pilot*'s feedback. The introduction of the pilot decreases the stability of the AWC pole and, for increasing time delay τ, the AWC pole tends to shift towards the right half of the complex plane, thus becoming less stable. These results confirm that the AWC can be affected by the pilot's feedback. It should be specified that the XV-15 is not known to be prone to PAO phenomena associated with the lateral axis. Coherently, the exposed results demonstrate that the eventuality of a XV-15 lateral PAO is low and considerable losses of stability margins are contemplated only when the pilot's BDFT is characterised by the envelope of the most unfavourable structural properties of the Test Pilots and possible time delays are introduced.

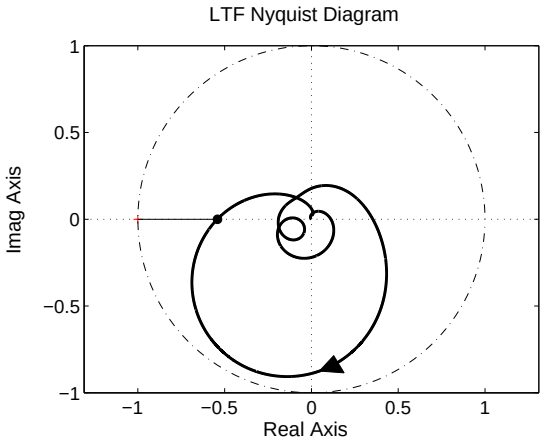

$\mathbf{G}_m$ [dB]	$\mathbf{f}(\mathbf{G}_m)$ [Hz]
5.33	3.36

Table 4.3: High Gain Pilot Stability Margins

Figure 4.7: LTF Nyquist Diagram, High Gain Pilot

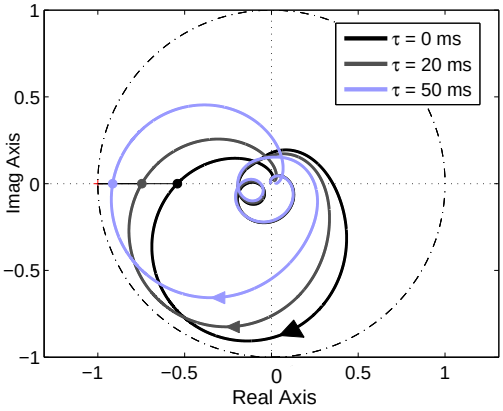

τ [ms]	$\mathbf{G_m}$ [dB]	$\mathbf{f}(\mathbf{G}_m)$ [Hz]
0	5.33	3.36
20	2.54	3.31
50	0.78	3.27

Table 4.4: High Gain Pilot and time delay, Stability Margins

Figure 4.8: LTF Nyquist Diagram, High Gain Pilot and time delay τ

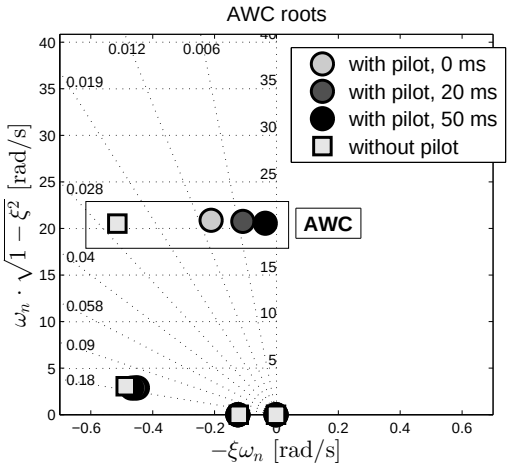

Figure 4.9: Root Locus, High Gain Pilot and time delay ($\tau \div 0$, 20, 50 ms)

4.2.2 PAO Detection

In Section 4.2.1 Pilot-in-the-Loop stability analyses are performed by introducing the pilot lateral-axis transfer function in feedback loop with the tiltrotor's aeromechanics. As a result, the pilot's lateral dynamics couples with the lateral oscillations of the AWC mode, located at 3.28 Hz in vacuum (Figure 4.9). A side acceleration induces an involuntary lateral stick motion that causes an asymmetric deflection of the flaperons (mode shape visualisation in **Appendix E.1**).

Many hypotheses have been formulated in the attempt to explain the source of excitation of the AWC due to an involuntary asymmetric flaperons' rotation.

Based on a known lateral-directional flight dynamics' mechanism (Ref.[39]), an initial hypothesis supposed that the source of excitation of the AWC may be attributed to a differential induced drag ensuing on the two wings, as a result of the differential deflection of the flaperons. However, since the unsteady aerodynamics is introduced by NASTRAN'S DLM, this kind of effect can not be observed; as a matter of fact, NASTRAN'S DLM does not capture wing-in-plane aerodynamic effects as it is only capable to estimate the generalised aerodynamic forces in a direction that is perpendicular to the aerodynamic panels (Figure 2.6). This limitation is nevertheless considered non restrictive, since the effect of an in plane differential induced drag, due to the deflection of the flaperons, is generally negligible and it is supposed to be insufficient to provoke a destabilising lateral dynamics (Ref.[11]).

In the attempt to explain the RPC phenomenon, the effects of the wing's wake over the XV-15 vertical fins are investigated. Figure 4.10 depicts an asymmetric deflection of the flaperons. Each rotated surface is associated with a wake and, since one flaperon is moved up and the other is moved down, the two wakes induce a lateral velocity field that generates a *sidewash velocity*. This lateral stream impacts over the vertical fins and produces a side force. The pulsating tail-side-force makes the fuselage to yaw and excites the asymmetric in plane mode, leading to a reduction, or even a loss, of stability. In Reference [11] this phenomenon allowed the explanation of the lateral PAO arose in the V-22.

The coupling between the flaperons' deflection and the tail side force is also described in Reference [40] page 21, where the sidewash velocity is said

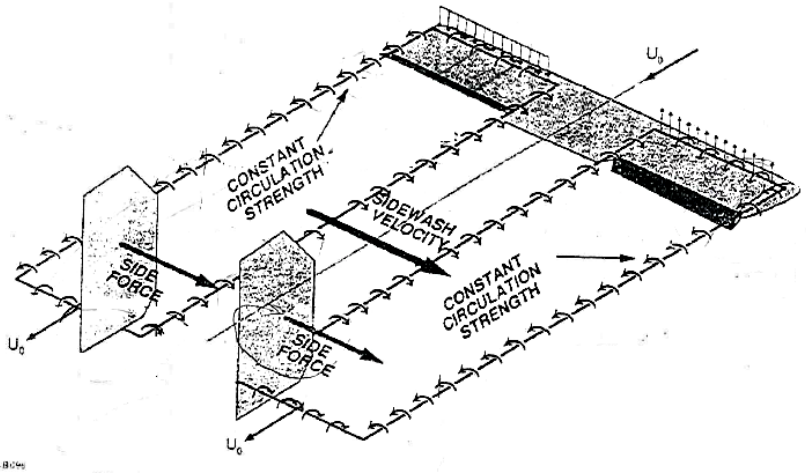

Figure 4.10: Flaperons induced aerodynamic force on vertical fins (Ref.[11])

to strongly participate the PIO event occurred in the AW609 incident of October 2015. The under-investigation aerodynamic interaction is there named *proverse yaw*.

To detect a possible *proverse yaw* dynamics, it is checked the element of the aerodynamic transfer function (TF) matrix $\mathbf{H}_{am}$ that represents the generalised aerodynamic force conjugate to the rigid yaw rotation due to asymmetric deflection of the flaperons. In MASST this aerodynamic TF, shown in Figure 4.12, is indexed as $H_{am}(6, 14)$, where number 6 refers to the yaw mode and number 14 to the asymmetric deflection of the flaperons. The aerodynamic influence coefficient is calculated as a function of the reduced frequency and the Mach number (Section 2.1.4). With reference to the modes shapes of Figure 4.11, an asymmetric deflection of the flaperons, needed to turn to the right, produces a (negative) generalised aerodynamic force that makes the tiltrotor aircraft to yaw to the right: a *proverse yaw* dynamics is detected.

This preliminary check verifies that the *proverse yaw* dynamics is correctly captured by the unsteady aerodynamics implemented in NASTRAN; its actual impact over the lateral PAO dynamics is hereafter quantified.

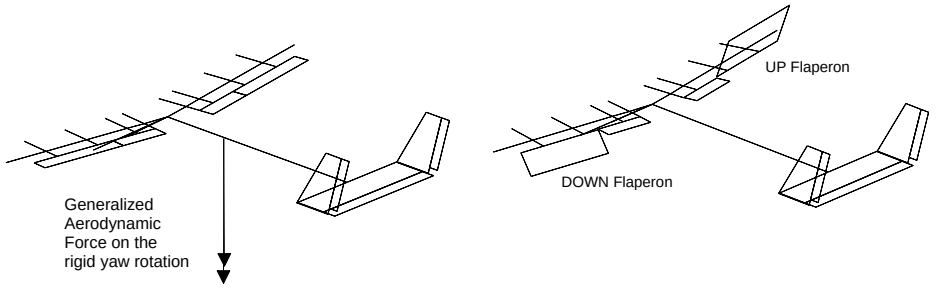

(a) Generalised Aerodynamic Force on the rigid yaw rotation (b) Flaperons' Asymmetric Deflection

Figure 4.11: Generalised Aerodynamic Force on the rigid yaw rotation due to asymmetric deflection of the flaperons

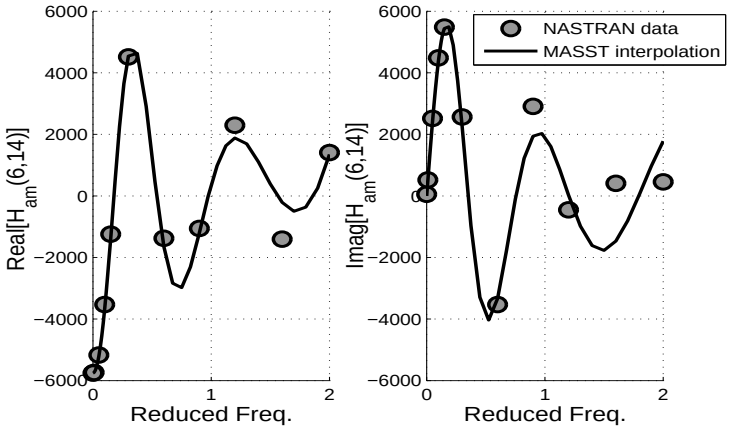

Figure 4.12: Transfer function $H_{am}(6,14)$, generalised aerodynamic force conjugate to the rigid yaw rotation (mode num. 6) due to asymmetric deflection of the flaperons (mode num. 14)

Figure 4.13 compares two MASST models obtained with and without the aerodynamic influence coefficient $H_{am}(6,14)$. The Bode plot shows the lateral acceleration response, measured at the pilot's seat, a_Y to an asymmetric deflection of the flaperons θ_f. A significant peak reduction associated with the AWC pole can be appreciated in the case of null $H_{am}(6,14)$.
The XV-15 dynamics is afterwards coupled with the biodynamic feedthrough provided by the *High Gain Pilot*. Figure 4.14 compares the LTFs obtained with and without the aerodynamic influence coefficient $H_{am}(6,14)$. It can be observed that, neglecting the aerodynamic contribution, the Nyquist's

lobe considerably reduces and the stability margins of the LTF strongly increase. As a result the influence of a *proverse yaw* is consistent and has a severe impact over the stability of the system.
The whole PAO lateral mechanism can be finally summarised as follows. The structural AWC mode induces lateral accelerations at the pilot's seat; these vibrations are filtered by the pilot's limbs that produce lateral movements of the control stick. The lateral movements of the stick cause the flaperons to deflect asymmetrically, generating a sidewash velocity that impacts over the tail fins and causes the fuselage to yaw. The subsequent movements of the fuselage excite the AWC mode producing a destabilising effect.

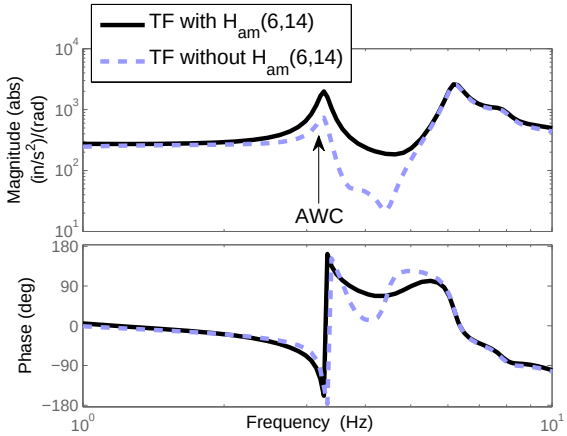

Figure 4.13: XV-15 transfer function from $\theta_f\,[rad]$ to $a_Y\,[in/s^2]$ with/out $H_{am}(6,14)$, that represents the generalised aerodynamic force conjugate to the rigid yaw rotation (mode num. 6) due to asymmetric deflection of the flaperons (mode num. 14)

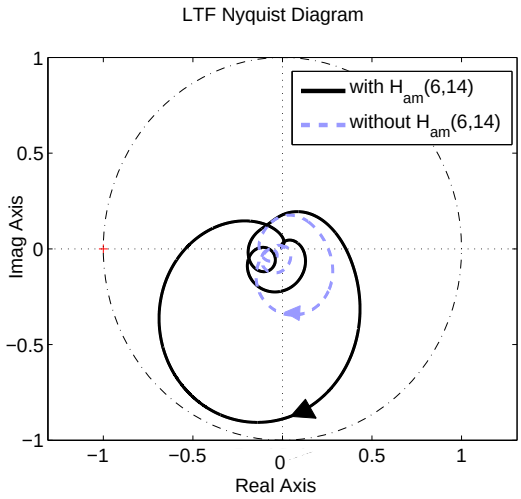

Figure 4.14: LTF Nyquist Diagram with/out $H_{am}(6,14)$, that represents the generalised aerodynamic force conjugate to the rigid yaw rotation (mode num. 6) due to asymmetric deflection of the flaperons (mode num. 14). $\tau = 0$ ms

4.2.3 Modification of the Vertical Fins' Geometry

Vertical Fins' Design

In Section 4.2.2 it is demonstrated that the lateral PAO strongly depends from an aerodynamic coupling that causes the tiltrotor's fuselage to yaw after an asymmetric deflection of the flaperons. The yawing motion is induced by a pulsating tail-side force that excites the asymmetric in plane mode of the wing. The geometry of the tail is consequently supposed to affect the trigger of the detected lateral RPC.

The presence of a vertical tail, represented in the XV-15 by two vertical fins, has a dual effect over the AWC mode.
The AWC mode, depicted in Figure 4.15(a), is characterised by an in-plane movement of the wing and a coherent yawing motion of the fuselage. Since NASTRAN's DLM is not capable to reproduce the aerodynamic effects due to the in-plane movements of the wing, the AWC aerodynamic damping is generated by the lateral displacements of the tail. In this sense, the larger the vertical tail surface the larger the aerodynamic damping associated with the AWC.
On the other hand, the presence of the two vertical fins is also producing the aerodynamic coupling with the aileron control surfaces, described in Section 4.2.2. In the following it is studied in deep the nature of this interaction.
Let us consider the flaperons' configuration of Figure 4.15(b). The velocity induced by the wake of a wing can be expressed as in Equation 4.7 (Ref. [41]).

$$v_{wake} = \frac{\Gamma}{4\pi} \cdot \frac{b}{b^2/4 - z^2} \ , \ |z| \leq b/2 \tag{4.7}$$

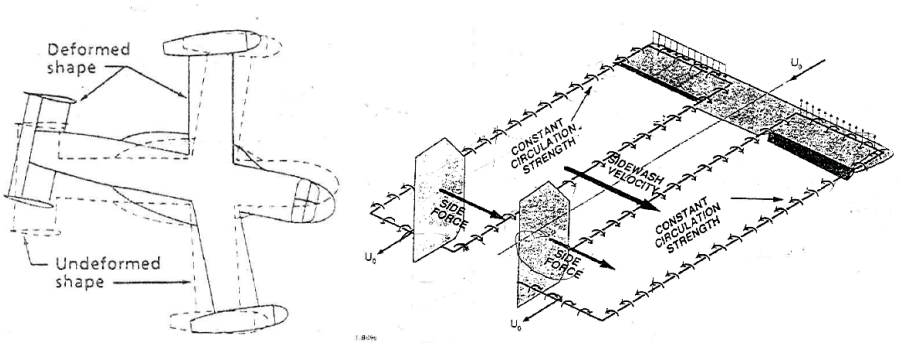

(a) AWC shape (b) Flaperons Induced Wake

Figure 4.15: Asymmetric in-plane mode of the wing

Where Γ is the wing's circulation, b is the wing's span and z is the free coordinate along the wing's span. The resulting induced velocity field around the vertical stabilisers is depicted in Figure 4.16. In the region above the plane of the wing, the induced airspeed generates a sidewash velocity directed along the positive direction of the y axis. On the contrary, in the region below the plane of the wing the velocity field is directed in the opposite direction. With reference to the configuration of the flaperons of Figure 4.15(b), the destabilising proverse yaw phenomenon is triggered by a side force directed along the positive direction of the y axis. Consequently, in order to potentially exalt the PAO dynamics, it is decided to reduce the tail surface eliminating the area that is arranged below the plane of the wing. The total surface of the vertical stabilisers, represented by the aerodynamic DLM's panels, is modified as depicted in Figures 4.18 and 4.19. If compared to the previous original tail configuration of Figure 4.17, it can be observed that the tail surface has been reduced to the only above-the-plane-of-the-wing section. It is estimated that the total surface's reduction accounts for a 30 % decrement (detailed data are listed in **Appendix E.3**). Due to the reduction of the area of the stabilisers, this new configuration is also expected to produce a lower aerodynamic damping.
The influence of possible time delays, introduced by the lateral control device, is initially neglected.

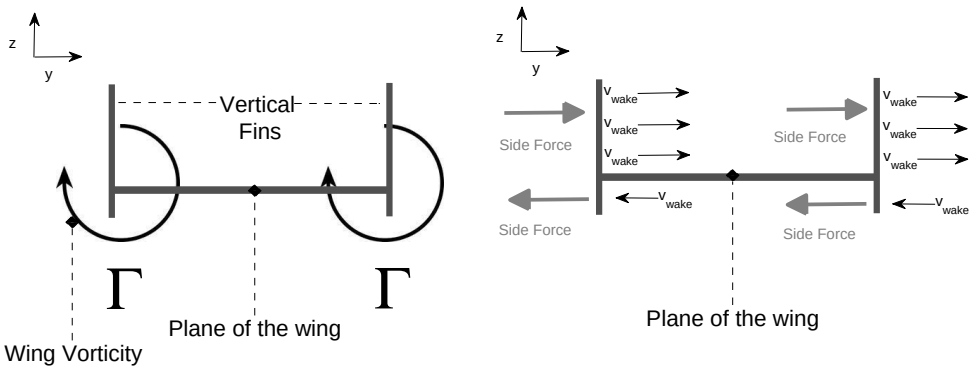

(a) Wing's Circulation Γ (b) Wake-induced velocity v_{wake}

Figure 4.16: Induced Velocity Field around Vertical Fins

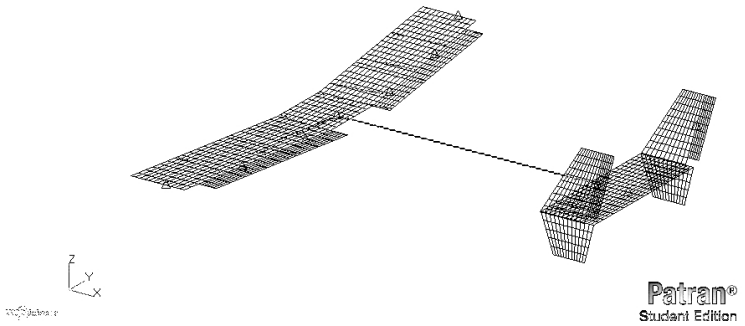

Figure 4.17: Nominal Tail Geometry view

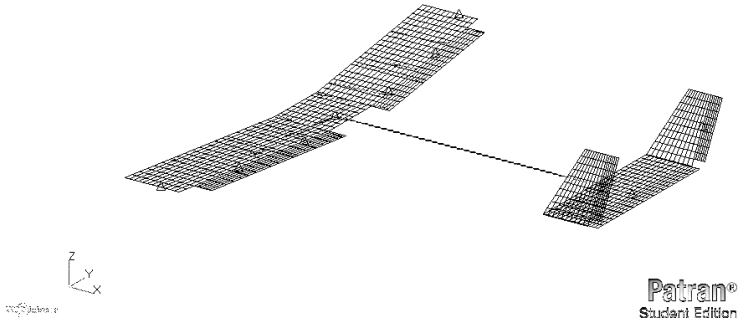

Figure 4.18: Modified Tail Geometry view

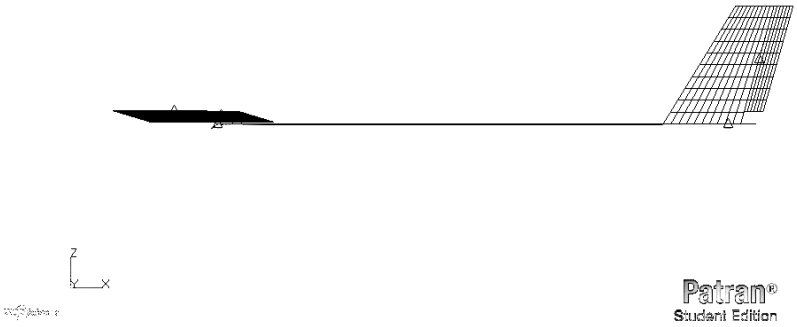

Figure 4.19: Modified Tail Geometry, plane xz view

Results

The transfer function of the lateral acceleration response a_Y, measured at the pilot's seat, to the flaperons' deflection θ_f is reported in Figure 4.20. The results associated with the nominal tail design are compared with the ones of the modified configuration. It can be observed that the new frequency response shows a higher peak in coincidence with the AWC frequency, near 3 Hz. The effect induced by the aerodynamic damping variation, caused by the smaller aerodynamic surface, may be considered negligible with respect to the evident static gain augmentation. The two responses overlap for frequencies higher than 5 Hz.

The effect of the increased response is also visible in Figure 4.21 which compares the results obtained considering the feedback of the three nominal Test Pilots. With respect to the nominal configuration (Figure 4.6), the LTF Nyquist diagrams strongly enlarge, reducing the stability margins. The most critical feedback is provided by Test Pilot 2 that exhibits the widest response. Moreover, Figure E.7, reported in **Appendix E**, demonstrates that possible time delays over the pilot/control device can consistently reduce the stability margins of the system.

The generalised aerodynamic force $H_{am}(6, 14)$ on the yaw mode due to asymmetric deflection of the flaperons is subsequently quantified. Figures 4.22 and 4.23 compare the aerodynamic TF $H_{am}(6, 14)$ associated with the nominal and modified tail configurations. It can be observed that the magnitude of the generalised aerodynamic force increases whit respect to the nominal configuration. For zero reduced frequency the phenomenon is almost doubled in value. Figure E.8, reported in **Appendix E**, compares the LTFs with and without the aerodynamic TF $H_{am}(6, 14)$, confirming the strong influence of the generalised aerodynamic force on the yaw mode due to an asymmetric deflection of the flaperons.

In conclusion, when the tail is modified as discussed (Figure 4.18), the stability margins of the PVS decrease and the explanation is rooted in the increased magnitude of the generalised aerodynamic force on the yaw mode due to asymmetric deflection of the flaperons. The most critical biodynamic feedback is provided by nominal Test Pilot 2 and the introduction of possible time delays may lead the PVS to the limit of stability.

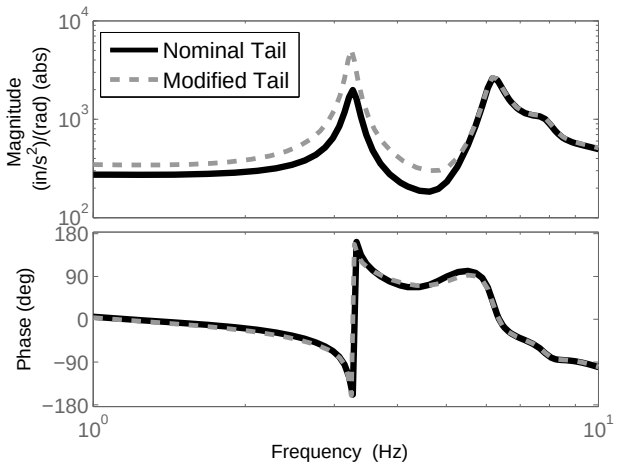

Figure 4.20: XV-15 transfer function from θ_f $[rad]$ to a_Y $[in/s^2]$, comparison between tail's geometrical configurations (Figs. 4.17, 4.18)

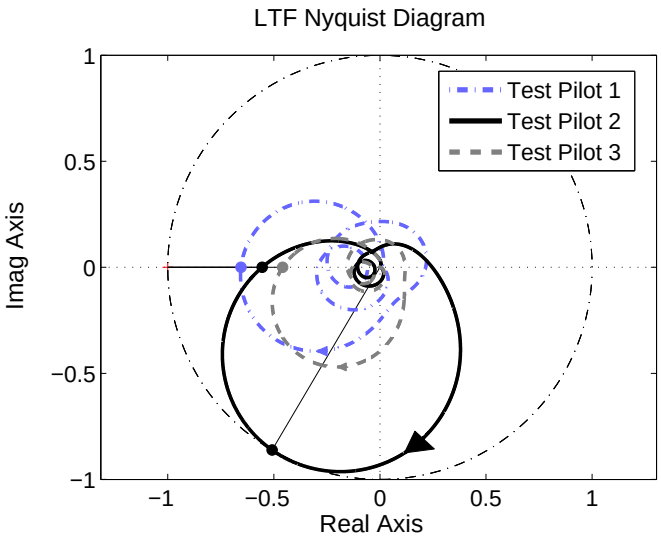

Figure 4.21: LTF Nyquist Diagram, modified tail geometry (Fig. 4.18), τ=0 ms

	$\mathbf{G_m}$[dB]	f($\mathbf{G_m}$)[Hz]
Pilot 1	3.68	3.25
Pilot 2	5.11	3.32
Pilot 3	6.77	3.28
	$\mathbf{P_m}$[dB]	f($\mathbf{P_m}$)[Hz]
Pilot 1	–	–
Pilot 2	59.47	3.25
Pilot 3	–	–

Table 4.5: Stability Margins, modified tail geometry (Fig. 4.18)

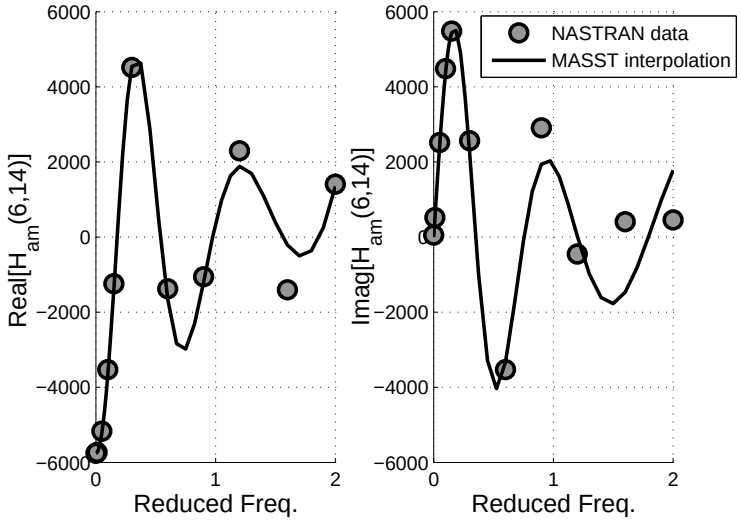

Figure 4.22: Nominal tail geometry: transfer function $H_{am}(6,14)$, generalised aerodynamic force conjugate to the rigid yaw rotation (mode num. 6) due to asymmetric deflection of the flaperons (mode num 14)

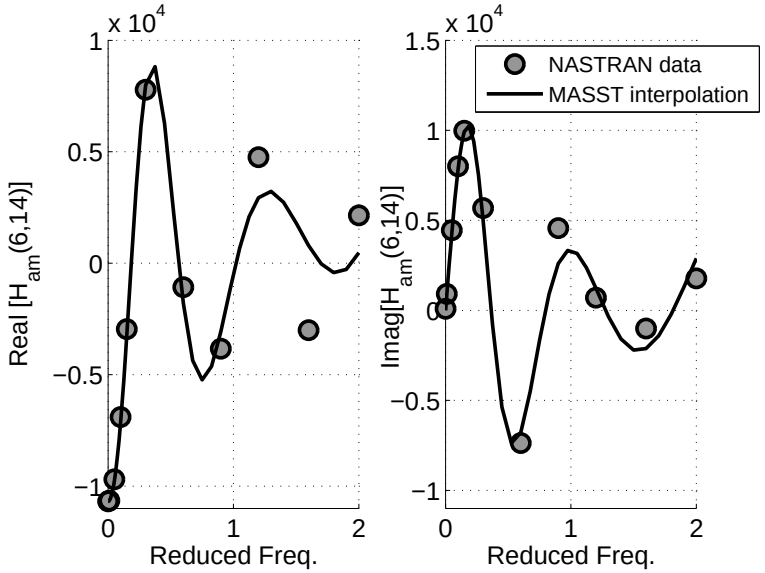

Figure 4.23: Modified tail geometry: transfer function $H_{am}(6,14)$, generalised aerodynamic force conjugate to the rigid yaw rotation (mode num. 6) due to asymmetric deflection of the flaperons (mode num 14)

4.2.4 Means of Prevention

In Section 4.2.3 the effects of a geometrical tail's modification are investigated. Specifically, in order to exalt the PAO dynamics, the vertical fin surface is reduced retaining the section located above the plane of the wing. In the following it is intended to study the inverse design considering a tail with vertical fins located below the plane of the wing. Based on the assumptions of Section 4.2.3, in this region the circulation Γ produces a sidewash velocity that, colliding with the vertical stabilisers, is supposed to counteract the AWC oscillations. This reversed tail configuration does not actually represent an effective engineering option; one of the main issues can be related to the possible violation of the ground clearance during take-off and landing. However, the proposed tail design is aimed to demonstrate that the proverse yaw dynamics can be counteracted moving part of the vertical fins' surface below the plane of the wing.

The tail geometry, studied in Section 4.2.3, is reported in Figure 4.24. It represents the case of a tail located above the plane of the wing and, for simplicity, it is from now on called *case 1*. The opposite design is depicted in Figure 4.25 and it is hereafter referred to as *case 2*.

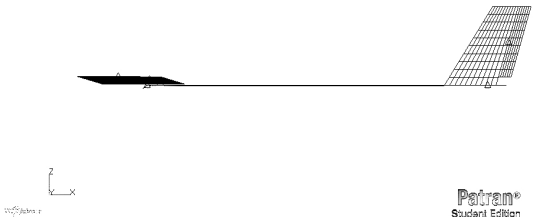

Figure 4.24: Tail above the plane of the wing, **case 1**

Figure 4.25: Tail below the plane of the wing, **case 2**

Figure 4.26 compares two MASST models obtained considering the two opposite tail configurations (Figs.4.24 and 4.25). For both cases it is evaluated the transfer function of the lateral acceleration response a_Y, measured at the pilot's seat, to the flaperons' deflection θ_f. The Bode plot shows that the magnitude of the two responses overlap with good approximation near the AWC frequency (near 3 Hz). However, it can be noticed that, in coincidence of the same frequency, the phase diagram is swapped. For *case 1* the phase is close to 180° near 3 Hz, while in *case 2* the phase is shifted to 0°. As a result, the response of the system is reversed when the tail configuration of Figure 4.25 is adopted.

The stability of the PVS is subsequently examined. Pilot-in-the-Loop analyses are performed considering the most critical biodynamic feedthrough, provided by Test Pilot 2 and the influence of possible time delays, introduced by the lateral control device, is initially neglected.
In the root locus of Figure 4.27, the squared markers represent the poles associated with the open loop dynamics, i.e. without the pilot's feedback, whereas the circular markers are associated with the roots obtained after Pilot-in-the-Loop analysis. In *case 1* the pilot's BDFT causes the AWC pole to shift towards the right half of the complex plane, thus becoming less stable, while in *case 2* the same pole is shifting to the left, becoming more stable. The reason for this opposite behaviour is rooted in the aerodynamic contribution provided by the generalised force on the yaw mode due to asymmetric deflection of the flaperons. Figures 4.28 and 4.29 show the aerodynamic transfer function $H_{am}(6, 14)$ obtained for *Cases 1* and *2*. It can be observed that the two functions have comparable magnitude but opposite sign. As a consequence the unsteady aerodynamic participation is reversed.

Figure 4.30 compares the LTFs associated with the two tail designs, showing that the configuration held by *case 2* provides considerably higher stability margins. The discrepancy between the two cases is further highlighted after the introduction of possible time delays τ over the control device. Figure 4.31 shows the gain margin G_m as a functions of variable time delays τ. If compared with *Case 2*, *Case 1* shows much lower stability margins and for time delays greater than 50 ms G_m is almost null. *Case 2* is instead characterised by elevated gain margins and, for time delays greater than 20 ms, G_m can not be even defined, as the LTF Nyquist plot is not crossing the negative real axes in the round of the AWC frequency. By way of example,

the case of $\tau = 50$ ms, considered representative, is shown in Figure 4.32.*

In conclusion, the obtained results highlight the fact that the design of the vertical fins has a non-negligible impact over the lateral PAO mechanism. In particular, the trigger of this phenomenon can be favoured if the vertical fins are located in a region that is settled above the plane of the wing. In this sense it is recommended to distribute part of the vertical aerodynamic surface below the plane of the wing, in order to compensate the effect of the wing's vorticity due to an asymmetric deflection of the flaperons after a roll manoeuvre.
The analyses of Section 4.2.1 coherently demonstrate that the nominal tail configuration of the XV-15 (Fig. 4.17) guarantees the PVS stability. As a matter of fact, a large fraction of the area of the vertical stabilisers (≈30%) is located below the plane of the wing. In the case of the V-22 (Ref.[11]) the area distributed below the plane of the wing was probably insufficient to counteract the instability mechanism. It is finally speculated that the described lateral unstable oscillations may also occur in the AW609, which is characterised by a single vertical stabiliser positioned at midspan above the plane of the wing.

Other means of prevention may be provided by the implementation of structural filters; in Ref.[11] to eliminate the AWC instability, asymmetric notch filters are incorporated into the flight control system. In this Section this kind of solution is not contemplated, but it is given serious importance in Chapter 6 for the prevention of vertical PAOs.

*Figure 4.32 is pointing out some gain margin also for *case 2*; however, this crossing is not to be taken into account since it corresponds to frequencies than are lower than 1 Hz, and thus correspond to the region of the pilot's voluntary response. Since no voluntary response is modelled, that region of the Nyquist diagram is not be considered representative of a real closed loop dynamics.

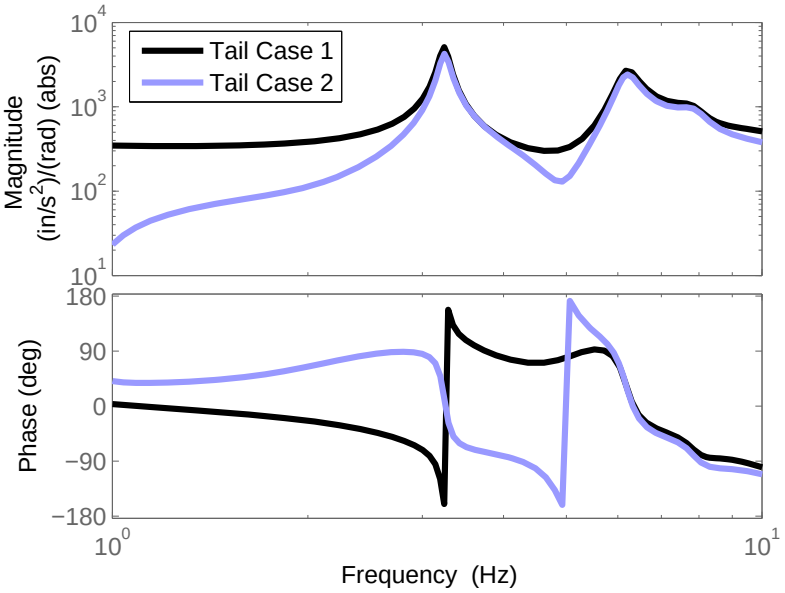

Figure 4.26: XV-15 transfer function from $\theta_f\ [rad]$ to $a_Y\ [in/s^2]$, comparison between tail's geometrical configurations (Fig.s 4.24, 4.25)

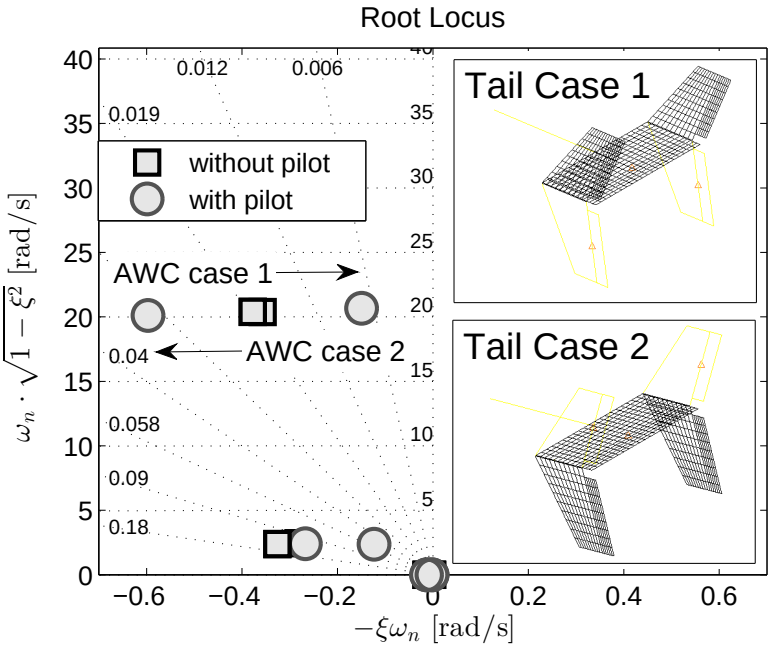

Figure 4.27: Root Locus, comparison between tail's geometrical configurations

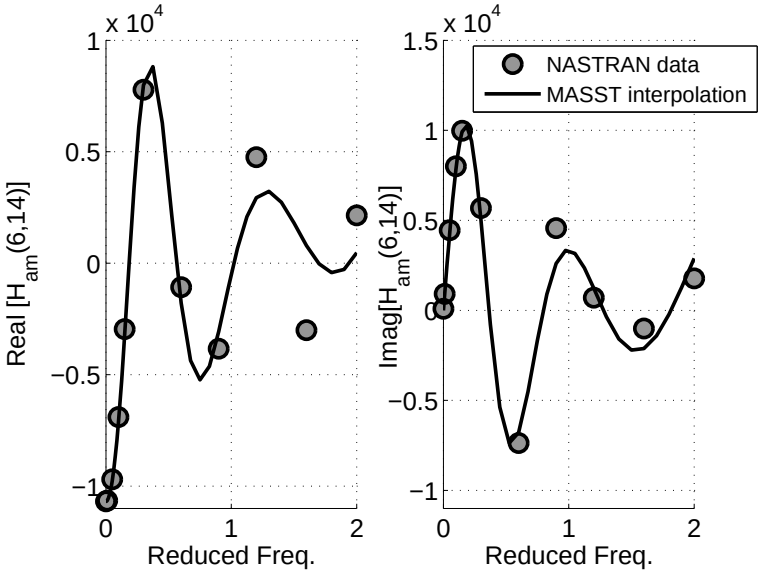

Figure 4.28: **Case 1** *(Fig. 4.24): transfer function $H_{am}(6,14)$, generalised aerodynamic force conjugate to the rigid yaw rotation (mode num. 6) due to asymmetric deflection of the flaperons (mode num. 14)*

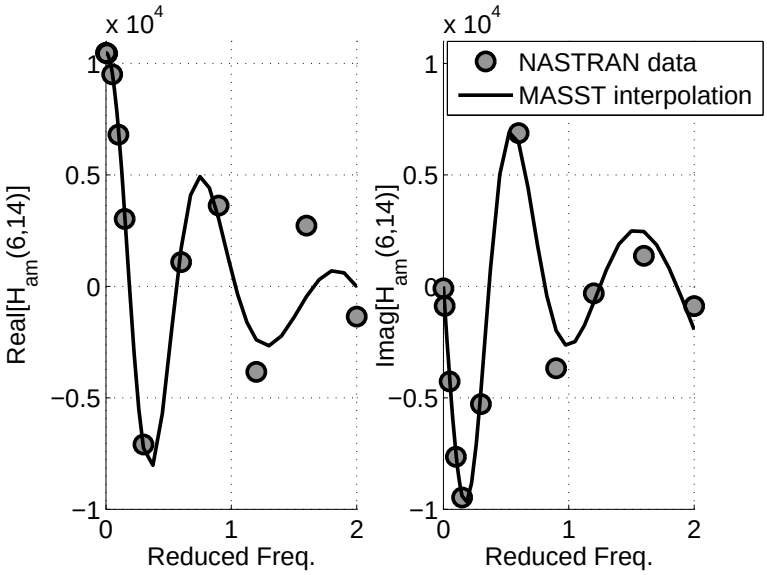

Figure 4.29: **Case 2** *(Fig. 4.25): transfer function $H_{am}(6,14)$, generalised aerodynamic force conjugate to the rigid yaw rotation (mode num. 6) due to asymmetric deflection of the flaperons (mode num. 14)*

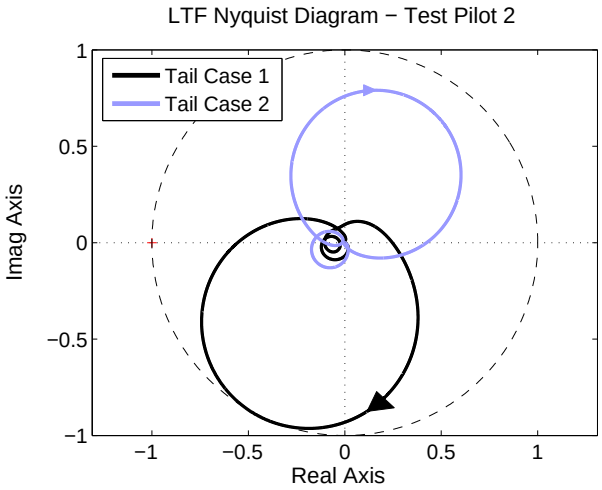

Figure 4.30: LTF Nyquist Diagram, comparison between tail's geometrical configurations (Fig.s 4.24, 4.25)

Tail Case	$\mathbf{G_m}$**[dB]**	$\mathbf{f(G_m)}$**[Hz]**
Case 1	5.11	3.32
Case 2	19.80	2.78
	$\mathbf{P_m}$**[dB]**	$\mathbf{f(P_m)}$**[Hz]**
Case 1	59.47	3.25
Case 2	–	–

Table 4.6: Stability Margins - Tail Geometrical Modification

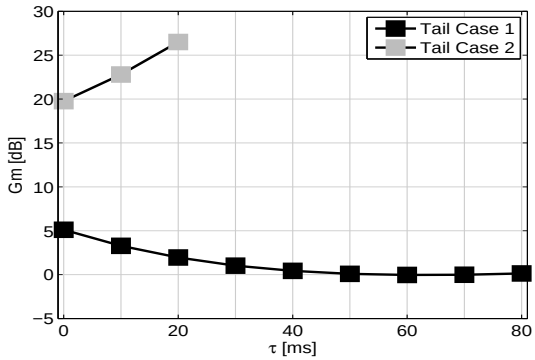

Figure 4.31: Gain Margin with respect to Time Delay

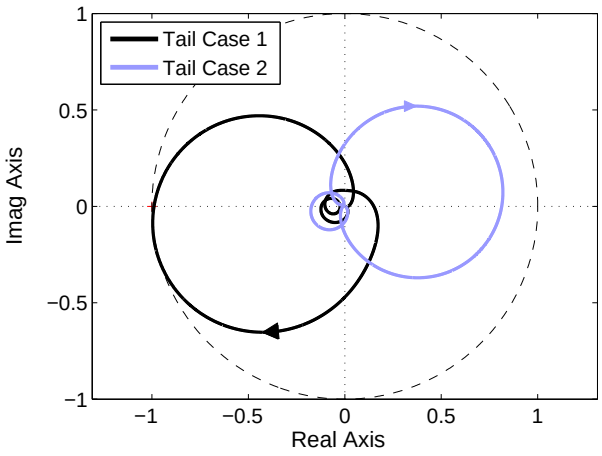

Figure 4.32: LTF Nyquist Diagram, comparison between tail's geometrical configurations and time delay (Fig.s 4.24, 4.25)

Tail Case	$\mathbf{G_m}$**[dB]**	$\mathbf{f(G_m)}$**[Hz]**
Case 1	0.10	3.25
Case 2	–	–
Tail Case	$\mathbf{P_m}$**[dB]**	$\mathbf{f(P_m)}$**[Hz]**
Case 1	5.47	3.24
Case 2	–	–

Table 4.7: Stability Margins - Tail Geometrical Modification

Chapter 5

Instability Mechanism on the Longitudinal Axis

5.1 Longitudinal PVS Dynamics

This Chapter is dedicated to the study of aeroelastic RPC instabilities involving the tiltrotor's longitudinal dynamics. In particular, it is intended to examine the relationship between the pilot's longitudinal stick control input and the subsequent vehicle motion in the longitudinal direction.

The vehicle longitudinal dynamics are schematised in Figure 5.1. The for-aft movements of the stick generate both a symmetric longitudinal cyclic input and a deflection of the elevator. Consequently, along the open loop line, a longitudinal displacement of the stick δ_X enters in a double load path: $G_{LC}(s)$ handles the longitudinal cyclic input while $G_E(s)$ handles the elevator's rotation. $G_{LC}(s)$ and $G_E(s)$ are defined, in Equation 5.1, by the

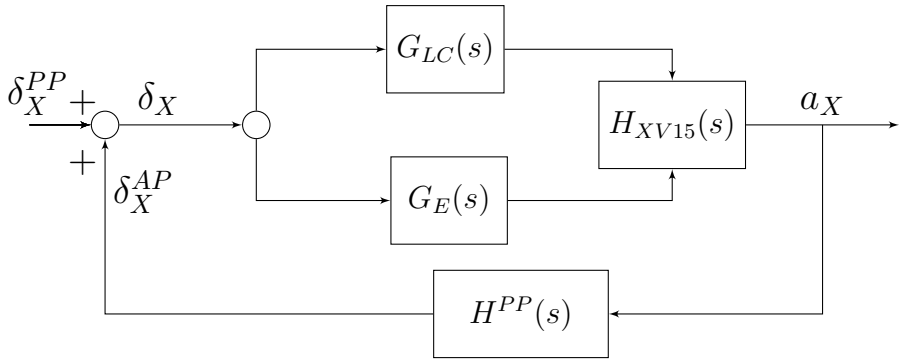

Figure 5.1: Longitudinal PVS Block Scheme

product of a gear ratio G and an exponential function that introduces a possible control device time delay τ.

$$G_{LC}(s) = G_{LC_0} \cdot e^{-\tau \cdot s} \qquad G_E(s) = G_{E_0} \cdot e^{-\tau \cdot s} \tag{5.1}$$

The gear ratios G_{LC_0} and G_{E_0} are scheduled with respect to the NAC angle, as shown in Figure 5.2. According to Ref.[32], G_{LC_0} is maximum in APMODE and null in HEMODE. G_{E_0} is instead constant, as reported in Ref.[26]. Figures 5.3, 5.4 and 5.5 clarify the relationship between the actuation of the stick, along the longitudinal direction, and the cyclic/elevator output. In APMODE (Fig.5.3) only the elevator is actuated while in HEMODE (Figs.5.4 and 5.5) both the elevator and the longitudinal cyclic are actuated.

In Fig.5.1 the involuntary/passive pilot longitudinal axis transfer function $H^{PP}(s)$ is put in feedback with the tiltrotor's aeromechanics $H_{XV15}(s)$. Due to a longitudinal acceleration a_X the pilot generates the output δ_X^{PP}, which represents the involuntary longitudinal deflection of the stick. The influence of a stick displacement δ_X^{AP}, introduced by a voluntary/active pilot, is not contemplated in the analyses.

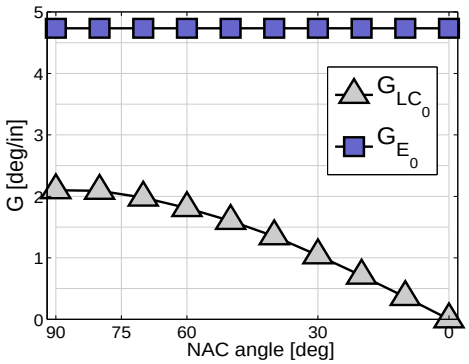

Figure 5.2: Longitudinal Gear Ratios

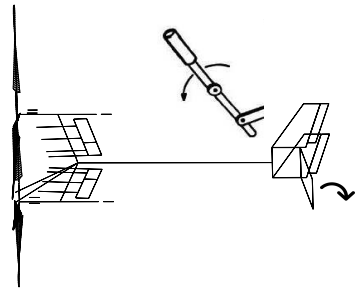

Figure 5.3: APMODE elevator input

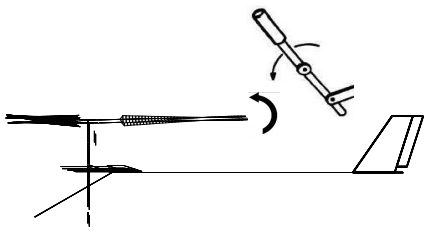

Figure 5.4: HEMODE longitudinal cyclic input

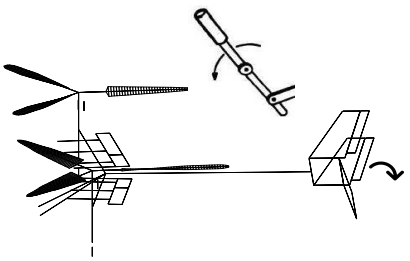

Figure 5.5: HEMODE elevator input

5.1.1 Longitudinal Pilot/Control Device Dynamics

The longitudinal pilot's characterisation is derived from Ref.[11]. This work reports the results of an experiment conducted on the V-22 cockpit console to obtain bio-response data. An isolated control console, consisting of the V-22 cockpit, seats, instrument panels and controls is mounted on rollers to permit fore-and-aft motion of the entire console. The shake tests are performed by shaking the console base with the pilot sitting in the seat and his hand on the controls. Figure 5.6 presents the identified pilot/for-and-aft stick transfer functions from shake tests of the cockpit console for two different pilots. However the following aspect must be specified. In Ref.[11], to account for the possibility of additional pilot variability, the measured transfer function data are adjusted to a higher gain based on twice the measured inflight pilot gain. In other words, data reported in Figure 5.6 of Ref.[11] do not represent the direct results of the shake tests. They correspond to a set of manipulated data, whose magnitude has been enlarged to account for the possibility of additional pilot variability. As a result they do not describe the nominal dynamics of a longitudinal pilot and are instead representative of a longitudinal axis High Gain Pilot transfer function.

To obtain an analytical expression of the longitudinal BDFT, it is performed, by means of MATLAB routines, an identification of the analytical pilot mathematical model presented in Figure 5.6. The transfer function that results from the identification process is reported in Equation 5.2 and it is characterised by two zeroes and four complex conjugate poles. The biodynamic pole is defined by a natural frequency of 4.03 Hz and a damping equal to 20.01%. Figure 5.7 reports the sample data acquired from Ref.[11] and the Bode diagram of the identified transfer function. The fitting is considered satisfying.

$$\frac{\delta_X^{PP}}{a_X} = \frac{-867.9 \cdot s^2 - 1.349 \cdot 10^4 \cdot s - 1.98 \cdot 10^6}{s^4 + 64.91 \cdot s^3 + 2833 \cdot s^2 + 5.171 \cdot 10^4 \cdot s + 1.05 \cdot 10^6} \tag{5.2}$$

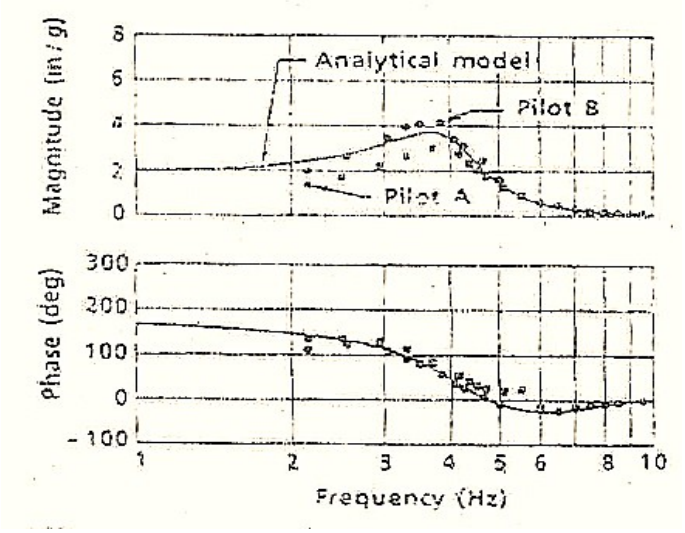

Figure 5.6: Pilot F/A stick math model Ref.[11]

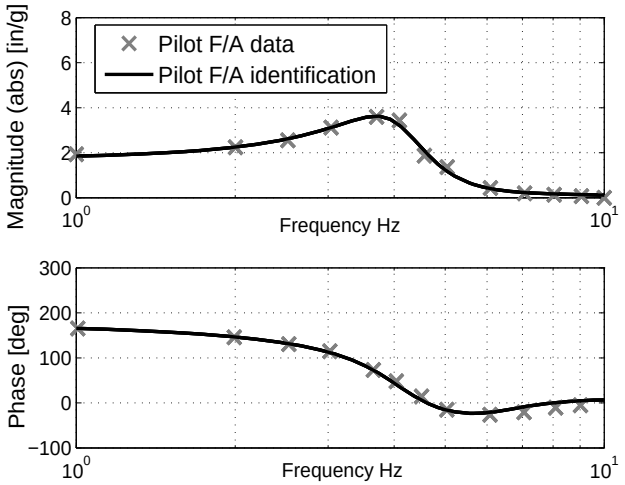

Figure 5.7: Pilot F/A stick math model Identification from data of Ref.[11]

5.1.2 Pilot-in-the-loop Results

With the introduction of the pilot, the PVS is studied using robust stability analysis techniques. According to the procedure exposed in Section 2.5.2, Nyquist criterion is applied to the loop transfer function of the longitudinal PVS represented in Figure 5.1. Pilot-in-the-loop analyses are performed considering two configurations, corresponding to APMODE and HEMODE. In both cases a set of representative airspeeds is considered. The influence of possible time delays is not contemplated in the analyses. The flight height is maintained at Sea Level (SL).

Figure 5.8 presents the results obtained in APMODE. The robust analysis returns stable conditions for all the considered airspeeds. The gain margin associated with 280 knots equals 1.64 dB, as reported in Table 5.1. The low gain margin associated with 280 knots can be justified considering that the longitudinal BDFT is characterised by a High Gain Pilot transfer function, as discussed in 5.1.1. In particular, to account for the possibility of additional pilot variability, the measured transfer function of Ref.[11] considers a static gain which is doubled with respect to the measured V-22 inflight data. Thanks to the linearity of the system, the gain margin for nominal conditions can be easily estimated. For a halved pilot static gain the gain margin is equal to 7.66 dB, which returns a stable and robust PVS. Figure 5.9 presents the results obtained in HEMODE. Again the system in stable and shows high gain margins for all the selected airspeeds.

As a result, no unstable RPCs are detected along the longitudinal axis. This result can be justified as follows. In Ref.[11] it is described an unfavourable coupling occurred for the V-22, that destabilised the airframe SWC mode. The unstable oscillations were excited in high speed airplane mode flight and were due to a pulsating thrust induced by the oscillations of the thrust command lever (TCL), caused by the involuntary pilot response to the longitudinal accelerations of the cockpit. In the XV-15, due to the frequency separation between the pilot's biodynamic pole, located near 4 Hz, and the SWC mode frequency of the airframe, positioned near 6 Hz, the possibility for an unstable RPC to occur is low. Moreover, the V-22 TCL is replaced in the XV-15 by a power lever (PL), whose motion can not be directly excited by longitudinal accelerations.
In summary, thanks to an adequate decoupling between the longitudinal pilot's dynamics and the airframe symmetric elastic modes and thanks to the specific cockpit configuration, that presents a PL in substitution of the TCL, the XV-15 is demonstrated not to be prone to longitudinal PAOs.

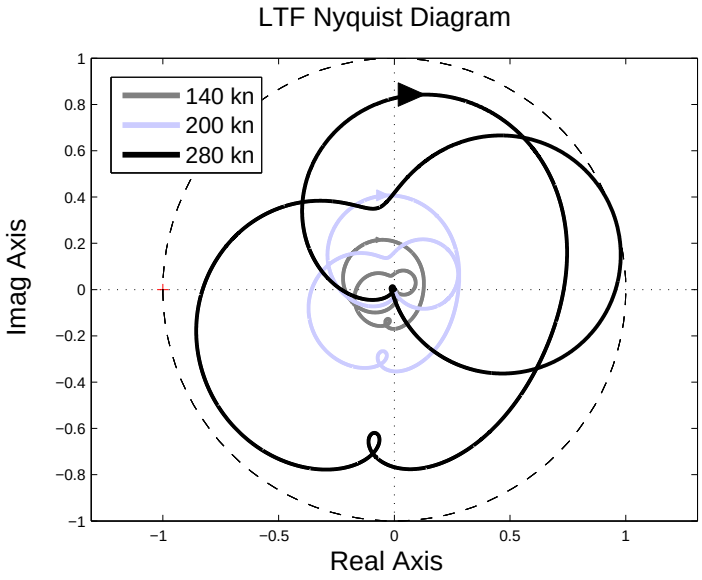

Figure 5.8: LTF Nyquist Diagram - APMODE, τ=0ms

airspeed	$\mathbf{G_m}$ [dB]	f [Hz]
140 kn	15.68	4.15
200 kn	8.98	4.16
280 kn	1.64	4.16

Table 5.1: APMODE Gain Margins

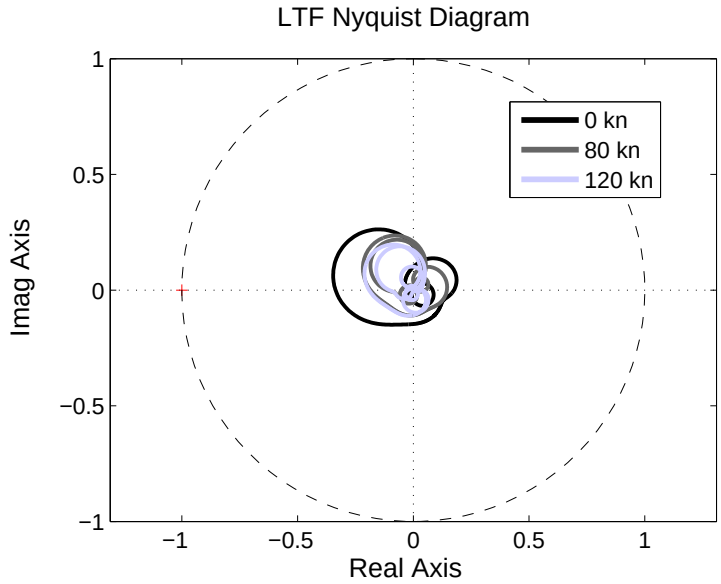

Figure 5.9: LTF Nyquist Diagram - HEMODE, τ=0ms

airspeed	$\mathbf{G_m}$ [dB]	f [Hz]
0 kn	9.48	5.33
80 kn	14.70	5.11
120 kn	14.40	5.10

Table 5.2: HEMODE Gain Margins

Chapter 6

Instability Mechanism on the Vertical Axis

6.1 Vertical PVS Dynamics

In this Chapter it is intended to investigate the trigger of possible PAO events along the vertical axis. Differently from the V-22, the XV-15 does not present a typical airplane thrust command lever (TCL) but a power lever (PL) that resembles a traditional helicopter collective lever, depicted in Figure 6.1. It is known, by literature, that in helicopters, the specific collective lever geometry enables the trigger of a PAO phenomenon called *vertical bounce* (Refs. [12, 9, 14]). It is caused by pulsating thrust induced by an oscillation of the collective control lever inadvertently introduced by the pilot in response to the cockpit vertical oscillations. It is subsequently speculated that a similar phenomenon may verify also in tiltrotors.

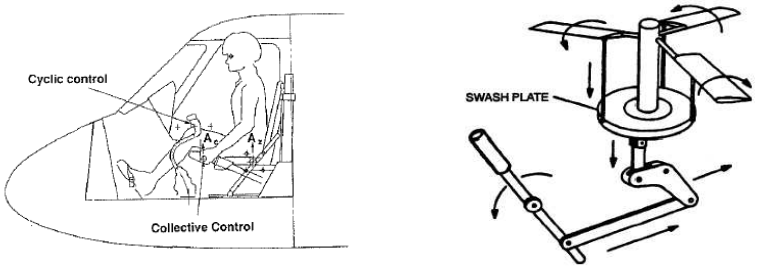

(a) Seat/Stick configuration (b) Power Lever kinematics

Figure 6.1: Power Lever (PL)

The XV-15 vertical dynamics are represented in the block scheme of Figure 6.2. Along the open loop line, a PL input δ_Z enters in a double load path: $G_t(s)$ connects the power lever to the engine power, by means of the throttle control θ_t, while $G_0(s)$ handles the collective pitch θ_0. $G_t(s)$ and $G_0(s)$ are defined in Equation 6.1 by the product of a gear ratio $\widetilde{G}$ and an exponential function, that introduces a possible control device time delay τ.

$$G_t(s) = \widetilde{G_t} \cdot e^{-\tau \cdot s} \qquad\qquad G_0(s) = \widetilde{G_0} \cdot e^{-\tau \cdot s} \tag{6.1}$$

$\widetilde{G}_0$ is scheduled with respect to the NAC angle, as reported in Ref.[32]. Figure 6.3 shows that the collective input is maximum in HEMODE (NAC90) and null in APMODE (NAC0). As a consequence, in APMODE the vertical loop closure is allowed by the only engine load path through the gear ratio $\widetilde{G}_t$, that, according to Ref.[26], is constant.

A RPM "Beta" Governor is also included into the XV-15 vertical dynamics through the transfer function (TF) $H_{\mathrm{GOV}}(s)$. Traditionally helicopters use throttle governing where the pilot sets collective pitch and the control system adjusts engine power to maintain RPM (Ref.[31]). On the other hand, turboprops generally use "Beta" governing, where the pilot sets engine power and the governor adjusts the propeller angle of attack to maintain the RPM. For the specific tiltrotor case, a helicopter governing scheme would encounter critical working conditions in APMODE configuration. According to Ref.[31], the torque exhibits high load variations with respect to a small collective pitch fluctuation. As a consequence, small pilot's PL displacements would cause unsustainable torque transients. For this reason an

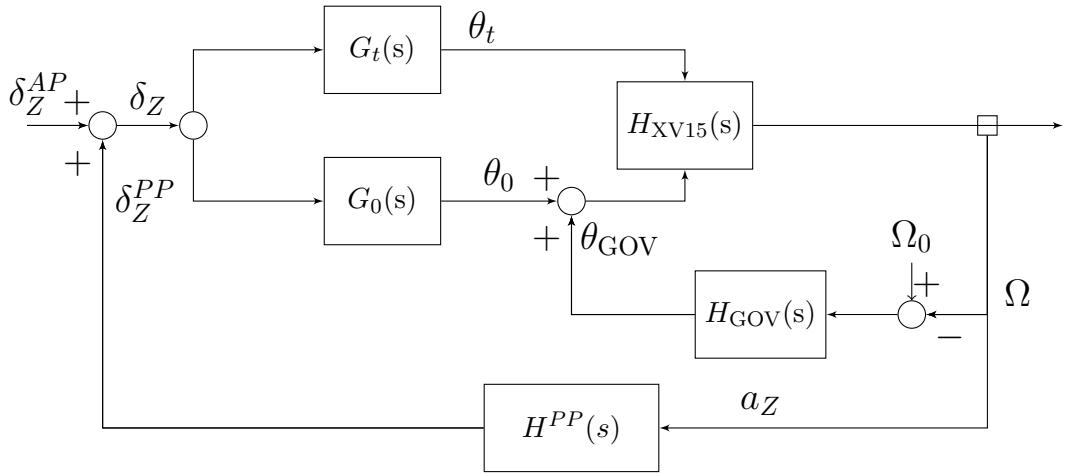

Figure 6.2: PVS Block Scheme - XV-15 Vertical Dynamics

airplane-like "Beta" governing scheme was chosen during the XV-15 design, and was even considered suitable for the later tiltrotors.
The governor control law, reported in Ref.[31] and Ref.[32], is represented by a PI controller that considers as input the error between the requested RPM Ω_0 and the measured speed Ω. The controller's gains are scheduled with respect to the NAC angle.

The vertical axis passive pilot transfer function $H^{PP}(s)$ is put in feedback with the whole vertical dynamics. Due to a vertical acceleration a_Z the pilot generates a vertical PL displacement δ_Z^{PP}. The influence of a PL displacement δ_Z^{AP}, induced by a voluntary/active action of the pilot, is not contemplated in the analyses.

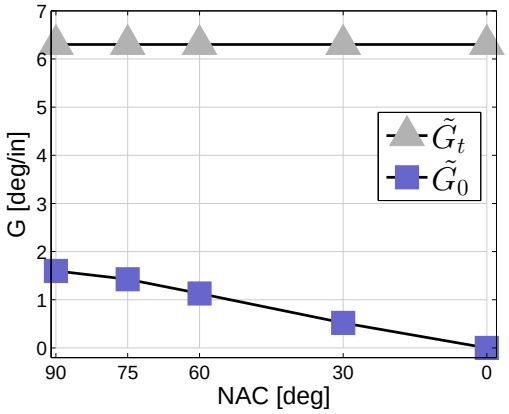

Figure 6.3: Throttle and Collective Gear Ratios Refs.[26, 32]

6.1.1 Vertical Pilot/Control Device Dynamics

The characterisation of the vertical axis pilot transfer function is derived from the work of Mayo of Ref.[12]. This paper resumes the results of an experimental campaign aimed at obtaining bio-response data on a Sikorsky motion-base simulator. The simulator cockpit set up for this test campaign involves the conventional helicopter seat, and cyclic, collective and pedal controls. Pilot's collective stick motion is recorded while vertical sinusoidal commands are applied to the simulator platform at discrete frequencies ranging from 1 to 5 Hz. The transfer functions of involuntary control inputs to vertical vibration through the dynamics of the coupled seat/torso/limb/stick system (BDFT) are determined for pilots of various body types. In particular the Test Pilots are distinguished into ectomorphic, small and lean build, and mesomorphic, large bone structure and muscle build. A total of six pilots are subjected to the tests.

The analytical expression of the vertical axis pilot transfer function, written with respect to the relative acceleration of the hand, is reported in Equation 6.2. δ_Z^{PP} represents the involuntary power lever displacement and a_Z represents a vertical acceleration measured at the pilot's seat. The structural properties of Mayo's TFs are reported in Table 6.1, both for the ectomorphic and mesomorphic case.

$$\frac{\delta_Z^{PP}}{a_Z} = -\frac{s}{(s+\omega_h)^2}\frac{s+1/\tau_p}{s^2+2\xi_p\omega_p s+\omega_p^2} \tag{6.2}$$

Pilot	ω_p [rad/s]	ξ_p [%]	τ_p [sec]	ω_h [rad/s]
Ectomorphic	21.23	32	0.117	3.10
Mesomorphic	23.56	28	0.107	3.10

Table 6.1: Mayo's TFs Structural Properties Ref.[12]

The Bode plots of the pilot's TFs are shown in Figure 6.4. It can be observed that the two pilots present a resonance near 3 Hz and the ectomorphic pilot exhibits a higher static response.
A final aspect should be specified; the frequency band below 1 Hz is associated with the voluntary pilot's response. Since the pilots' models proposed by Mayo describe the only involuntary response of the pilot, the low frequency asymptotic behaviour is vanished by a second-order high pass filter with cut off frequency ω_h, reported in Table 6.1.

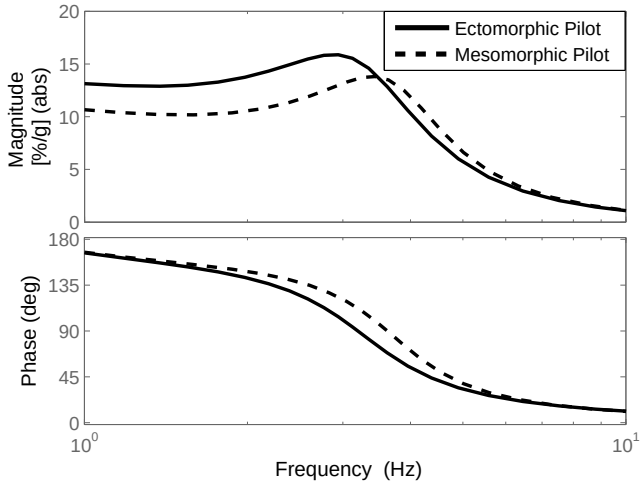

Figure 6.4: Mayo's Biodynamic Feedthrough (BDFT), from a_Z [g] to δ_Z [%]

6.2 Pilot-in-the-loop Results

6.2.1 PAO Analysis in Hover

As mentioned in Section 6.1, the vertical bounce is a PAO phenomenon typical of helicopters. Many studies (Refs. [9, 12, 14]) have been focused on this mechanism and they have explained that the possible development of the instability is rooted in the coupling of the first collective flap (or coning) mode of the main rotor and the biodynamic mode of the pilot's arm holding the collective control inceptor.
On classical stiff-in-plane gimballed tiltrotors the coning mode frequency is over the pilot's voluntary/involuntary bandwidth, but the vertical bounce phenomenon may still arise if the pilot's biomechanics interact with the airframe elastic modes, in particular with the SWB mode. Since the XV-15 exhibits a SWB frequency near 3 Hz, that lightly varies with the conversion angle (Section 3.5.2), it is speculated that the pilot's BDFT, showing a resonance in the range between 3-4 Hz (Figure 6.4), may interact with the wing's oscillations.

The initial analyses are run considering a configuration that corresponds to HEMODE and null forward speed, i.e. the hovering flight. Time delays, potentially introduced by the control device, are neglected.
The XV-15 TF of the vertical acceleration a_Z, measured at the pilot's seat, in response to the power-lever input δ_Z is represented in the Bode Diagram of Figure 6.6. The SWB is located at a frequency of 3.01 Hz.

With the subsequent introduction of the Pilot, the system is studied using robust stability Nyquist criterion, according to the procedure exposed in Section 2.5.2. The loop closure is performed as depicted by the block scheme of Figure 6.2. It is specified that the pilot's feedback is conservatively provided by Mayo's ectomorphic pilot that, whit respect to the mesomorphic, exhibits a higher static response and a closer frequency with the SWB.
The LTF Nyquist diagram of Figure 6.7 returns an unstable condition characterised by marked negative gain and phase margins. The PVS shows that a change in power lever input results in a nearly immediate change in thrust, which accelerates the tiltrotor exciting the SWB and, in turn, the pilot's biomechanis. The stable SWB couples with the pilot's biodynamics and becomes highly unstable. It can be observed that the trigger of the vertical bounce in tiltrotors results different from the one that verifies in helicopters, since there is no coupling between the collective lever's oscillations and the rotor coning mode, but an interaction between the oscillations of the PL induced by the involuntary pilot and the first bending mode of the wing.

In Ref.[14] the basic mechanism of the vertical bounce phenomenon in tiltrotors is discussed and it is proposed a simplified aeroelastic XV-15 model, able to capture the aircraft's heave motion and the low-frequency out-of-plane wing bending dynamics, represented in Figure 6.5(b). Specifically, exploiting the symmetry, the semi-wing is modelled by means of a bar of constant elastic properties, constrained to the plane of symmetry by a slider. The nacelles and the fuselage are represented by means of concentrated mass elements located at the tip and root of the semi-wing. Also the mass of

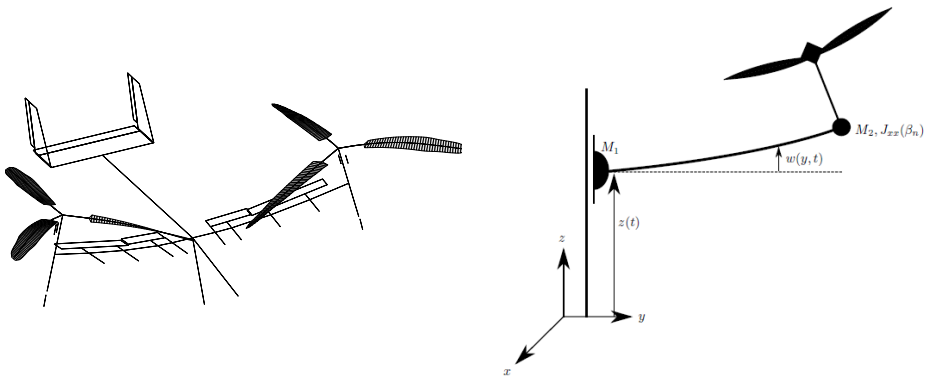

(a) MASST model (b) Simplified 3 DoF Model Ref.[14]

Figure 6.5: Comparison between models

the semi-wing is lumped into its edges. The aerodynamic participation is accounted by the rotor's contribution.
Since this simplified analytical model was derived in the intent of studying the XV-15 vertical bounce in hovering flight, the results obtained from this model are compared to the ones derived from the more detailed MASST model, presented up to here. Figure 6.5 compares the two models' set up.

Figure 6.8 compares the TFs of the vertical acceleration a_Z, measured at the pilot's seat, in response to the PL input obtained from the two models. In the proximity of the SWB frequency, the two TFs overlap with good approximation.
Pilot-in-the-Loop analysis, subsequently performed on both the detailed MASST and simplified models, returns the detection of the same vertical unstable oscillations. The root locus of Figure 6.9 shows the interaction between the airframe SWB mode and the poles associated with the pilot's BDFT, during hovering flight. It can be observed that results overlap with good approximation showing that the SWB roots become unstable when the vertical pilot's dynamics is included into the model. The SWB poles exhibit a high negative damping ratio which reaches a value of, approximately, -10%. As a result, a high resonance between the pilot's biomechanical pole and the aircraft poorly damped SWB is detected. However, it should be considered that the analysis is performed under few conservative hypothesis. The PVS is characterised by several uncertainties: the pilot/control device BDFTs, identified by Mayo (Ref.[12]), have been obtained on a flight simulator that differs from the XV-15 cockpit, with dissimilar control device dynamics. Moreover the friction, that can derive from gearings, mechanical transmissions, etc. is not modelled. Avoiding the introduction of friction makes the system more prone to PAOs. It is in fact true that the XV-15 was not affected by pilot biomechanical coupling because it used mechanic control linkages. Anyhow it can be stated that in modern tiltrotors mechanical chain transmissions are substituted by fly-by-wire systems, that dramatically reduce the friction contribution. As a result, this analysis may not be fully representative of the XV-15 vertical dynamics, but it can potentially emphasise issues associated with modern tiltrotors' design.

In the simplified analytical model the pilot is only acting over the collective control input through the PL because the dynamics associated with the engine, the drive train and RPM "Beta" governor are not included into the model. In MASST the pilot, coherently with the block scheme of Figure 6.2, is acting on both the collective θ_0 and throttle θ_t inputs. Figure 6.10 com-

pares two MASST models, with and without the set of **E**ngine, **D**rive **T**rain and RPM **G**overnor, that is hereafter recalled by the acronym **EDTG**. It can be observed that the introduction of the EDTG assembly results highly negligible in the frequency range of interest. This demonstrates that the simplified analytical model can be adopted to reliably represent the XV-15 vertical dynamics in hover.

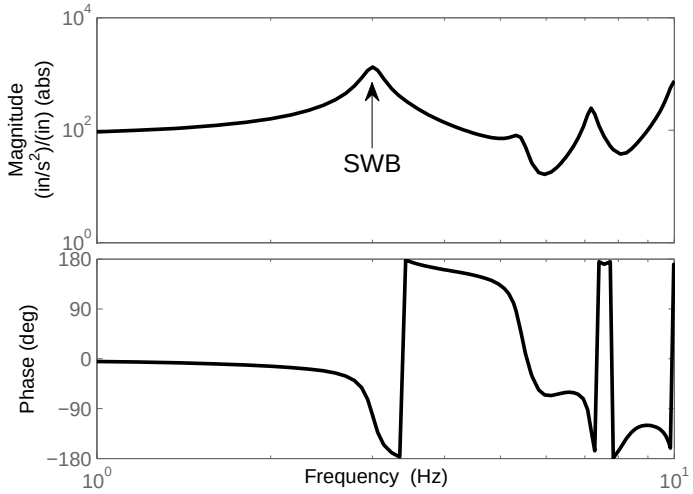

Figure 6.6: XV-15 transfer function from δ_Z [in] to a_Z [in/s^2] in Hover (NAC90, airspeed 0 knots)

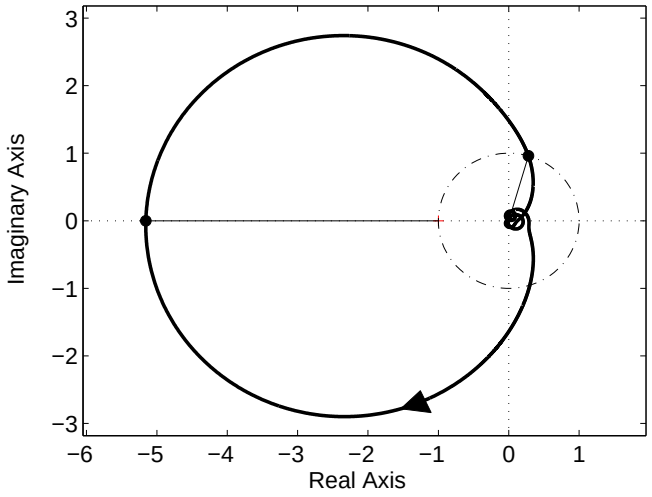

Figure 6.7: LTF Nyquist Diagram in Hover (NAC90, airspeed 0 knots)

	$\mathbf{G_m}$ [dB]	f [Hz]
0 kn	-14.2	3.01
	$\mathbf{P_m}$ [deg]	f [Hz]
0 kn	-106	3.50

Table 6.2: Hover Gain Margins

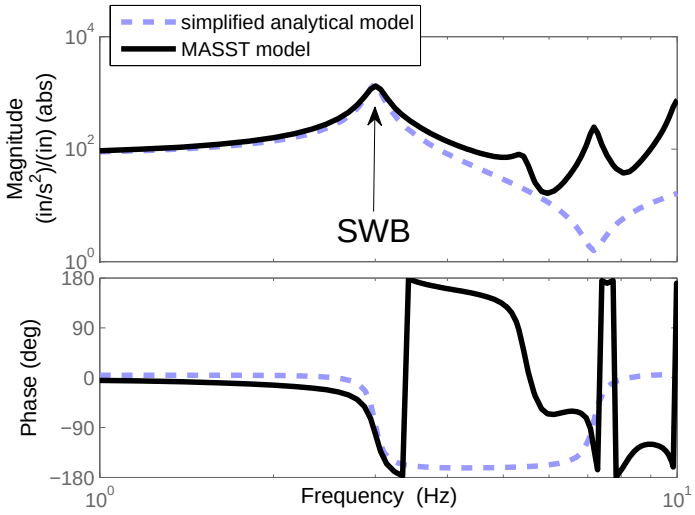

Figure 6.8: Simplified model vs. MASST model: XV-15 TFs from δ_Z [in] to a_Z [in/s^2] in Hover (NAC90, airspeed 0 knots)

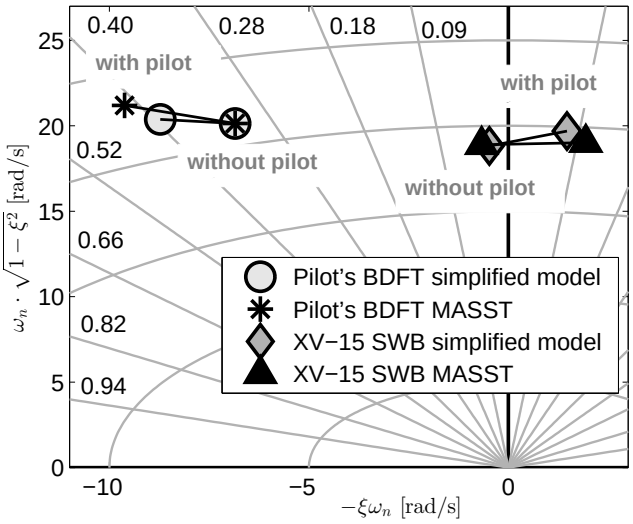

Figure 6.9: Simplified model vs. MASST model: root Locus in Hover (NAC90, airspeed 0 knots)

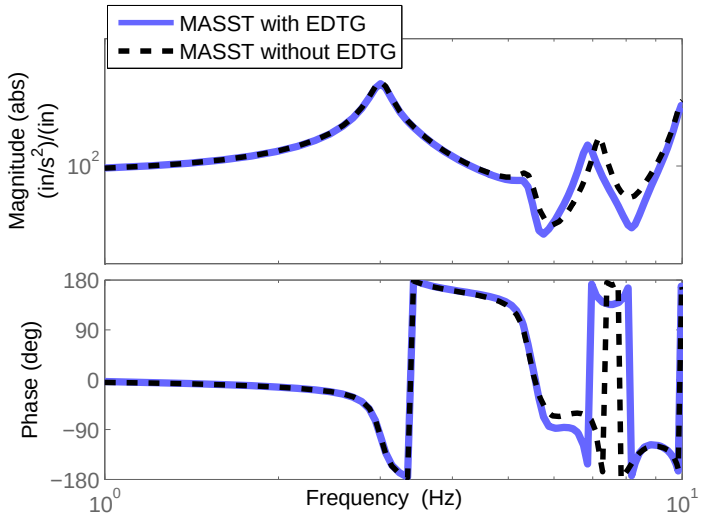

Figure 6.10: MASST XV-15 TFs from δ_Z [in] to a_Z [in/s^2] with and without EDTG assembly in Hover (NAC90, airspeed 0 knots)

6.2.2 Extended PAO Analysis

In Section 6.2.1 the basic mechanism of the vertical bounce in tiltrotors in hovering flight is discussed. In the present Section the analysis of the phenomenon is extended to other flight conditions described by the tiltrotor's conversion corridor. It is selected a reduced and representative subset of configurations, parameterised with respect to the NAC angle and the airspeed. For each nacelle angle the minimum, the maximum and a mid velocity are analysed. The flight height is maintained at Sea Level (SL) for every selected condition.

Since the collective gear ratio $\widetilde{G}_0$, shown in Figure 6.3, is decreasing with the NAC angle, the vertical bounce phenomenon is expected to become less severe as the conversion is completed. Moreover, the aerodynamic loads, due to non-zero forward speed, can potentially exalt the vertical accelerations, and can consequently magnify the vehicle response after a PL input. As a result, combining these two aspects, the most critical conditions are expected to be encountered in the region of the conversion corridor that is concurrently characterised by high NAC angles (close to HEMODE) and maximum airspeeds.
The results obtained after Pilot-in-the-Loop analyses are exposed in the following. Again, it is specified that the closed loop feedback is conservatively provided by Mayo's ectomorphic pilot that, whit respect to the mesomorphic, exhibits a higher static response and a closer frequency with the SWB. The influence of possible time delays τ, introduced by the control device, is neglected.

The natural frequencies $\omega_n\,[Hz]$ and the damping ratios $\xi[\%]$ of the complex-conjugate SWB poles, obtained as a function of the airspeed and the NAC angle, are represented in Figure 6.11. It can be observed that the vertical bounce frequency shows a small oscillation in magnitude that ranges from 3 Hz to 3.15 Hz. A more appreciable variation is instead exhibited by the damping ratio. Figure 6.12 shows the superposition of the damping ratio level curves on the conversion corridor, whose analysed conditions are marked with a circle. As expected, the most critical configurations are detected in the upper region of the conversion corridor. The most crucial points correspond to NAC 75-140 kn and NAC 90-120 kn.

Though the negative damping ratio is lowering in magnitude with the NAC angle, it can be observed that the vertical instability is still present in AP-

MODE. In APMODE, the SWB couples with the pilot's biodynamic response through a mechanism that is different from the one detected in Section 6.2.1 in HEMODE. In this last case the direct effect of a change in collective input results is a nearly immediate change in thrust, which accelerates the tiltrotor exciting the SWB and, in turn, the pilot's biomechanics (Ref.[14]). In APMODE the thrust vector lays in the plane of the wing, and, consequently, it can not be considered responsible for the excitation of the out-of-plane SWB. It is subsequently speculated that the source of the excitation could be brought back to the torque generated by the rotors after a throttle input through the power lever. As depicted in Figure 6.13, due to the fact that the rotors are counter rotating, the wing is supposed to be symmetrically forced by the rotors' torque. In order to validate this hypothesis, Figure 6.14 compares the damping ratio of the SWB poles obtained after the analysis of three different configurations :

1. the nominal set up, that takes into account the presence of the rotors' torque and the pilot's BDFT.
2. a configuration that includes the pilot's BDFT and that is not considering the rotors' torque.
3. a configuration that includes the rotors' torque and that is not considering the pilot's BDFT.

It can be observed that the SWB pole becomes stable when the torque produced by the rotors is neglected. As a result, the APMODE instability can be justified as follows: the effect of a change in power lever input results in a change in the torque produced by the rotors which accelerates the tiltrotor exciting the SWB mode and, in turn, the pilots' biomechanics.

Robust analysis, performed on the overall conversion corridor, returns unstable conditions characterised by negative gain and phase margins, as shown in Figure 6.15. The most robust instabilities correspond to the higher nacelle angles.

In summary, results in the present Section highlight the proneness of the XV-15 tiltrotor to vertical bounce phenomenon, which is caused by pulsating thrust induced by an oscillation of the power lever inadvertently introduced by the pilot. The most critical conditions are encountered in the upper region of the conversion corridor, characterised by elevated NAC angles. Specifically, the most crucial configurations are represented by NAC 75-140 kn and NAC 90-120 kn. The instability detected in APMODE can be described as a coupling between the SWB mode and the pilot' biomechanics due to a pulsating torque. This pulsating torque is induced by the

rotors, after an oscillation of the power lever that is caused by the involuntary response of the pilot to the vertical vibrations of the cockpit. Finally, for intermediate conversion configurations the effects induced by the rotor's thrust and torque are mixed.

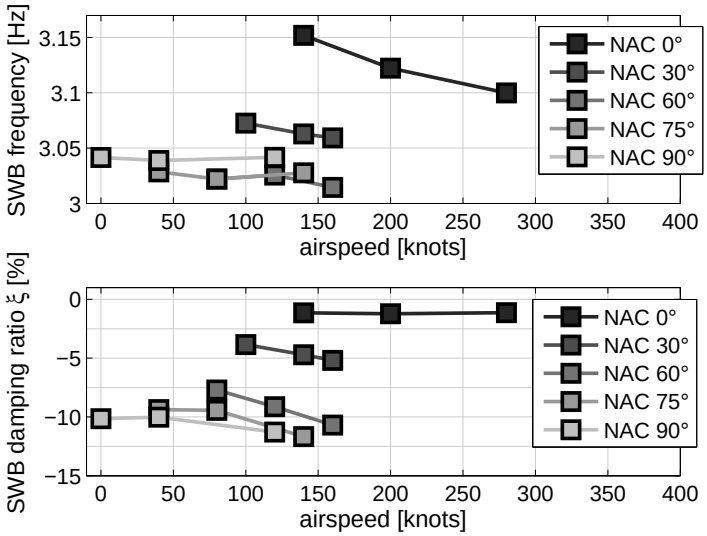

Figure 6.11: SWB frequency and damping on the overall conversion corridor

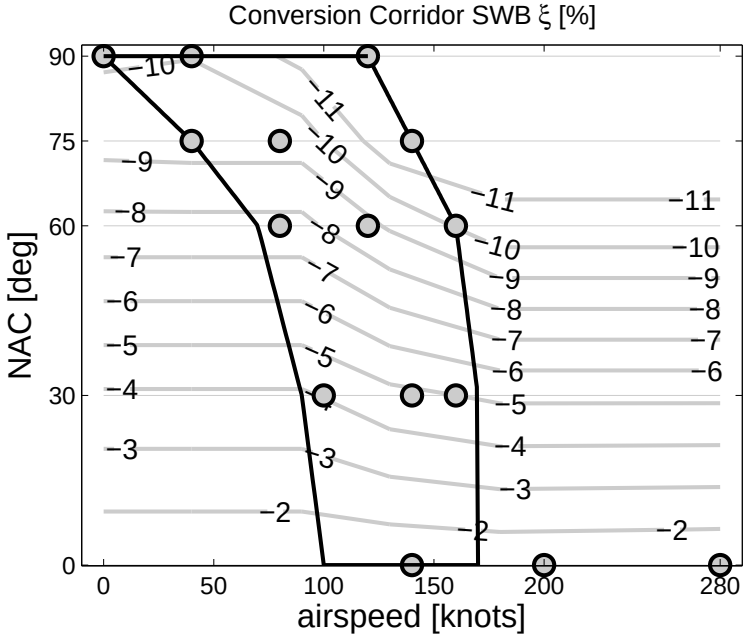

Figure 6.12: SWB damping on the overall conversion corridor

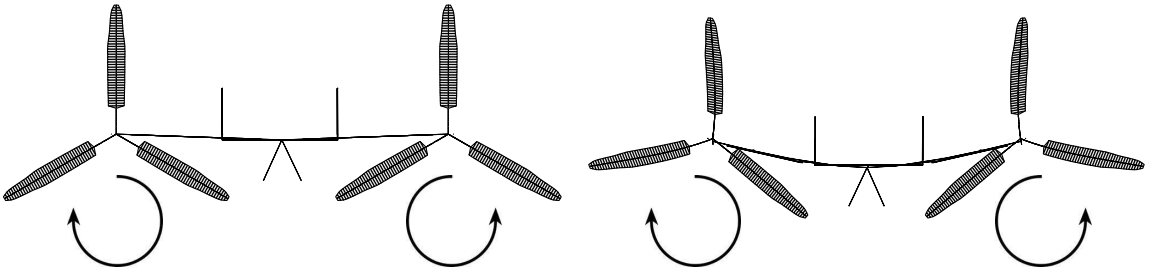

Figure 6.13: APMODE SWB excitation

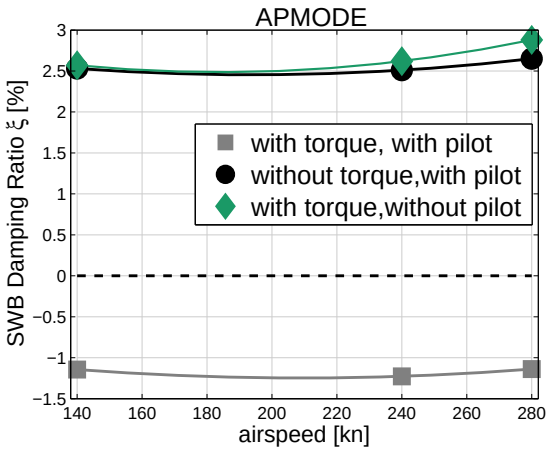

Figure 6.14: Torque effect over APMODE SWB damping

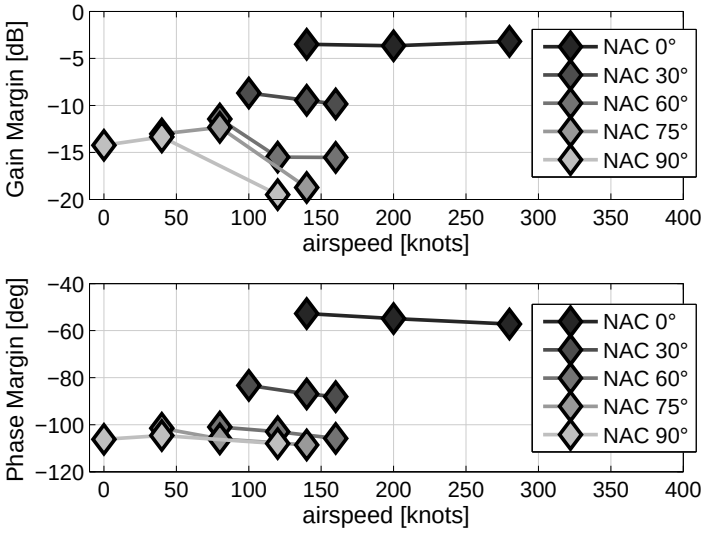

Figure 6.15: Stability Margins on the overall conversion corridor

6.2.3 Sensitivity Analysis

Sensitivity Analysis - EDTG Dynamics

In this Section it is processed a sensitivity analysis of the vertical PAO with respect to the introduction of the EDTG assembly. The engine, the drive train and the RPM governor are removed from the MASST model and the rotor-speed is assumed constant. The analyses are performed for a subset of representative configurations of the conversion corridor. Figure 6.16 compares the SWB damping ratio obtained with and without the EDTG dynamics; no net difference is shown in the upper region of the conversion corridor, that remains almost unaltered. This outcome confirms the results of Section 6.2.1, that have demonstrated the low influence of the EDTG dynamics over the PAO prediction in hovering flight (Fig.6.10). The more appreciable effect is instead observable in the lower region of the conversion corridor, especially in APMODE configuration. When the EDTG dynamics are included (Figure 6.16(a)) the APMODE SWB is destabilised by the pulsating torque introduced by the rotors after an oscillation of the power lever (Section 6.2.2). On the contrary, when the EDTG dynamics are removed (Fig.6.16(b)), the APMODE SWB is stable. Let us consider the vertical tiltrotor's dynamics reported in the block scheme of Figure 6.2. When the EDTG dynamics are neglected, the gear ratio $\widetilde{G}_t$ is set to zero. Moreover, in APMODE flight the gear ratio $\widetilde{G}_0$ is null (Fig.6.3). As a result both $\widetilde{G}_t$ and $\widetilde{G}_0$ are null and the APMODE vertical tiltrotor's dynamics can not be excited by the pilot's power lever input δ_Z^{PP}. The complex-conjugate APMODE SWB poles can not be affected by the destabilising biodynamic feedback and remain stable.

Figures 6.17 and 6.18 report the stability margins derived from robust analysis. Again it can be observed that the exclusion of the EDTG dynamics is not altering the robustness of the results obtained in the upper region of the conversion corridor.

Sensitivity Analysis - Pilot's BDFT

The most critical configurations are individuated for NAC90 and NAC75 and the associated maximum airspeeds; for completeness, the stability analysis held by these nacelle angles are repeated considering the mesomorphic pilot's feedback. The results are shown is Figures 6.19 and 6.20; it can be observed that the ectomorphic feedback generates a more critical instability with respect to the mesomorphic, though, in both cases, the vertical bounce results very marked and robust. This is justified by the fact that the ectomorphic pilot (Fig. 6.4) shows a higher static response and a resonance peak that is closer to the SWB mode frequency.

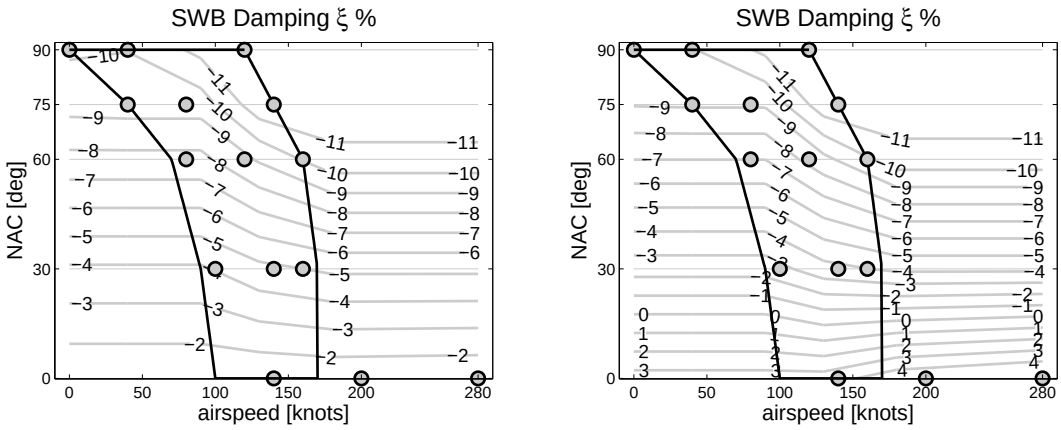

Figure 6.16: Damping ratio with (left) and without (right) EDTG Dynamics

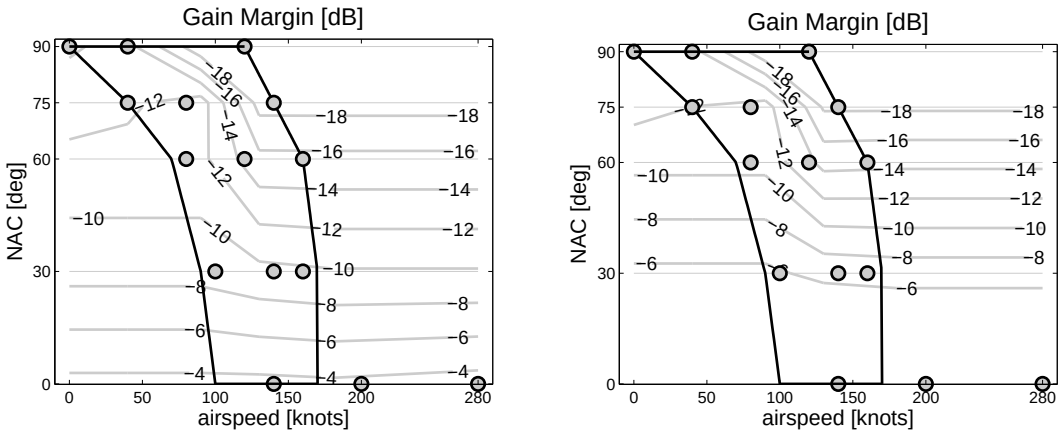

Figure 6.17: Gain Margin with (left) and without (right) EDTG Dynamics

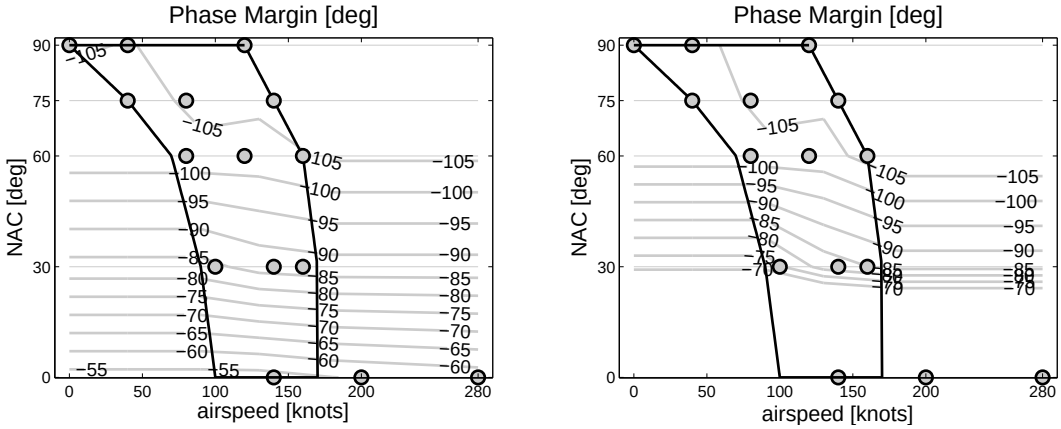

Figure 6.18: Phase Margin with (left) and without (right) EDTG Dynamics

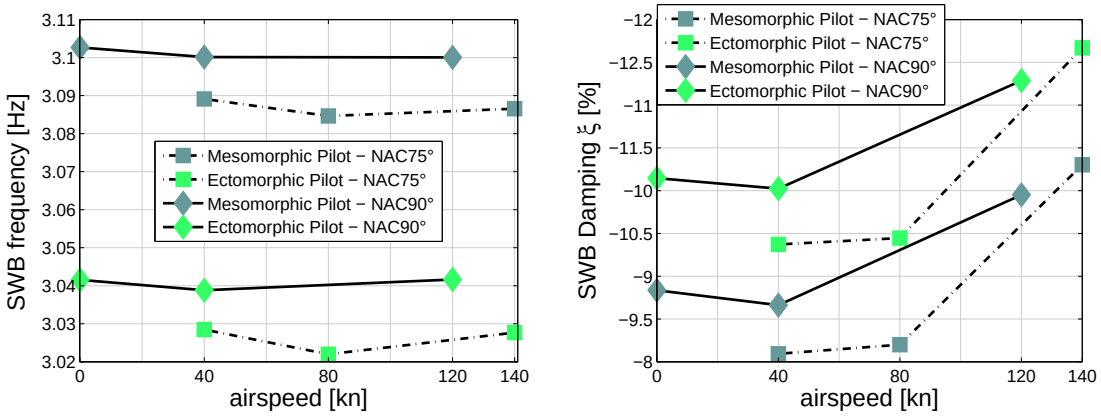

Figure 6.19: SWB pole natural frequency and damping ratio with respect to airspeed [knots], NAC angle [deg] and pilot's BDFT

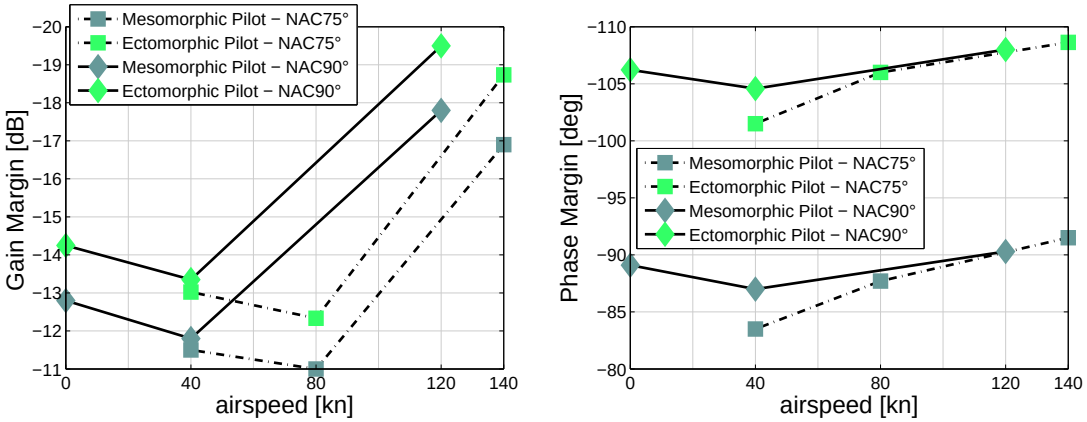

Figure 6.20: Stability Margins with respect to airspeed [knots], NAC angle [deg] and pilot's BDFT

6.2.4 Means of Prevention - Notch Filter

The trigger of the vertical bounce instability, discussed in this Chapter, is rooted in the coupling of the first symmetric bending mode of the wing and the biodynamic pole of the pilot's arm, holding the power lever inceptor. Among the many possible means of prevention, the design of a notch filter is herein proposed in order to eliminate the instability.

Notch filters (NFs) can suppress the resonance peaks of the undesired modes. The structure of a NF, characterised by a second-order transfer function, is reported in Equation 6.3. The relations that link the coefficients c_1, c_2, c_3 and c_4 with the features of the NF are reported in Equations 6.4 and 6.5 (see Ref.[42]). The NF is designed to stabilise the SWB pole and to obtain a robust PVS with a gain margin above 6 decibel and a minimum phase margin of 60 degrees.
A NF attenuates signals within a very narrow band of frequencies; due to the fact that the SWB frequency shows little variations for all the configurations of the conversion corridor (Figure 6.11), it is possible to design a single NF in order to suppress the vertical bounce in a wide range of flight conditions. The set of parameters that have been selected to characterise the NF are reported in Table 6.3.

$$H_{NF}(s) = \frac{1 + c_1 \cdot s + c_2 \cdot s^2}{1 + c_3 \cdot s + c_4 \cdot s^2} \tag{6.3}$$

$$\omega_{NF} = \frac{1}{\sqrt{c_2}} \qquad \mu = 20log\Big(\frac{c_1}{c_3}\Big) \tag{6.4}$$

$$Q = \frac{\sqrt{c_4}}{c_3} \qquad \mu_\infty = \frac{c_2}{c_4} \tag{6.5}$$

$\omega_{NF}\,[Hz]$	μ	Q	μ_∞
2.96	1	1.3158	-50

Table 6.3: Notch Filter (NF) parameters

The validation of the effectiveness of the designed NF is shown in Figures 6.21 and 6.22. The NF successfully suppresses the instability associated with the most critical scenarios detected by the analysis of Section 6.2.2.

One of the main issues associated with NF implementation is the fact that they introduce phase delays, that may act in the low-frequency domain.

The designed NF introduces a phase delay at 1 Hz that ranges from 15 to 20 degrees, depending on the configuration of the conversion corridor that is taken into account. As a consequence, detailed analysis should consider the impact the NF on the handling qualities of the aircraft.

The designed NF is also applied to the simplified XV-15 model, presented in Section 6.2.1. It is recalled that this model is able to capture the aircraft's heave motion and the low frequency out of plane bending dynamics for a nacelle angle of 90 degrees and null forward flight, i.e. hovering flight. Figure 6.23 shows that the robust stability requirements are satisfied when the designed NF is applied to the analytical simplified model.
The fact that the same NF can successfully suppress the instability of both the detailed MASST and the simplified XV-15 models suggests the possibility to use the latter to further validate the NF design. In fact, the simplified analytical model is characterised by lumped parameters and it can be easily modified to represent a wide variety of operative conditions and gross weight (11.000 lb $<$ M$_T$ $<$ 15.000 lb) configurations. As a result, it is theoretically possible to validate the effectiveness of the NF over a set of critical scenarios involving the XV-15 HEMODE hovering flight, that corresponds to one of the most critical configurations detected by the vertical bounce analysis conducted in Section 6.2.2.

In conclusion, the proposed means of prevention is able to restore the stability and robustness of the system, although the disadvantages associated with phase delay should be given consideration. However, the notch filter represents a simple tool to prevent the vertical bounce and can be easily implemented in aircraft with fly-by-wire control systems. The designed NF successfully suppresses the instability in all critical conditions of the conversion corridor and the simplified analytical model should be given consideration for the preliminary design of the flight control system.

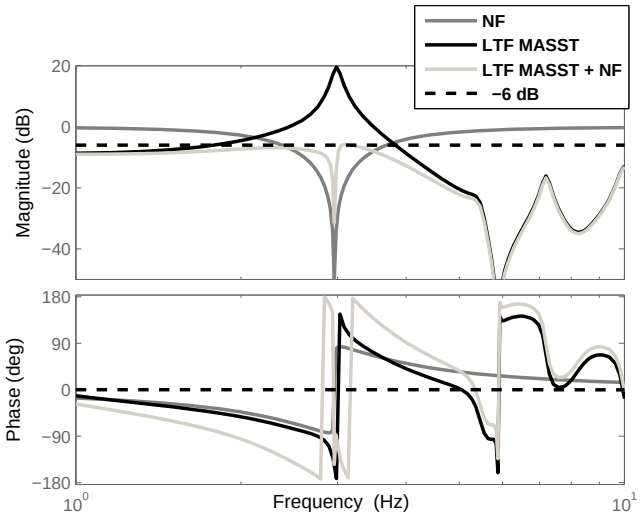

(a) NAC 90, airspeed 120 knots

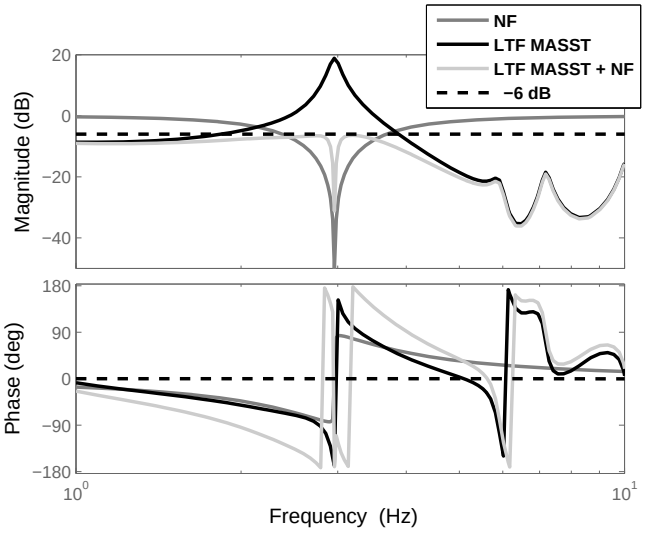

(b) NAC 75, airspeed 140 knots

Figure 6.21: Notch Filter Validation

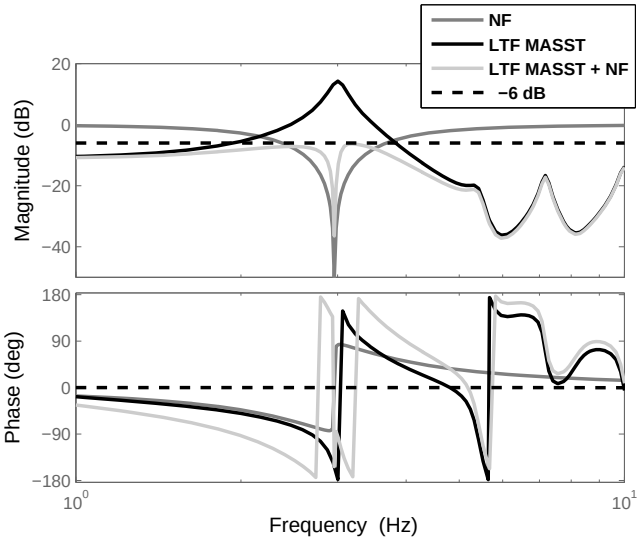

(a) NAC 90, airspeed 0 knots

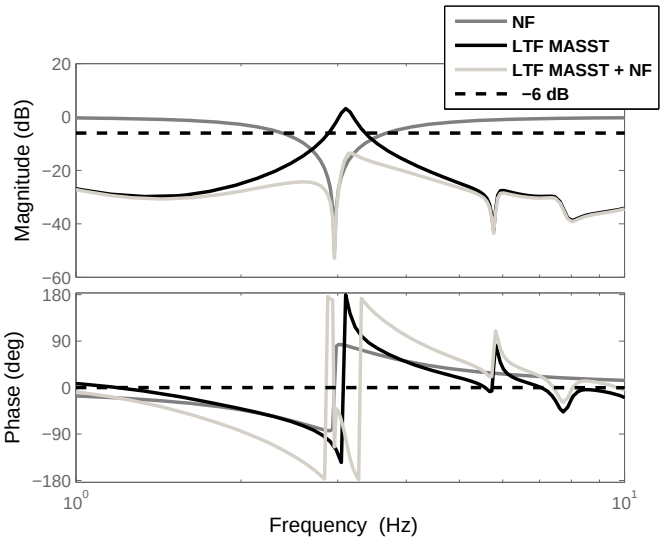

(b) NAC 0, airspeed 280 knots

Figure 6.22: Notch Filter Validation

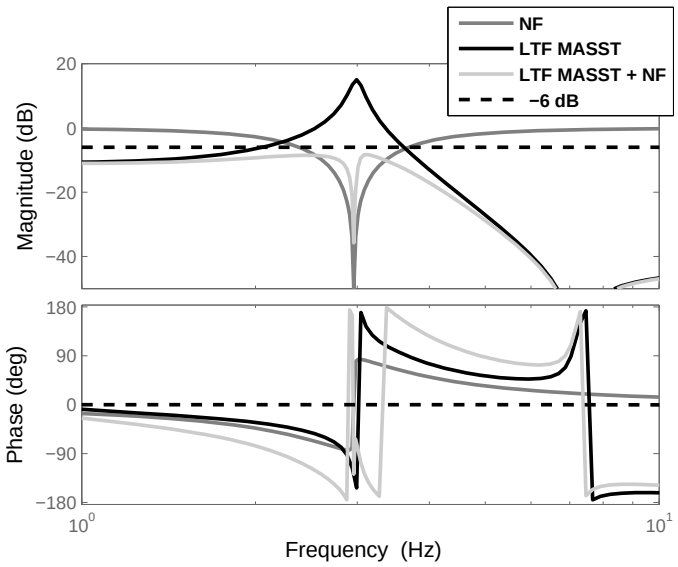

Figure 6.23: Notch filter validation over the simplified analytical model (NAC 90, airspeed 0 knots)

Chapter 7

Conclusions

A detailed aeroelastic model, representative of the Bell XV-15, has been developed to analyse PAO phenomena in tiltrotor aircraft. The tiltrotor's structural airframe, outlined as a stick model, enables the description of the six lowest normal modes of the wing. These modes allow the characterisation of the aircraft's dynamics in the PAO characteristic frequency range, between 2 and 8 Hz.

Lateral instability mechanisms, due to involuntary pilot's lateral cyclic stick motion, are investigated first. The conducted analyses demonstrate that, in nominal conditions, the eventuality for a lateral rotorcraft-pilot-coupling to occur is low. Considerable losses of stability margins are contemplated only when the pilot's biodynamic feedthrough is characterised by the most unfavourable biomechanical properties identified in Ref.[34], and when possible control device time delays are introduced.
However, a critical parameter for the occurrence of a lateral PAO is detected in the geometry of the vertical stabilisers. It is demonstrated that the lateral instability mechanism can be favoured if the vertical fins are located in a region settled above the plane of the wing. It is subsequently recommended to distribute part of the vertical aerodynamic surface below the plane of the wing, in order to compensate the interactional effect induced by the wing's vorticity, due to an asymmetric deflection of the flaperons. As a matter of fact the XV-15 nominal tail geometry guarantees the lateral stability, since a large fraction of the vertical stabilisers is located below the plane of the wing ($\approx 30\%$). In the case of the V-22 the area distributed below the plane of the wing was probably insufficient to counteract the instability mechanism reported in Ref.[11]. It is finally speculated that the described lateral unstable oscillations may occur in the AW609, which is characterised by a single vertical stabiliser positioned at midspan above the plane of the wing.

Possible instability mechanisms on the longitudinal axis are subsequently investigated. Due to the frequency separation between the pilot's biodynamic pole (∼4Hz) and the symmetric wing chord mode frequency (∼6Hz), the possibility for an unstable RPC to occur is low. Moreover, differently from the V-22, the XV-15, as well as the AW609, mounts a power lever, that inhibits the transmissibility between the longitudinal accelerations at the pilot's seat and the unintentional longitudinal response of the pilot's upper limbs.
In summary, thanks to an adequate decoupling between the longitudinal pilot's dynamics and the airframe symmetric elastic modes and thanks to the specific cockpit configuration, that presents a power lever in substitution of a thrust command lever, the XV-15 is demonstrated not to be prone to longitudinal PAOs.

Finally, possible vertical instability mechanisms are explored on the overall conversion corridor. The most critical flight configurations are encountered in the upper region of the conversion corridor, where a high resonance between the pilot's biomechanical pole and the poorly damped symmetric wing bending mode is detected. In helicopter mode the vertical unstable oscillations are excited by a pulsating thrust, that results from the oscillatory motion of the power lever in response to the vertical accelerations of the cockpit. It is also detected an instability mechanism in airplane mode, which is due to a pulsating torque produced by the rotors after involuntary oscillations of the power lever, as a consequence of the vertical accelerations measured at the pilot's seat.
It is recalled that the high instabilities detected in this section undergo few conservative hypothesis, including the absence of the friction modelling.
In conclusion, in order to suppress the vertical PAOs, the design of a notch filter is proposed. It represents a simple tool to prevent the vertical bounce and it can be easily implemented in aircraft with fly-by-wire systems, although the disadvantages associated with phase delay should be considered.

7.1 Future Developments

The closed loop pilot-vehicle system has been characterised by a Primary Flight Control System and a governor controller that maintains a constant rotor speed. Today it is agreed that incidents caused by airplane/rotorcraft-pilot-coupling are often associated with the aircraft's control system. A future development will consider the possibility to introduce into the model an

Automatic Flight Control System, which is used to improve the tiltrotor's stability and handling qualities.

In this thesis, only category I Rotocraft Pilot Couplings (Ref.[8]) are analysed, i.e. phenomena that do not imply a significant effect of nonlinearities (e.g. actuator saturations, freeplays, etc...). It can not be excluded that, for large amplitude oscillations, the nonlinearities may have an impact; this aspect may be considered as an hint for possible future work.
One of the main limitations of the present research is also related to the proposed pilot model. Currently PAO analyses are performed separately along the longitudinal, lateral and vertical axes, due to the impossibility to handle a single pilot model representative of the complete biodynamics over the three axes. Along each axis the pilot's dynamics is identified by a linear transfer function. A future work will consider the possibility to introduce a more detailed biomechanical scheme, able to properly reproduce the relationship between the cockpit motion and the involuntary pilot's contribution in the aircraft's control inputs. This challenging objective can be potentially accomplished following different approaches.
One option is represented by an experimental characterisation of the biodynamic properties of the pilot. A vibrating flight simulator cockpit may be used to excite the human body along the longitudinal, lateral and vertical axes. For each axis the motion of the cockpit controls, in response to a single linear acceleration, can be recorded to characterise a biodynamic matrix that contains the transfer functions between the accelerations, measured at the pilot's seat, and the control device deflections. This method enables a comprehensive description of the involuntary pilot, allowing an estimation of the cross coupled effects. Pilot-in-the-loop stability analyses can be performed using MIMO criteria (Ref.[45]). However, one of the main issues associated with the experimental approach is related to the large variability of the biodynamic feedthrough (e.g. pilot's anthropometric characteristics, muscular activation dynamics, control device dynamics, etc.) that prevent a unique identification of the pilot.
An alternative option may be represented by a numerical approach. The pilot's involuntary participation can be estimated using detailed multibody models of the pilot's upper limbs (Ref.[43]). In this case the pilot's BDFTs can be characterised by means of a linearisation procedure performed with respect to a reference condition. One of the main advantages associated with this approach is that linear models can be produced for arbitrary cockpit configurations, without the need to perform dedicated tests (Ref.[44]).

Finally, the actual pilot model, descriptive of the involuntary biodynamic feedthrough, may be extended to describe the voluntary pilot's dynamics. A comprehensive characterisation of the pilot will enable the possibility to conduct general rotorcraft-pilot-coupling analyses, also including the study of pilot-induced-oscillation (PIO) phenomena, that result from the active participation of the pilot.

Bibliography

[1] Martin D. Maisel, Demo J. Giulianetti and Daniel C. Dugan,"The History of the XV-15 Tilt Rotor Research Aircraft: From Concept to Flight", NASA/SP-2000-4517, NAS 1.2l:4517, Jan 01, 2000.

[2] Jackson A.J.,"British Civil Aircraft since 1919", Volume 1., Putnam, ISBN 0-370-10006-9, 1974

[3] Steve Coates, Jean-Christophe Carbonel,"Helicopters of the Third Reich, Crowborough", UK, Classic Publications Ltd., 2002, ISBN 1-903223-24-5.

[4] Deckert, W. H.; Ferry, R. G. "Limited Flight Evaluation of the XV -3 Aircraft", AFFTC-TR-6O-I1-, Air Res. and Dev. Command, U.S. Air Force, May I96O.

[5] Maisel, M. D., et al. "NASA/Army XV-15 Tilt-Rotor Research Aircraft Familiarization Document", TM X-62,407, NASA, January 1975.

[6] Steve Markman, Bill Holder, Bell/Boeing V-22 Osprey Tilt-Engine VTOL Transport (U.S.A.), "Straight Up: A History of Vertical Flight", Atglen, Pennsylvania, Schiffer Publishing, 2000.

[7] Marilena D. Pavel, Michael Jump, Binh Dang-Vu, Pierangelo Masarati, Massimo Gennaretti, Achim Ionita, Larisa Zaichik, Hafid Smaili, Giuseppe Quaranta, Deniz Yilmaz, Michael Jones, Jacopo Serafini, Jacek Malecki,"Adverse rotorcraft pilot couplingsPast, present and future challenges", Progress in Aerospace Sciences, Volume 62, 2013, Pages 1-51, ISSN 0376-0421.

[8] Dieterich O., Götz J., DangVu B., Haverdings H., Masarati P., Pavel M. D., Jump M., and Gennaretti, M., "Adverse Rotorcraft-Pilot Coupling: Recent Research Activities in Europe", 34th European Rotorcraft Forum, September 16-19 2008.

[9] Masarati P., Quaranta G., Lu L., and Jump M., "A Closed Loop Experiment of Collective Bounce Aeroelastic Rotorcraft-Pilot Coupling", Journal of Sound and Vibration, Vol. 333, (1), doi:10.1016/j.jsv.2013.09.020, January 2014, pp. 307-325.

[10] National Transportation Safety Board Aviation Accident Final Report, Accident Number DCA16FA199, Registration N525TA

[11] Parham T. Jr., Popelka D., Miller D. G., and Froebel A. T.,"V-22 Pilot-in-the-Loop Aeroelastic Stability Analysis", American Helicopter Society 47th Annual Forum, May 68 1991.

[12] Mayo J. R. "The Involuntary Participation of a Human Pilot in a Helicopter Collective Control Loop", 15th European Rotorcraft Forum, 12-15 September 1989.

[13] Masarati P., Muscarello V., and Quaranta G. "Linearized Aeroservoelastic Analysis of Rotary-Wing Aircraft" 36th European Rotorcraft Forum, September 7-9 2010.

[14] Muscarello V., Masarati P., and Quaranta G.,"Collective Bounce Problems in Tiltrotors", 42nd European Rotorcraft Forum, Paper no. 121, September 5-8 2016.

[15] C.W. Acree Jr., R. J. Peyran, Wayne Johnson "Rotor Design for Whirl Flutter: An Examination of Options for Improving Tiltrotor Aeroelastic Stability Margins", American Helicopter Society 55th Annual Forum, May 25-27 1999.

[16] Pierangelo Masarati, Vincenzo Muscarello and Giuseppe Quaranta, "MASST Manual", V. 2.1, November 5, 2012.

[17] Pierangelo Masarati, Vincenzo Muscarello, Giuseppe Quaranta, Alessandro Locatelli, Daniele Mangone, Luca Riviello and Luca Viganò, "An Integrated Environment For Helicopter Aeroservoelastic Analysis: The Ground Resonance Case", 37th European Rotorcraft Forum, September 13-15 2011.

[18] Karpel M. and Raveh D.,"Fictitious Mass Element in Structural Dynamics", AIAA Journal, Vol. 34, (3), 1996, pp. 607613.

[19] C. W. Acree and Mark B. Tischler,"Identification of XV-15 aeroelastic modes using frequency sweeps", Journal of Aircraft, Vol. 26, No. 7 (1989), pp. 667-674.

[20] L. Cavagna, A. Da Ronch, S. Ricci,"NeoCASS Next generation Conceptual Aero Structural Sizing", Dipartimento di Ingegneria Aerospaziale - Politecnico di Milano, February 7, 2009

[21] Albano E., Rodden W. P.,"A Doublet-Lattice Method for Calculating Lift Distributions on Oscillating Surfaces in Subsonic Flows", AIAA Journal, Vol. 7, No. 2 (1969), pp. 279-285

[22] Joseba Murua, Rafael Palacios, J. Michael R. Graham,"Applications of the unsteady vortex-lattice method in aircraft aeroelasticity and flight dynamics", Progress in Aerospace Sciences Journal, Volume 55, 2012, Pages 46-72, ISSN 0376-0421

[23] MSC/NASTRAN Version 68 aeroelastic analysis user's manual, Technical report, DOC9182, MSC, 2016.

[24] Roger K. L.,"Airplane Math Modeling Methods for Active Control Design", AGARD Structural Aspects of Active Controls, CP-228, AGARD, Aug. 1977, pp. 4.1-4.11

[25] Morino L., Mastroddi F., De Troia F., Ghiringhelli G. and Mantegazza P. ,"Matrix fraction approach for finite state aerodynamic modelling", AIAA Journal, vol. 33, no. 4, pp. 703-711, 1995.

[26] Acree C. W. Jr.,"An Improved CAMRAD Model for Aeroelastic Stability Analysis of the XV-15 With Advanced Technology Blades", NASA-TM-4448, A-92022, NAS 1.15:4448, Mar 01, 1993

[27] Masarati P., Muscarello V., and Quaranta G.,"Linearized Aeroservoelastic Analysis of Rotary-Wing Aircraft", 36th European Rotorcraft Forum, September 7-9 2010.

[28] "CAMRAD II: Comprehensive Analytical Model of Rotorcraft Aerodynamics and Dynamics", Technical report, Johnson Aeronautics, 1988.

[29] Tony Burton, Nick Jenkins, David Sharpe, Ervin Bossanyi,"Wind Energy Handbook", Wiley, ISBN: 978-0-470-69975-1, June 2011.

[30] Pitt D. M. and Peters D. A.,"Theoretical Prediction of Dynamic-Inflow Derivatives", Vertica, Vol. 5, (1), 1981, pp. 2134

[31] J.M. Schaeffer, R. Alwang, Boeing Helicopters, M. Joglekar, Bell Helicopter Textron, Inc.,"V-22 Thrust Power Management Control Law Development", AHS Forum 47, May 6, 1991.

[32] Ferguson S. W.,"A Mathematical Model for Real Time Flight Simulation of a Generic Tilt-Rotor Aircraft", CR 166536, NASA, 1988.

[33] Merritt H. E.,"Hydraulic Control Systems", John Wiley & Sons, New York, 1967.

[34] Muscarello V., Quaranta G., Masarati, P. Lu L., Jones M. and Jump M.,"Prediction and Simulator Verification of Roll/Lateral Adverse Aeroservoelastic Rotorcraft-Pilot Couplings", Journal of Guidance, Control, and Dynamics, doi:10.2514/1.G001121, in press.

[35] Paolo Rocco, ,"Controlli automatici, Ingegneria Aerospaziale", 2013

[36] Skogestad S. and Postlethwaite I.,"Multivariable Feedback Control", John Wiley & Sons,Chichester, 2005.

[37] United States Patent,"Tilt actuation for a rotorcraft", US 7871033 B2, Jan. 18, 2011.

[38] Parham T. Jr. and Corso L. M.,"Aeroelastic and Aeroservoelastic Stability of the BA 609", 25th European Rotorcraft Forum, September 1416 1999.

[39] Giorgio Guglieri, Carlo E.D. Riboldi,"Introduction to Flight Dynamics", Celid, EAN: 9788867890422.

[40] Relazione di Inchiesta - Incidente occorso all'aeromobile AugustaWestland AW609 marche N609AG, in località Tronzano Vercellese, 30 ottobre 2015, ANSV Agenzia Nazionale per la Sicurezza del Volo

[41] L. Quartapelle, F. Auteri,"Fluidodinamica Incomprimibile", CEA, EAN: 9788808185396, 2013

[42] Battipede M., Gili P., Carano L., and Vaccaro V.,"Constrained Notch Filter Optimization for a Fly-By-Wire Flight Control System", l'Aerotecnica Missili e Spazio, Vol. 88, No. 3, 2009, pp. 105113

[43] Pierangelo Masarati, Giuseppe Quaranta, Andrea Zanoni,"A Detailed Biomechanical Pilot Model for Multi-Axis Involuntary Rotorcraft-Pilot Couplings", 41st European Rotorcraft Forum, September 2015

[44] Pierangelo Masarati, Giampiero Bindolino, Giuseppe Quaranta,"A Parametric Pilot/Control Device Model for Rotorcraft Biodynamic Feedthrough Analysis", 40th European Rotorcraft Forum, September 2014

[45] Desoer C. and Wang Y.T.,"On the generalized Nyquist stability criterion", IEEE Transactions on Automatic Control, Vol. 25 num. 2, pages 187–196, IEEE, 1980

Appendix A

XV-15 Cockpit Layout

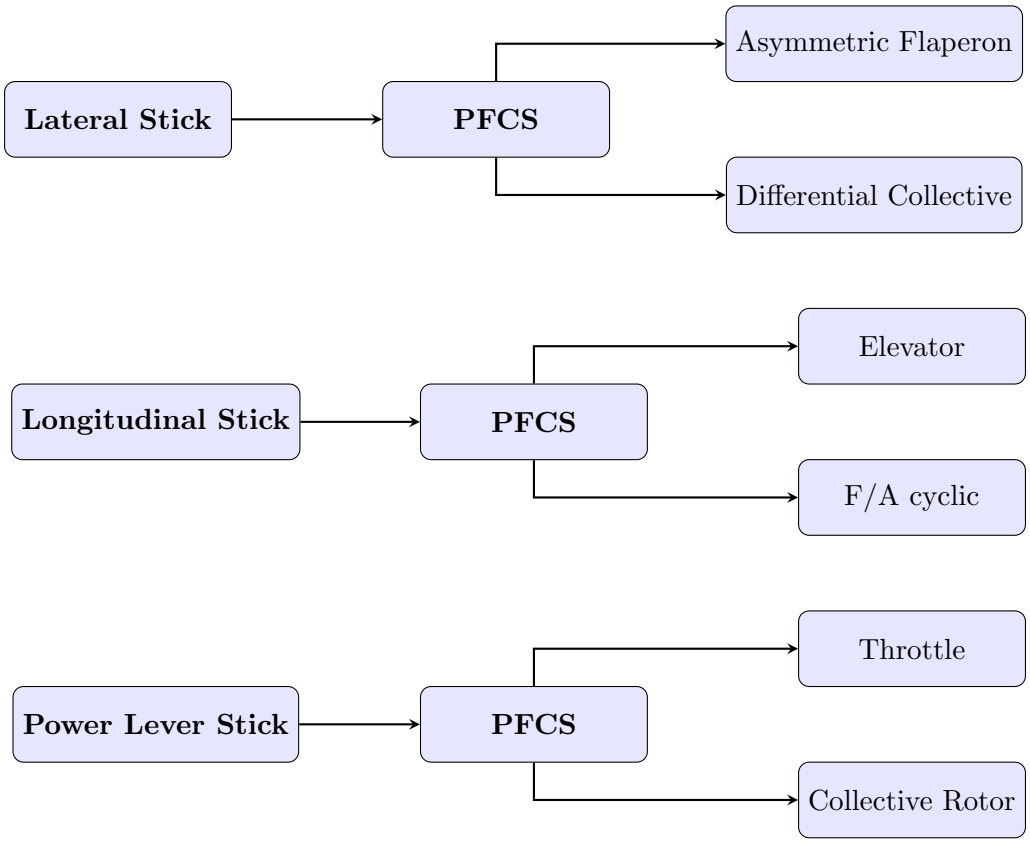

	min [in]	max [in]
Lateral stick	-4.80	4.80
Longitudinal stick	-4.80	4.80
Power Lever	0	10

Table A.1: Commands Travels Ref.[5]

Appendix B

MASST

B.1 MASST Graphic Interface

Figure B.1: MASST Graphic User Interface

B.2 XV-15 MASST Model

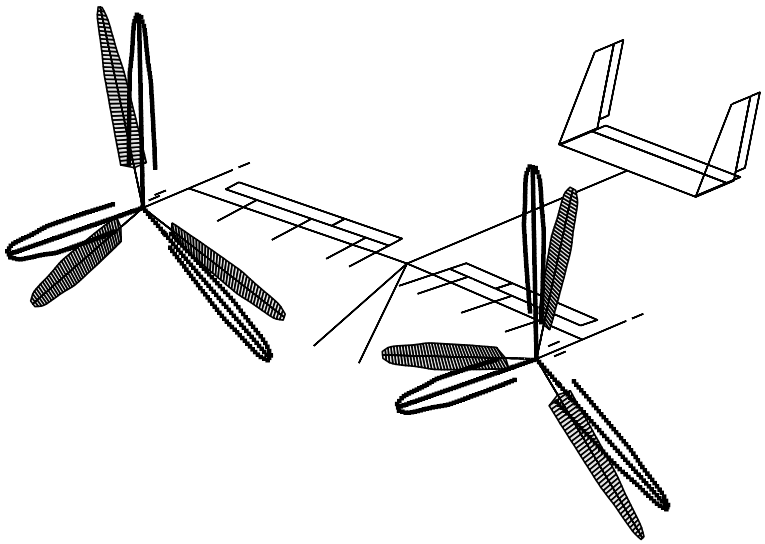

Figure B.2: APMODE, XV-15 MASST Model

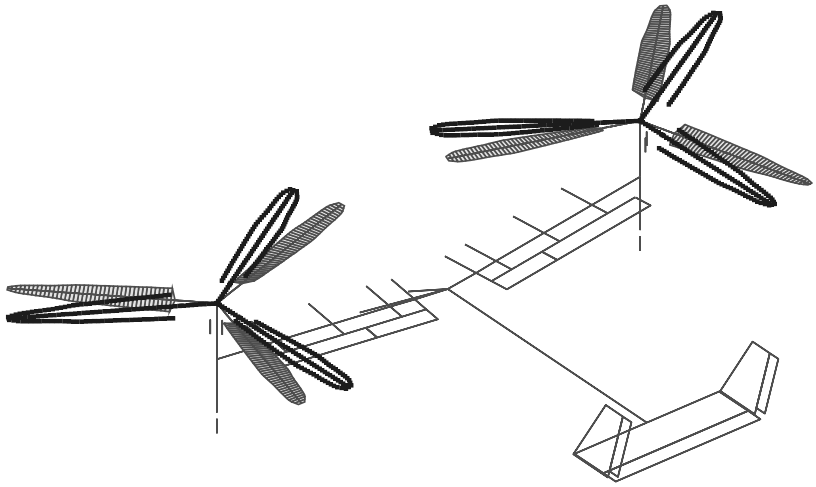

Figure B.3: HEMODE, XV-15 MASST Model

Appendix C

Airframe Substructuring Validation

clamped nacelle	f_1	f_2	f_3	f_4
NASTRAN [Hz]	3.1967	6.0941	6.1540	7.4984
MASST [Hz]	3.1971	6.0940	6.1539	7.4982
$err\%_{Hz}$	0.0125	0.0016	0.0016	0.0027
	f_5	f_6	f_7	f_8
NASTRAN [Hz]	8.4673	8.7503	–	–
MASST [Hz]	8.4648	8.7498	–	–
$err\%_{Hz}$	0.0295	0.0057	–	–

downstop-on	f_1	f_2	f_3	f_4
NASTRAN [Hz]	3.1930	6.0222	6.1019	7.3039
MASST [Hz]	3.1934	6.0221	6.1018	7.3037
$err\%_{Hz}$	0.0125	0.0017	0.0016	0.0027
	f_5	f_6	f_7	f_8
NASTRAN [Hz]	8.0501	8.5099	18.5371	18.8749
MASST [Hz]	8.0477	8.5093	18.5371	18.8748
$err\%_{Hz}$	0.0298	0.0071	0.0000	0.0005

downstop-off	f_1	f_2	f_3	f_4
NASTRAN [Hz]	3.1871	5.8551	5.9940	6.9863
MASST [Hz]	3.1875	5.8550	5.9939	6.9862
$err\%_{Hz}$	0.0126	0.0017	0.0017	0.0014
	f_5	f_6	f_7	f_8
NASTRAN [Hz]	7.5051	8.1705	12.2393	12.3696
MASST [Hz]	7.5030	8.1701	12.2389	12.3692
$err\%_{Hz}$	0.0280	0.0049	0.0033	0.0032

NAC=30°	f_1	f_2	f_3	f_4
NASTRAN [Hz]	3.1305	5.9362	6.1379	7.3938
MASST [Hz]	3.1219	5.9355	6.1679	7.3627
$err\%_{Hz}$	0.1886	0.1632	0.7993	0.4314
	f_5	f_6	f_7	f_8
NASTRAN [Hz]	7.5378	7.7042	11.6601	11.9065
MASST [Hz]	7.5860	7.6372	11.6942	11.7466
$err\%_{Hz}$	0.2537	1.9401	0.2925	1.3430

NAC=60°	f_1	f_2	f_3	f_4
NASTRAN [Hz]	3.0538	5.7262	6.0507	6.8592
MASST [Hz]	3.0339	5.6893	6.1415	6.9052
$err\%_{Hz}$	0.5735	0.7536	0.0978	0.2110
	f_5	f_6	f_7	f_8
NASTRAN [Hz]	7.2636	8.2201	10.6053	11.1806
MASST [Hz]	7.2058	8.1854	10.6121	10.7478
$err\%_{Hz}$	1.3296	2.2860	0.0641	3.8710

NAC=90°	f_1	f_2	f_3	f_4
NASTRAN [Hz]	3.0061	5.0603	5.3248	6.4488
MASST [Hz]	3.0061	5.0603	5.3230	6.4485
$err\%_{Hz}$	0.4372	0	0.2380	1.5932
	f_5	f_6	f_7	f_8
NASTRAN [Hz]	7.3111	8.6239	9.9558	10.0951
MASST [Hz]	7.3115	8.6238	9.9558	10.0949
$err\%_{Hz}$	0.0424	0.2637	0.0000	0.0020

Appendix D

NASTRAN Structural Airframe Results

D.1 XV-15 NASTRAN Bulk File

```
SOL 103
CEND
TITLE = XV 15 FEM model - wing modes
METHOD = 1
ECHO = NONE
SET 10 = 10
DISPLACEMENT(PUNCH) = 10
OLOAD = NONE
SPCFORCE = NONE
FORCE = NONE
STRESS = NONE
$-------------------------------------------------------------------------
BEGIN BULK
PARAM,GRDPNT,0 $ WEIGHT GENERATOR
EIGRL   1       2       9       6       0
$-------------------------------------------------------------------------
$ Nodes - [inches]
$ x : aligned with fuselage axis
$ y : aligned with wing axis

$ WING
GRID    1       0       288.68  193     6.74
GRID    2       0       294.178 144.75  5.05
```

```
GRID    3       0       299.675 96.5    3.37
GRID    4       0       305.173 48.25   1.684
GRID    16      0       307.921 28      0.977
GRID    5       0       310.67  0       0

GRID    17      0       307.921 -28     0.977
GRID    6       0       305.173 -48.25  1.684
GRID    7       0       299.675 -96.5   3.37
GRID    8       0       294.178 -144.75 5.05
GRID    9       0       288.68  -193    6.74

$ PROPROTOR point mass
GRID    10      0       241.38  193     6.74
GRID    11      0       241.38  -193    6.74

$ NACELLE  : from proprotor point mass 10/11 to points 12/13
GRID    12      0       333.29  193     6.74
GRID    13      0       333.29  -193    6.74

$ FUSELAGE
GRID    14      0       92.525  0       0
GRID    15      0       597.52  0       0

$------------------------------------------------------------------------
$ the structure is modelled using BAR elements --> CT,CG and EA coincide

$ WING
CBAR    12      12      1       2       0.      0.      1
$ wing - z -->out of plane ; y-->in plane
CBAR    23      12      2       3       0.      0.      1
CBAR    34      12      3       4       0.      0.      1
CBAR    416     12      4       16      0.      0.      1
CBAR    165     165     16      5       0.      0.      1
CBAR    517     165     5       17      0.      0.      1
CBAR    176     12      17      6       0.      0.      1
CBAR    67      12      6       7       0.      0.      1
CBAR    78      12      7       8       0.      0.      1
CBAR    89      12      8       9       0.      0.      1

$ PROPROTOR point mass + NACELLE
```

```
CBAR    110     100     1       10      0.      0.      1
                        0.      0.      -9      0.      0.      -9

CBAR    112     100     1       12      0.      0.      1
                        0.      0.      -9      0.      0.      -9

CBAR    911     100     9       11      0.      0.      1
                        0.      0.      -9      0.      0.      -9

CBAR    913     100     9       13      0.      0.      1
                        0.      0.      -9      0.      0.      -9

$ FUSOLAGE
CBAR    145     200     14      5       0.      0.      1
                        0.      0.      -43.2   0.      0.      -43.2
CBAR    515     200     5       15      0.      0.      1
                        0.      0.      -43.2   0.      0.      -11

$------------------------------------------------------------------------

$ CONCENTRATED ELEMENTS
$ there are two concentrated masses representing the proprotors and
$ a concentrated fuselage roll inertia

$proprotor
CONM2   10      10      0       1.44599
CONM2   11      11      0       1.44599

$roll inertia
CONM2   5       5       0
        5.79E+04

$------------------------------------------------------------------------
$ PBAR - bar properties

$ WING---------------------------------------------------------------------

$       ID      E(1)    G(1)    nu      rho
MAT1    1       1       1               0
```

```
$       ID      MAT1    A       I1      I2      J       NSM
PBAR    12      1       1.E+15  3.70E+9 1.12E+102.80E+9 0.0169
PBAR    165     1       1.E+15  3.70E+9 1E+15   1E+15   0.0169
$ torsion stiffness and chord bending increase near the fuselage



$ nacelle and fuselage are rigid beams
$ NACELLE-------------------------------------------------------------------
$       ID      E(1)    G(1)    nu      rho
MAT1    2       1       1               0

$       ID      MAT1    A       I1(EI1) I2(EI2) J(GJ)   NSM
PBAR    100     2       1.E+15  1.E+15  1.E+15  1.E+15  0.0446

$ FUSOLAGE------------------------------------------------------------------
$       ID      E(1)    G(1)    nu      rho
MAT1    3       1       1               0

$       ID      MAT1    A       I1(EI1) I2(EI2) J(GJ)   NSM
PBAR    200     3       1.E+15  1.E+15  1.E+15  1.E+15  0.0318

END DATA
```

D.2 XV-15 FE Stick Model Structural Properties

Component	Elements Type	N° Elements
Wing	Elastic Beam (BAR)	10
Left and Right Nacelles	Rigid Beam (RBE2)	4
Left and Right Rotor	Lumped Mass (CONM2)	2
Fuselage	Lumped Mass (CONM2)	1

Table D.1: XV-15 FE Components

Component	Length [in]	Weight [lb]
Wing	388.80	2.534
Left and Right Nacelle	92.40	3.166
Left and Right Rotor	0	1.118
Fuselage	0	6.182
Gross Weight : 13.000 lb		

Table D.2: XV-15 Weights

Inertia	I_{xx}[blob · in^2]	I_{yy}[blob · in^2]
CONM2	5.930E+4	2.100E+5
Inertia	I_{zz}[blob · in^2]	I_{xz}[blob · in^2]
CONM2	3.041E+5	0.147E+5

Table D.3: Concentrated Fuselage Properties

Stiffness	[lb·in^2]
Beam Bending	3.70E+09
Chord Bending	1.008E+10
Torsion	2.80E+09

Table D.4: XV-15 Wing Characteritics

D.3 XV-15 Mode Shapes Visualisation

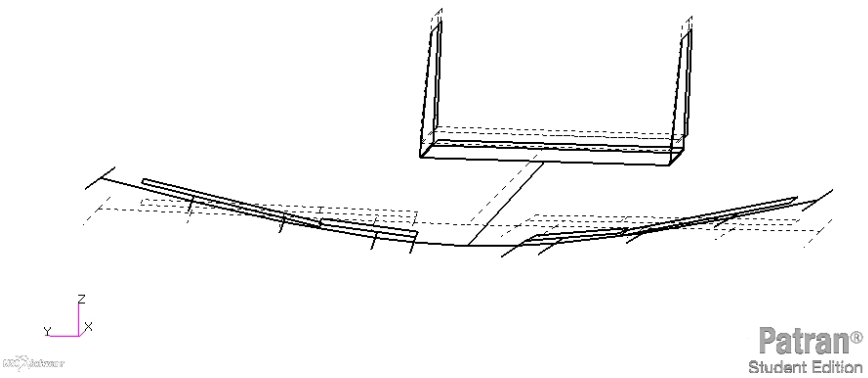

Figure D.1: SWB, symmetric wing bending

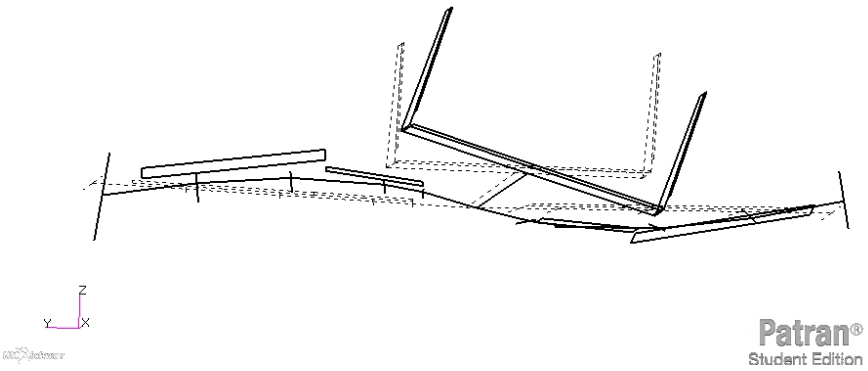

Figure D.2: AWB, asymmetric wing bending

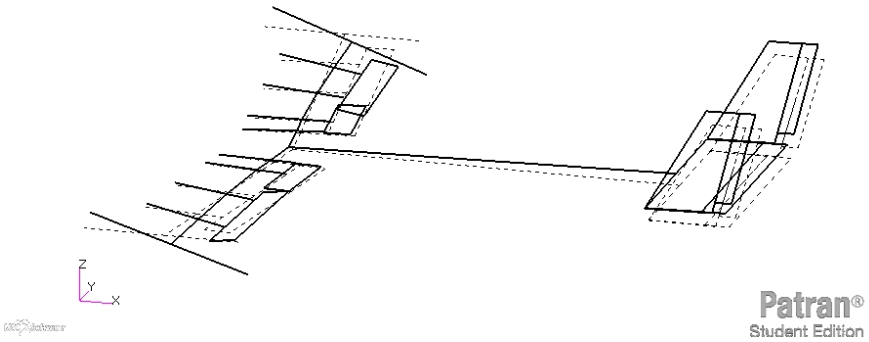

Figure D.3: SWT, symmetric wing torsion

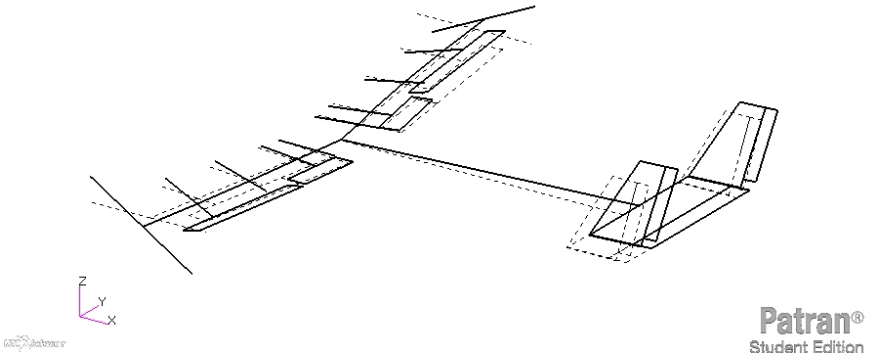

Figure D.4: AWT, asymmetric wing torsion

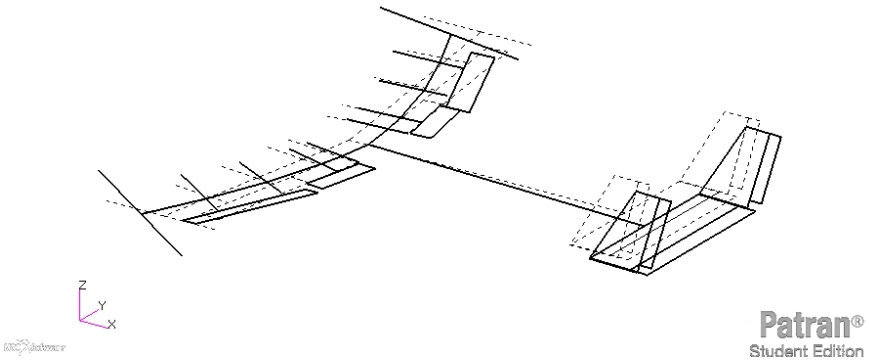

Figure D.5: SWC, symmetric wing chord

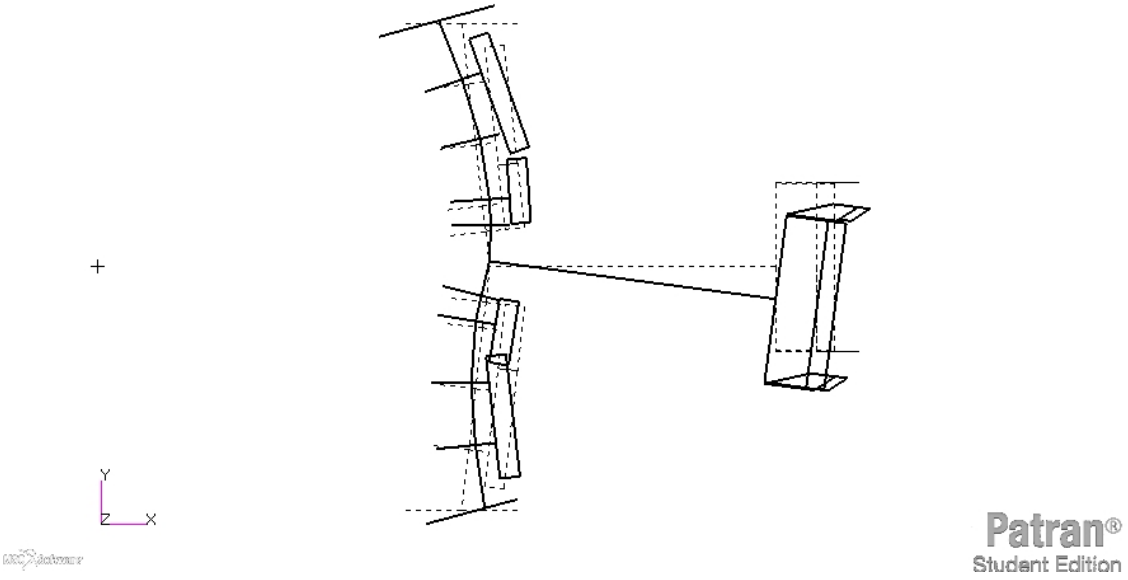

Figure D.6: AWC, asymmetric wing chord

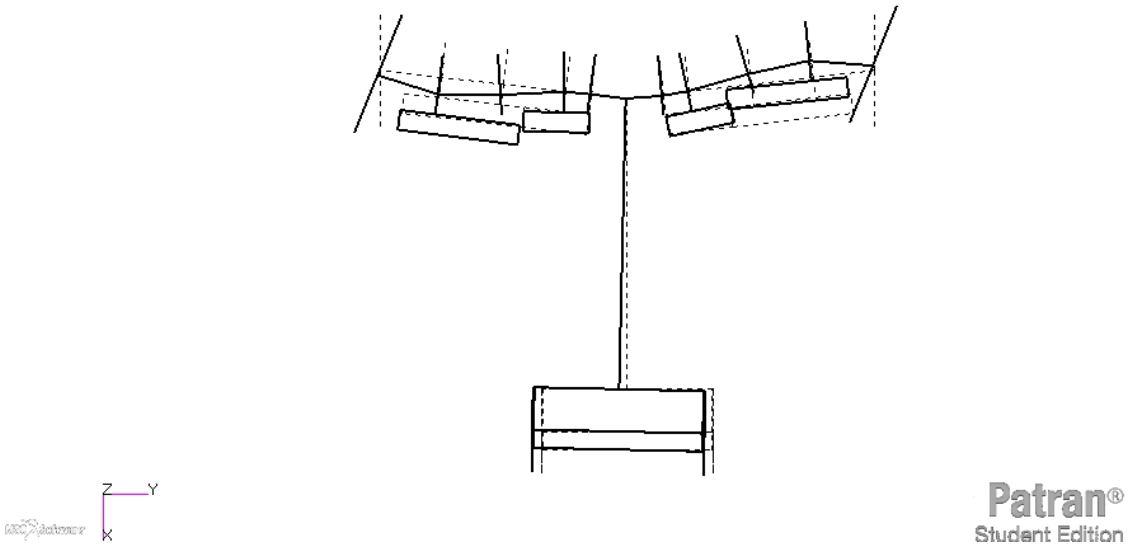

Figure D.7: SPY, symmetric pylon yaw

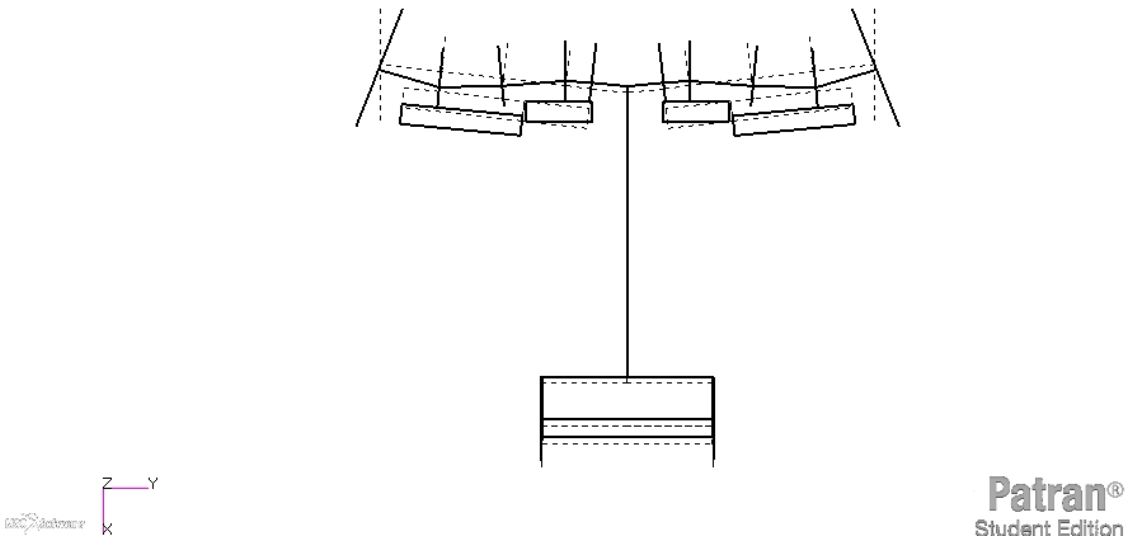

Figure D.8: APY, asymmetric pylon yaw

Appendix E

Lateral PAO Appendix

E.1 AWC Mode Shape Visualisation

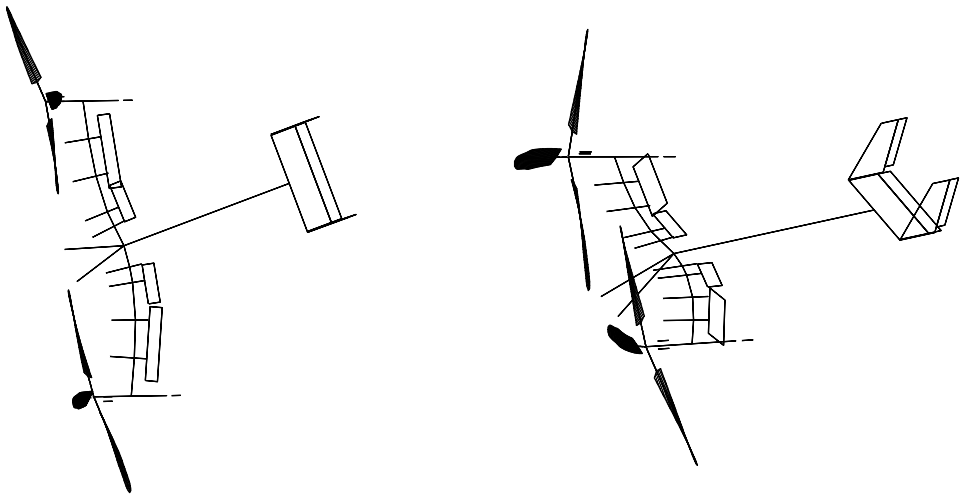

(a) AWC mode shape top view

(b) AWC mode shape lateral view

Figure E.1: Pilot-in-the-loop AWC mode shape

E.2 High Gain Pilot

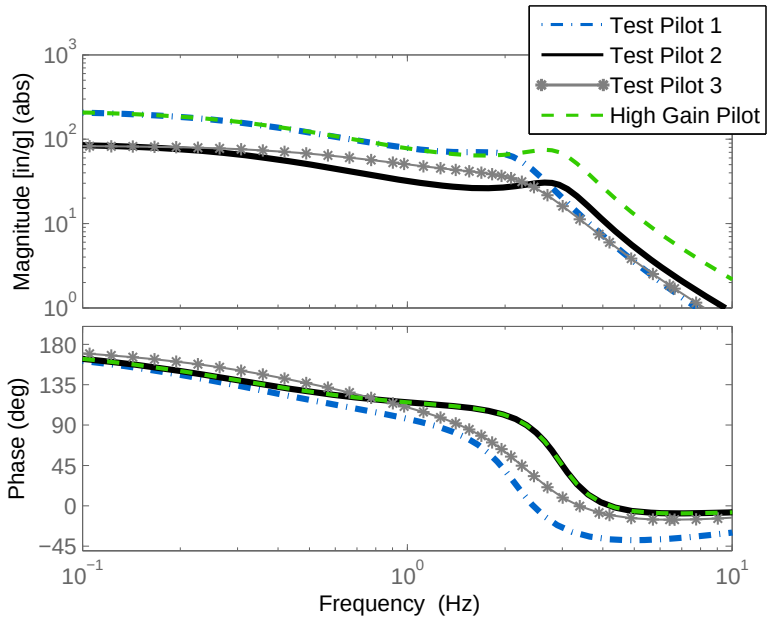

Figure E.2: High Gain Pilot

	units	Pilot 1	Pilot 2	Pilot 3	High Gain Pilot
μ	%/g	216.26	88.67	83.88	216.26
T_z	sec	0.02	0.05	0.03	0.05
T_p	sec	0.51	0.49	0.26	0.49
ξ	%	26.87	23.11	39.66	23.11
ω_n	rad/s	13.59	18.53	14.81	18.53

Table E.1: Pilot/Lateral stick dynamic properties

E.3 Modifications of Tail Geometry

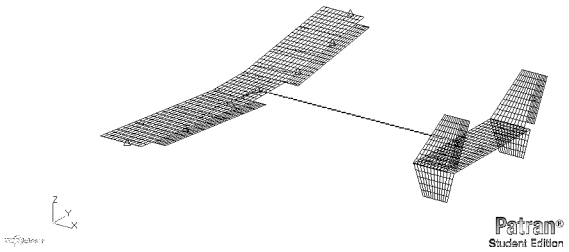

Figure E.3: Nominal Tail Geometry

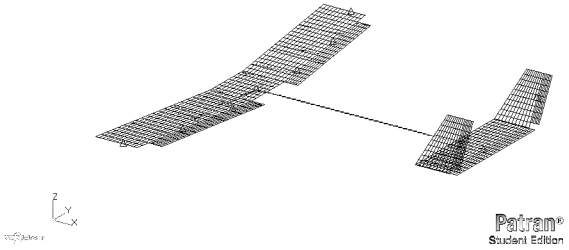

Figure E.4: Tail Geometry Case 1

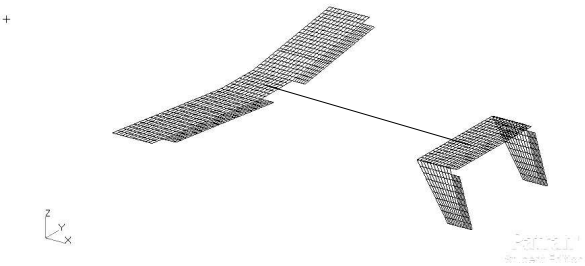

Figure E.5: Tail Geometry Case 2

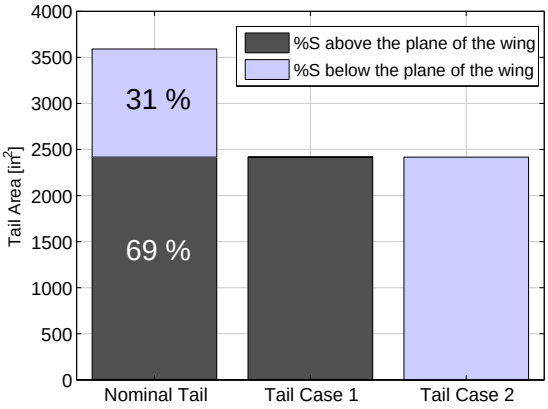

Figure E.6: Tail Designs

Case n°	S [in^2]
nominal	3.5910E+03
case 1	2.4173E+03
case 2	2.4173E+03

Table E.2: Tail Surfaces

E.3.1 Results Tail Case 1

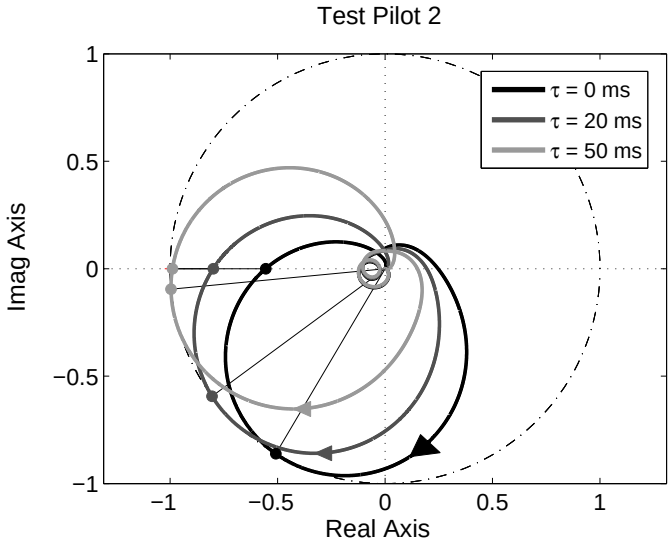

Figure E.7: LTF Nyquist diagram, Tail Case 1, Time Delay, Test Pilot 2

τ [ms]	$\mathbf{G_m}$[dB]	f($\mathbf{G_m}$)[Hz]
0	5.1128	3.317
20	1.96	3.28
50	0.0977	3.25
τ [ms]	$\mathbf{P_m}$[dB]	f($\mathbf{P_m}$)[Hz]
0	59.5	3.25
20	36.4	3.24
50	5.47	3.24

Table E.3: Stability Margins - Tail Geometrical Modification

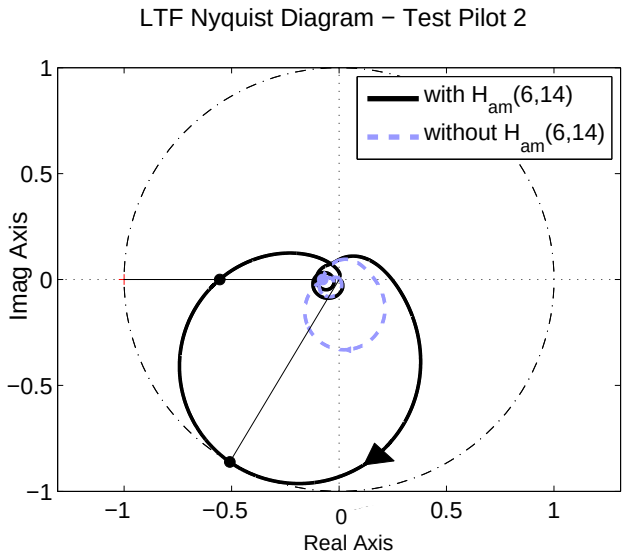

Figure E.8: LTF Nyquist Diagram with/out Generalised Aerodynamic Force on the yaw mode due to asymmetric deflection of the flaperons. Tail case 1, $\tau = 0$, Test Pilot 2

YFC	$\mathbf{G_m}$[dB]	f($\mathbf{G_m}$)[Hz]
yes	5.1128	3.317
no	23.4	3.39
	$\mathbf{P_m}$[dB]	f($\mathbf{P_m}$)[Hz]
yes	59.4719	3.2500
no	–	–

Table E.4: Stability Margins - Tail Geometrical Modification